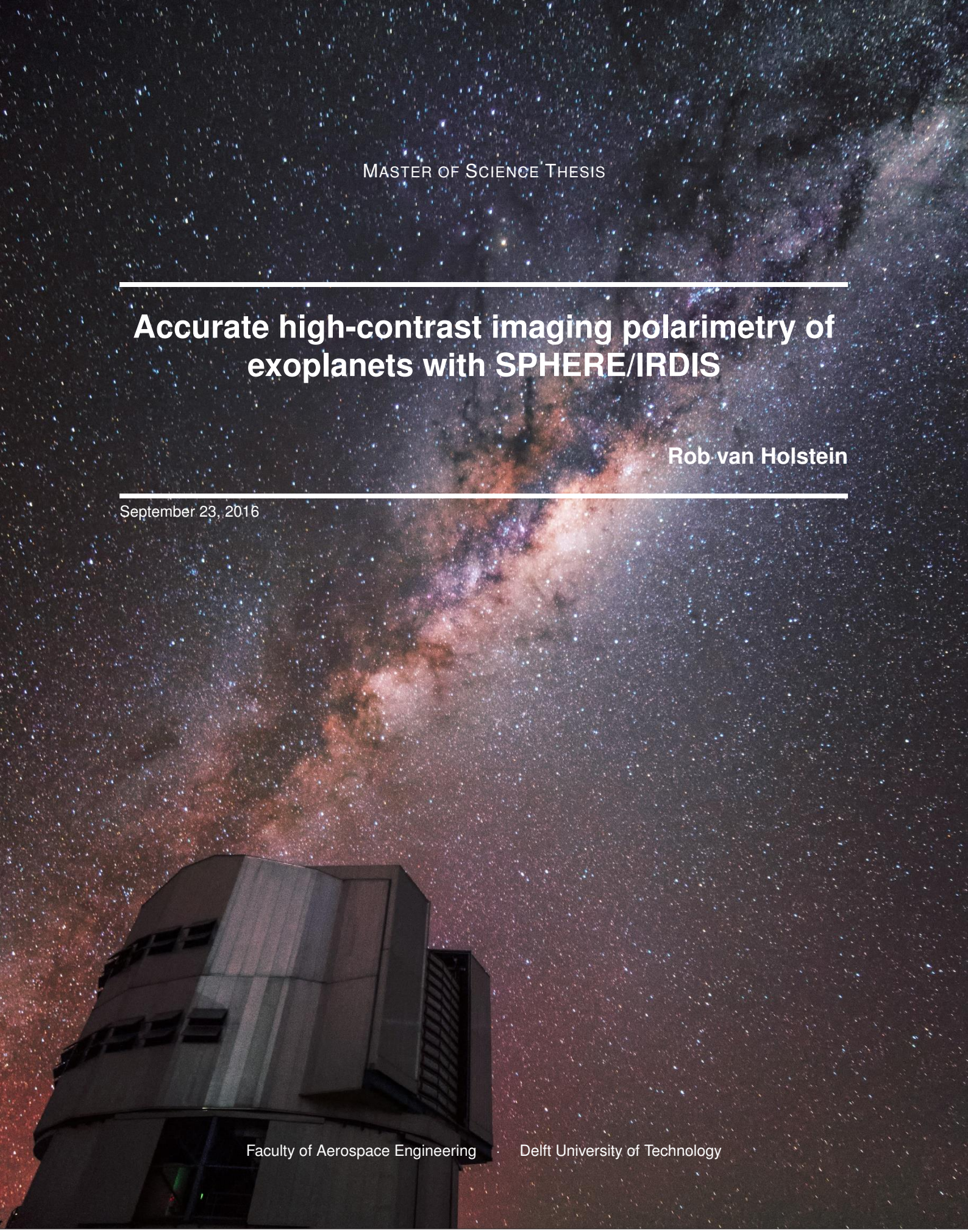

MASTER OF SCIENCE THESIS

Accurate high-contrast imaging polarimetry of exoplanets with SPHERE/IRDIS

Rob van Holstein

September 23, 2016

Faculty of Aerospace Engineering · Delft University of Technology

TU Delft Delft University of Technology

Challenge the future

Accurate high-contrast imaging polarimetry of exoplanets with SPHERE/IRDIS

MASTER OF SCIENCE THESIS

For obtaining the degree of Master of Science in Aerospace Engineering
at Delft University of Technology

Rob van Holstein

September 23, 2016

Faculty of Aerospace Engineering · Delft University of Technology

vanholstein@strw.leidenuniv.nl
robvanholstein@gmail.com

Cover photo: ”Surrounded by a sparkling sea of stars, the Milky Way extends over ESO’s Very Large Telescope facility” by J. Busqué / ESO

DELFT UNIVERSITY OF TECHNOLOGY
DEPARTMENT OF
ASTRODYNAMICS AND SPACE MISSIONS

The undersigned hereby certify that they have read and recommend to the Faculty of Aerospace Engineering for acceptance a thesis entitled **"Accurate high-contrast imaging polarimetry of exoplanets with SPHERE/IRDIS"** by **Rob van Holstein** in partial fulfillment of the requirements for the degree of **Master of Science**.

Dated: September 23, 2016

Head of department:

prof.dr. L.L.A. Vermeersen

Supervisor:

dr. D.M. Stam

Supervisor:

dr.ir. F. Snik

Supervisor:

J. de Boer MSc

Reader:

prof.dr. B.R. Brandl

Reader:

ir. K.J. Cowan

Preface and acknowledgments

So here it is, my final master's thesis. I am nearing the end of my seven years of studies at TU Delft, of which the past two years I worked on the polarimetric mode of SPHERE/IRDIS. During that time I have learned a great deal about polarimetry, instrumentation, astronomy, and myself, and I met a lot of great people. To me, the highlights of the past two years were the internship at ESO in Chile and the observation proposal getting accepted. Although this thesis means the end of my studies, I am really just getting started: the day after my graduation I will start a PhD on high-contrast imaging polarimetry at the Leiden Observatory and in two week I will fly to Chile together with Frans Snik to attempt to — for the first time — measure exoplanetary polarization signals through direct imaging.

It's funny to think about how I ended up where I am now. During my master's, I was thinking of pursuing a career in scientific spaceflight. My attempt to obtain an internship position at JPL failed. Soon after, I entered Daphne Stam's office and asked if she knew any internship opportunities abroad. 'I can easily get you a position at DLR in Germany', she suggested. 'That's just like the Netherlands, they only speak a different language', I responded. 'Well, in two days I have a meeting at the Leiden Observatory and there will be people from ESO Santiago. I will see what I can do'. And so it came to pass. What started as an exciting internship project, quickly turned into a passion for polarimetry. It is probably the very timing of entering Daphne's office that has shaped the rest of my career.

I would like to express my gratitude to Daphne Stam for her supervision in the past two years and the valuable feedback she provided on my work. I am also very thankful to Jos de Boer, for his supervision, for teaching me about polarimetry and for helping me out whenever necessary. I really enjoyed working with Jos, and I hope we will continue doing that in the years to come. I would like to thank Frans Snik for his supervision, feedback and the enumerable number of great ideas he comes up with. Special thanks goes to Julien Girard, who went to great lengths to obtain the data I needed, exactly how I needed it. Without his efforts, I could never have achieved the results I can now present in this thesis. Finally, I would like to thank my parents, who supported me and provided me an excellent environment to develop myself.

I am very much looking forward to my PhD and the rest of my career. With a little luck I could have a flying start: fingers crossed for clear skies and actual polarized planets!

Honselersdijk
September 23, 2016

Rob van Holstein

Summary

The search for and characterization of exoplanets and other sub-stellar companions are hot topics in contemporary astronomy. Currently, the characterization of the atmospheres of exoplanets through direct imaging leverages on the analysis of only the intensity of their light as a function of wavelength and time. Additional information on the composition and structure of planetary atmospheres — that cannot be obtained with spectroscopy — can be deduced with polarimetry, i.e. measuring the direction of oscillation of the electric fields of light.

Not only the starlight that an exoplanet reflects is expected to be polarized, but also the thermal emission of a planet, as this radiation from inside the atmosphere will be scattered by cloud and haze particles on its way up. Indeed, the polarized thermal radiation of several field brown dwarfs has already been measured and is attributed to the scattering of the radiation by patchy clouds in their atmospheres. The degree of linear polarization of hot exoplanets at near-infrared wavelengths is expected to generally be larger than 0.1% and could be up to several percent in some cases. Measurements of the polarized thermal emission of exoplanets can provide information on the presence and patchiness of atmospheric clouds and hazes, the cloud top pressure, spatial structure such as rotational flattening and cloud bands, the atmospheric rotation rate, and the surface gravity and mass of the companion. By determining the angle of linear polarization, the planet's projected spin axis could be constrained.

The recently commissioned VLT instrument SPHERE is a high spatial resolution, high-contrast, direct imaging instrument that is specifically designed to detect and characterize giant exoplanets orbiting nearby stars. SPHERE's near-infrared instrument arm IRDIS has a dual-beam polarimetric mode that is primarily used for high-contrast imaging of circumstellar disks, as it is expected to be too insensitive to directly measure the polarized thermal emission of exoplanets. However, IRDIS has already detected exoplanets with huge signal-to-noise ratio using angular differential imaging (ADI) of thermal fluxes. The aim of this thesis is therefore to investigate the feasibility of combining ADI and accurately calibrated polarimetry with SPHERE/IRDIS to for the first time detect and possibly characterize exoplanetary atmospheres through direct imaging polarimetry at near-infrared wavelengths.

To assess whether IRDIS can detect the expected polarization signal of exoplanets, and using HR 8799's planetary system as a study case, IRDIS' polarimetric sensitivity is estimated by extrapolating the results from VLT/NaCo observations to IRDIS, and by simulating single-beam polarimetric measurements with real IRDIS data. Based on these estimates, SPHERE/IRDIS is expected to reach sub-percent polarimetric sensitivity when combining extreme adaptive optics, coronagraphy, ADI with advanced data reduction techniques and dual-beam polarimetry.

A model describing the modification of the polarization signal induced by the telescope and instrument is established and validated with available internal calibration measurements and observations of a standard star. It appears that for some filters and particular combinations of the parallactic and altitude angle, only a very small part ($\sim$ 10%) of the incident linearly polarized signal is actually measured by the instrument. This loss of signal is accompanied by large offsets in the angle of linear polarization. It is also found that the instrumental polarization of the telescope and SPHERE's first mirror varies with telescope altitude angle and can reach values of a few percent.

To limit the instrumental polarization and the loss of signal, an observation strategy is presented for IRDIS' polarimetric mode. In addition, a data reduction method is developed that uses the instrument model to derive an exoplanet's true degree and angle of linear polarization from the measured polarization signal. It is estimated that, after correcting for the modification of the polarization signal induced by the complete optical system, a polarimetric accuracy of $\leq$ 0.1% is reached.

Given that an exoplanet will generally be between a few tenths of a percent and a percent polarized, it is concluded that, if SPHERE/IRDIS can indeed attain the predicted sub-percent polarimetric sensitivity when combining angular differential imaging and polarimetry, exoplanetary atmospheres can be characterized for the first time through direct imaging polarimetry.

Table of Contents

1 Introduction

The search for and characterization of exoplanets and other sub-stellar companions are hot topics in contemporary astronomy. Currently, the characterization of the atmospheres of exoplanets through direct imaging leverages on the analysis of only the intensity of their light as a function of wavelength and time. However, additional information on the composition and structure of exoplanetary atmospheres could be deduced with polarimetry. In this master thesis, we investigate the feasibility of combining angular differential imaging and accurately calibrated polarimetry with the recently commissioned VLT instrument SPHERE/IRDIS to for the first time characterize exoplanetary atmospheres through direct imaging polarimetry at near-infrared wavelengths.

1.1 Characterizing exoplanets through direct imaging

Almost none of the approximately 3500 exoplanets currently detected and confirmed (The Extrasolar Planets Encyclopaedia, 2016) have been detected directly, but their presence has been derived from the effect the planet has on its parent star. Particularly successful detection techniques are the transit photometry and radial-velocity methods. Since these two methods are biased towards large planets in edge-on orbits close to their star (Pater & Lissauer, 2010), not many small, Earth-sized planets in the star's habitable zone or planets in wide orbits have been found. In addition, only basic planetary parameters can be derived with these indirect methods, such as the planetary radius, the orbital period, a lower limit on the planetary mass and, through transit spectroscopy, information on the composition and temperature of the upper atmosphere (Pater & Lissauer, 2010).

The next step in exoplanet research is characterization, i.e. the determination of physical properties of the atmosphere and/or surface of an exoplanet, such as the composition, sizes and spatial distributions of cloud particles. A promising way to do this is by capturing these planets on an image directly. For this direct imaging, the planet needs to be spatially resolved from the star (a planet itself will be spatially unresolved, i.e. it will be visible as a point source on the image). This is very challenging however, because the contrast between a star and an orbiting planet is huge (several orders of magnitude) and, unless the planet is at a large angular separation from the star, the point spread function (PSF) of the much brighter star washes out that of the planet. Indeed, the best candidates for direct imaging are self-luminous sub-stellar companions, such as young massive exoplanets or brown dwarfs, in wide orbits that emit most of their (thermal) radiation at near-infrared wavelengths.

The first directly imaged exoplanet was a young, very massive and hot planet orbiting very far ($\sim$ 55 AU) from a brown dwarf relatively close ($\sim$ 70 pc) to Earth (Chauvin et al., 2005). This detection was possible because of the exceptionally low contrast between the thermal emission of the planet and that of the star. To detect fainter and/or closer-in planets, observations with ground-based telescopes can be performed in the so-called pupil-tracking mode, in which the field of view rotates with respect to the detector while the optics of the instrument and telescope remain fixed with respect to the detector (Marois et al., 2006). Pupil-tracking allows for effective subtraction of the stellar PSF from the image with angular differential imaging (ADI), thereby attaining a high contrast. ADI has already been successfully employed on various telescopes and instruments. Notable successes include the recent discovery of a young, massive planet in a triple-star

system (Wagner et al., 2016), and the detection of a young gas giant estimated to have twice the mass of Jupiter around the star Eridani b (Macintosh et al., 2015), making it the smallest directly imaged exoplanet to date.

Direct imaging (using ADI) enables the characterization of the atmospheres of self-luminous, hot, massive planets with photometry and spectroscopy. With these methods, the planets' luminosity and atmospheric composition, structure and temperature can be constrained (e.g. Lafrenière et al., 2008; Ingraham et al., 2014; Chilcote et al., 2015; Macintosh et al., 2015; Zurlo et al., 2016). Perhaps the best studied directly imaged exoplanets are the four young giant planets orbiting the star HR 8799 (Marois et al., 2008; Marois, Zuckerman, et al., 2010). Recent spectral measurements of (some of) these planets have revealed the presence of gases such as CO, CH_4 and H_2O (Konopacky et al., 2013) and sub-micron dust particles (Bonnefoy et al., 2016) in their atmospheres. Temporal variations in near-infrared gaseous absorption features, such as those of CH_4, strongly suggest the presence of patchy clouds (Oppenheimer et al., 2013).

1.2 Characterizing exoplanets through polarimetry

Additional information on the composition and structure of planetary atmospheres — that cannot be obtained with spectroscopy — can be deduced with polarimetry, i.e. measuring the direction of oscillation of the electric fields of light. Not only the starlight that an exoplanet reflects is expected to be polarized (Seager et al., 2000; Stam et al., 2004), but also the thermal emission of a planet (or brown dwarf), as this radiation from inside the atmosphere will be scattered by cloud and haze particles on its way up (Sengupta & Marley, 2010; de Kok et al., 2011). However, the net thermal polarization signal of a spherically symmetric exoplanet is zero, since the planet's (2D-projected) disk is spatially unresolved when observing the planet and the polarization signals emanating from different parts of the disk cancel each other (de Kok et al., 2011). Therefore, for a net polarization signal to arise in the thermally emitted radiation, the companion's disk must feature asymmetries such as equatorial flattening due to rapid rotation, patchy clouds or spots in the atmosphere (de Kok et al., 2011), or obscuring moons (Sengupta & Marley, 2016). The degree of linear polarization of hot exoplanets at near-infrared wavelengths is expected to generally be larger than 0.1% and could be up to several percent in some cases (de Kok et al., 2011).

Measurements of the polarized thermal emission of exoplanets could provide information on the presence and patchiness of atmospheric clouds and hazes, the cloud top pressure, spatial structure such as rotational flattening and cloud bands, and the surface gravity and mass of the companion (de Kok et al., 2011; Marley & Sengupta, 2011). By determining the angle of linear polarization, the planet's projected spin axis could be constrained (de Kok et al., 2011). If the polarization signal is periodic, it could indicate the presence of persistent storms, such as Jupiter's Great Red Spot, and reveal atmospheric rotation rates. Finally, combining polarimetric measurements with flux measurements could reveal atmospheric particle properties, such as albedo and size. The information on the atmospheric composition and structure revealed through polarimetry is important, as it will significantly increase the accuracy of fitting atmospheric models based on known spectra of field brown dwarfs and sub-stellar companions to spectroscopic exoplanet observations, which currently results in errors of at least 10% (Ingraham et al., 2014; Chilcote et al., 2015; Bonnefoy et al., 2016).

Near-infrared polarimetry has already been successfully performed for dozens of field brown dwarfs, yielding degrees of linear polarization between 0.1 to 2.5% in the I-band (Sengupta & Marley, 2010) and up to 0.8% in the Z- and J-bands (Miles-Páez et al., 2013). For these field dwarfs, the polarization likely arises from patchy clouds. The polarization signals of exoplanets are expected to be stronger, because exoplanets have a lower surface gravity, hence a stronger flattening for a given rotation rate, and a lower effective atmospheric temperature can yield stronger polarization signals for a given temperature gradient (de Kok et al., 2011). However, the first direct measurement of exoplanetary polarization signals has yet to be performed.

1.3 Combining ADI and polarimetry with SPHERE/IRDIS

The recently commissioned instrument SPHERE (Spectro-Polarimetric High-contrast Exoplanet REsearch) is specifically designed to directly image exoplanets (Beuzit et al., 2008) and is installed at Unit Telescope 3 (UT3) of the Very Large Telescope (VLT) operated by the European Southern Observatory (ESO). SPHERE is a high spatial resolution, high-contrast, direct imaging instrument operating in the visible and near-infrared

that combines extreme adaptive optics, stellar coronagraphs and three differential imagers for direct imaging and characterization of giant exoplanets orbiting nearby stars. Two of these imagers are the visible imaging polarimeter ZIMPOL (Zurich IMaging POLarimeter) (Thalmann et al., 2008) and the near-infrared spectrograph IFS (Integral Field Spectrograph) (Claudi et al., 2008).

SPHERE also comprises the near-infrared dual-band imager IRDIS (InfraRed Dual-band Imager and Spectrograph) (Dohlen et al., 2008). SPHERE/IRDIS is designed to detect the (unpolarized) near-infrared thermal emission of young, massive exoplanets with contrast ratios of planet to star of 10^{-4} to 10^{-6} using spectral differential imaging (SDI), in which spectral features are observed that are expected in the spectra of exoplanets, but not in those of the parent stars (Schmid et al., 2012). In addition, SPHERE/IRDIS can observe in pupil-tracking mode, allowing for angular differential imaging (ADI) to be performed. Recently, spectral measurements of the four known planets around HR 8799 have been performed with IRDIS using ADI (Zurlo et al., 2016).

IRDIS also has a dual-beam polarimetric mode that is primarily used for high-contrast imaging of circumstellar disks using polarimetric differential imaging (PDI) (Langlois et al., 2014). In this mode, two images in orthogonal polarization directions are taken, and then subtracted. Since light scattered by a circumstellar disk is polarized and direct starlight is not (Kemp et al., 1987), subtracting the two images yields an image in which the starlight is suppressed, enhancing the contrast up to three to five orders of magnitude (Keller et al., 2010). Unfortunately, IRDIS' polarimetric mode is expected to be too insensitive to directly measure the polarized thermal emission of exoplanets.

However, as IRDIS has already detected exoplanets with huge signal-to-noise ratio (*SNR*) using ADI alone ($SNR > 200$ for some planets of HR 8799; Zurlo et al., 2016), combining ADI with dual-beam polarimetry (de Juan Ovelar et al., submitted) could enable the first ever direct detection of exoplanetary polarization signals. This combination of ADI and polarimetry is the basic polarimetric mode of the Gemini Planet Imager (Perrin et al., 2015) and is also offered by SPHERE/ZIMPOL (Thalmann et al., 2008). However, since ZIMPOL observes at visible wavelengths, it cannot detect the polarized thermal emission of exoplanets. Measurements of the thermal polarization signals of the planets of HR 8799 have already been attempted with VLT/NaCo using ADI combined with polarimetry, but the attained contrast appeared to be insufficient for a detection (de Juan Ovelar et al., submitted). Since SPHERE's adaptive optics system is more advanced than NaCo's, the logical step is to try to measure these thermal exoplanetary polarization signals with IRDIS.

1.4 Main objective and methods

The main objective of this master thesis is *to investigate the feasibility of combining angular differential imaging and accurately calibrated polarimetry with SPHERE/IRDIS to for the first time detect and possibly characterize exoplanetary atmospheres through direct imaging polarimetry at near-infrared wavelengths*.

To this end, IRDIS' *polarimetric sensitivity*, i.e. the noise level in the degree of linear polarization, will be estimated to assess whether IRDIS can detect the expected polarization signal of exoplanets. To acquire a first estimate of the polarimetric sensitivity of IRDIS, and using HR 8799's planetary system as a study case, the null results from the NaCo observations (de Juan Ovelar et al., submitted) will be extrapolated to IRDIS by scaling the attained polarimetric sensitivities with the intensity SNR's. An independent estimate of the sensitivity will be obtained by simulating single-beam polarimetric measurements with (non-polarimetric) IRDIS dual-band data of HR 8799 taken with the K2 filter (Zurlo et al., 2016).

To derive the exoplanet's true degree and angle of linear polarization from the measured polarization signal, a model describing the *polarimetric response* of the complete optical system, i.e. the modification of the polarization signal induced by the telescope and instrument, will be established and validated with available internal calibration measurements and observations of a standard star. The model will then be used to accurately determine the linearly polarized intensity and angle of linear polarization over the circumstellar disk of TW Hya to exemplify the correction of the optical system's polarimetric response. Finally, the *polarimetric accuracy* of the measurements, i.e. the uncertainty in the measured polarization signal, will be established. Because the degree of linear polarization of exoplanets at near-infrared wavelengths will generally only be between a few tenths of a percent and a percent, the aim is to achieve both a polarimetric sensitivity and a total absolute polarimetric accuracy (after correcting for the polarimetric response of the complete optical system) of $\sim 0.1\%$[1]. To attain a total absolute polarimetric accuracy of $\sim 0.1\%$, an ab-

[1] To constrain the projected spin axis of an exoplanet, the angle of linear polarization needs to be measured with an accuracy

solute polarimetric accuracy, i.e. the uncertainty in the instrumental polarization, of $< 0.1\%$ and a relative polarimetric accuracy, i.e. the accuracy that scales with the input polarization signal, of $\sim 1\%$ is aimed for.

Based on the thesis work, an application for observing time was submitted to ESO that proposes to measure the degree and angle of linear polarization of HR 8799's planets with SPHERE/IRDIS (see Appendix A). The proposed observations have been accepted and will take place in October 2016. If successful, it will be the first time exoplanetary atmospheres are characterized through direct imaging polarimetry.

1.5 Contents and structure

In Chapter 2 of this thesis, the mathematical description of the polarization of light will be presented. In the same Chapter, the optical path and relevant components of the Unit Telescope and SPHERE/IRDIS as well as the measurement technique used for polarimetry will be described. In Chapter 3, the working principle of the combination of ADI and polarimetry will be outlined and the polarimetric sensitivity of IRDIS will be estimated. After that, the polarimetric response model, and its validation and accuracy for the optical path in the instrument will be discussed in Chapter 4. Next, Chapter 5 will cover the validation and model accuracy for the remaining part of the optical path, i.e. the telescope and the first mirror of the SPHERE. Chapter 6 will then discuss the polarimetric response of the complete optical system during science observations, correct observations of TW Hya's disk for the polarimetric response of the system, and provide an estimate of the polarimetric accuracy of the complete optical system. Finally, conclusions and recommendations will be presented in Chapter 7.

of a few degrees. However, the accuracy of measuring the angle of linear polarization is not covered in this thesis.

2 Measuring polarization with SPHERE/IRDIS

The recently commissioned instrument SPHERE, installed at Unit Telescope 3 (UT3) of the Very Large Telescope (VLT), combines extreme adaptive optics, stellar coronagraphs and three differential imagers for direct imaging and characterization of giant exoplanets orbiting nearby stars. IRDIS is one of these imagers and has a dual-beam polarimetric mode that is primarily used for high-contrast imaging of circumstellar disks at near-infrared wavelengths using polarimetric differential imaging (PDI). In Section 2.1 of this Chapter, the mathematical description of the polarization of light will be presented. Subsequently, the optical path and relevant components of the Unit Telescope (UT) and SPHERE/IRDIS as well as the measurement technique for polarimetry will be discussed in Section 2.2.

2.1 Describing polarization of light

Electromagnetic radiation such as light can be described as a transverse wave of vibrating electric and magnetic fields perpendicular to each other that propagates at the speed of light. When the oscillations of the electric and magnetic fields have a preferential direction in space, light is said to be polarized (Tinbergen, 2005). To describe polarization, only the electric field vector is considered. Light is fully linearly polarized if the electric field oscillates in a single direction, and fully circularly polarized if the tip of the electric field vector traces out a circle at the frequency of oscillation. Circularly polarized light can be seen as a combination of two perpendicular linearly polarized waves with electrical field vibrations of equal amplitude that have a $\pm 90^\circ$ phase difference. The sense of rotation depends on the sign of the phase difference.

The most general form of polarization is elliptical polarization, when the tip of the electric field vector traces out an ellipse at the frequency of oscillation (Tinbergen, 2005). Elliptically polarized light can be seen as a combination of two perpendicular linearly polarized waves with electrical field vibrations of unequal amplitude that have a $\pm 90^\circ$ phase difference. Linear and circular polarization are special forms of the more general elliptical polarization. When light is unpolarized, the tip of the electric field vector moves in a complete random pattern. Partially polarized light is a combination of an unpolarized and a fully polarized component. For an in-depth treatment of the nature of polarization, see Tinbergen (2005).

The total intensity and polarization state of light can be described by a Stokes vector $\boldsymbol{S}$ (Tinbergen, 2005):

$$\boldsymbol{S} = \begin{bmatrix} I \\ Q \\ U \\ V \end{bmatrix} \tag{2.1}$$

with I the total intensity (or flux), Q and U the linearly polarized intensities and V the circularly polarized intensity. Stokes vectors can be added, which represents incoherent (i.e. there is no constant phase difference between the components being added) superposition of beams. The so-called Stokes parameters I, Q, U and V are usually expressed in units of $\mathrm{W\,m^{-2}}$. Stokes vectors can be added, which represents incoherent (i.e. there is no constant phase difference between the components being added) superposition

of beams.

The Stokes parameters are defined with respect to a reference frame with positive and negative Stokes Q corresponding to vertical and horizontal linear polarization, respectively (Snik et al., in preparation) (see Figure 2.1). When looking along the beam of light, positive Stokes U is the intensity of linearly polarized light oriented 45° clockwise from positive Stokes Q. Finally, positive Stokes V is defined as circularly polarized light with counterclockwise rotation when looking along the beam of light. In the celestial reference frame, positive Stokes Q is aligned with the local meridian, and in the instrument's reference frame, positive Stokes Q corresponds to vertical, i.e. perpendicular to the Nasmyth platform that SPHERE is installed on.

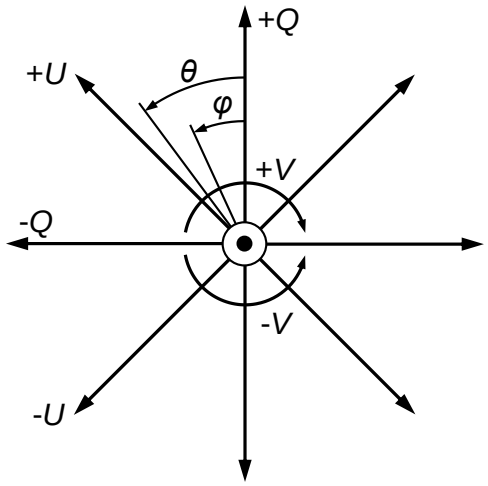

Figure 2.1: Reference frame for the definition of the Stokes parameters with positive and negative Stokes Q defining the vertical ($+Q$) and horizontal ($-Q$) axes, respectively. The propagation direction of the light beam is out of the paper. Looking into the beam of light, positive Stokes U ($+U$) is oriented 45° counterclockwise from positive Stokes Q and positive Stokes V ($+V$) is defined as clockwise rotation. The rotation angle θ of an optical component used in the rotation Mueller matrix (see Section 4.1) and the angle of linear polarization φ are defined counterclockwise when looking into the beam of light.

This definition of the Stokes parameters can also be understood from six flux measurements performed with ideal polarizers (Hansen & Travis, 1974):

$$I = F_{0^\circ} + F_{90^\circ} \tag{2.2}$$

$$Q = F_{0^\circ} - F_{90^\circ} \tag{2.3}$$

$$U = F_{45^\circ} - F_{135^\circ} \tag{2.4}$$

$$V = F_{\mathrm{L}} - F_{\mathrm{R}} \tag{2.5}$$

where F is the flux measured with the transmission axis of an ideal linear polarizer oriented 0°, 45°, 90° or 135° counterclockwise with respect to the positive Stokes Q-axis when looking into the beam of light, or with a left-handed (L; clockwise in Figure 2.1) or right-handed (R; counterclockwise in Figure 2.1) ideal circular polarizer.

A Stokes vector can be normalized by dividing all its Stokes parameters by the total intensity I:

$$\boldsymbol{S} = \begin{bmatrix} 1 \\ q \\ u \\ v \end{bmatrix} \tag{2.6}$$

with q, u and v the normalized Stokes parameters. The linearly polarized intensity I_{lin} is defined as (Tinbergen, 2005):

$$I_{\text{lin}} = \sqrt{Q^2 + U^2} \tag{2.7}$$

The degree of linear polarization (DoLP) P then follows as:

$$P = \frac{I_{\text{lin}}}{I} = \frac{\sqrt{Q^2 + U^2}}{I} = \sqrt{q^2 + u^2} \tag{2.8}$$

where P equals 0 (or 0%) for non-linearly polarized light and 1 (or 100%) for fully linearly polarized light. P has a value between 0 and 1 for partially linearly polarized light. Finally, the angle of linear polarization (AoLP) φ is computed as (see Figure 2.1):

$$\varphi = \frac{1}{2} \arctan\left(\frac{U}{Q}\right) = \frac{1}{2} \arctan\left(\frac{u}{q}\right) \tag{2.9}$$

2.2 Optical path and polarization measurements with SPHERE/IRDIS

The Stokes parameters of a beam of light will generally change upon interaction with optical elements, such as mirrors and lenses. Hence, when measuring Stokes parameters, we have to know the optical path the light followed before it reached the detector. The optical path of the complete optical system, .i.e. the Unit Telescope (UT) and SPHERE/IRDIS, is shown in Figure 2.2. This Figure only shows the components relevant for polarimetric measurements.

During an observation, light is collected by the concave hyperbolic primary mirror (M1) of the alt-azimuth mounted UT (ESO, 2014). M1 reflects the light to the convex hyperbolic secondary mirror (M2) suspended at the top of the telescope tube. The light is reflected by M2 to the flat tertiary mirror (M3) that is inclined at 45° with respect to the incoming beam of light. M3 then sends the light exactly along the altitude axis into the Nasmyth focus where SPHERE is located. All three mirrors of the UT are made of aluminum.

The light entering SPHERE passes a system that can feed the instrument with light from an internal light source through optic fibers to enable internal calibration and flat-field measurements (Roelfsema et al., 2010; Wildi et al., 2009). The light beam subsequently hits the pupil tip-tilt mirror (PTTM or M4) of SPHERE's extreme adaptive optics (AO) system (Siebenmorgem et al., 2014). M4 is the only aluminum mirror in SPHERE; all the other mirrors are coated with protected silver. M4 is inclined at 45° and sends the beam through a wheel with a linear polarizer with its transmission axis aligned vertical, i.e. perpendicular to the Nasmyth platform (Wildi et al., 2009). This calibration polarizer is only used for calibration measurements and is not inserted during science observations.

The light beam then passes through another wheel which can insert the half wave plate (HWP) (Siebenmorgem et al., 2014)[1]. The HWP delays the component of light linearly polarized parallel to its so-called optical axis with respect to the component linearly polarized perpendicular to it, ideally causing a relative phase shift (retardance) between the components of 180° or half a wavelength. This causes the HWP to reflect the angle of linear polarization of the incident light across its optical axis (hence light polarized parallel or perpendicular to the optic axis in unaffected by the HWP). By rotating the HWP, the angle of linear polarization of the incident light can thus be changed to any angle.

Subsequently, the beam of light passes the image derotator (Bazzon et al., 2012; Siebenmorgem et al., 2014), which is an assembly of three mirrors that can rotate about the axis through the centers of the inclined mirrors (a so-called K-mirror). The derotator reflects the image and the angle of linear polarization across the plane perpendicular to its plane of reflection that passes through its rotation axis. By rotating the derotator, the image can be rotated by any angle.

After the derotator, the light beam passes six mirrors of the extreme AO system, which are all at small angle of incidence (Siebenmorgem et al., 2014). The light beam then reaches a dichroic mirror that transmits the near-infrared light and that reflects the visible light towards ZIMPOL and the wavefront sensor of the AO system. The transmitted beam passes the atmospheric dispersion corrector (ADC), a wheel containing coronagraphs and a wheel containing a mirror and different dichroic mirrors. The mirror can be inserted to allow measurements to be made by IRDIS only. When IRDIS and IFS perform measurements

[1] Although ZIMPOL uses three half wave plates, IRDIS uses only one.

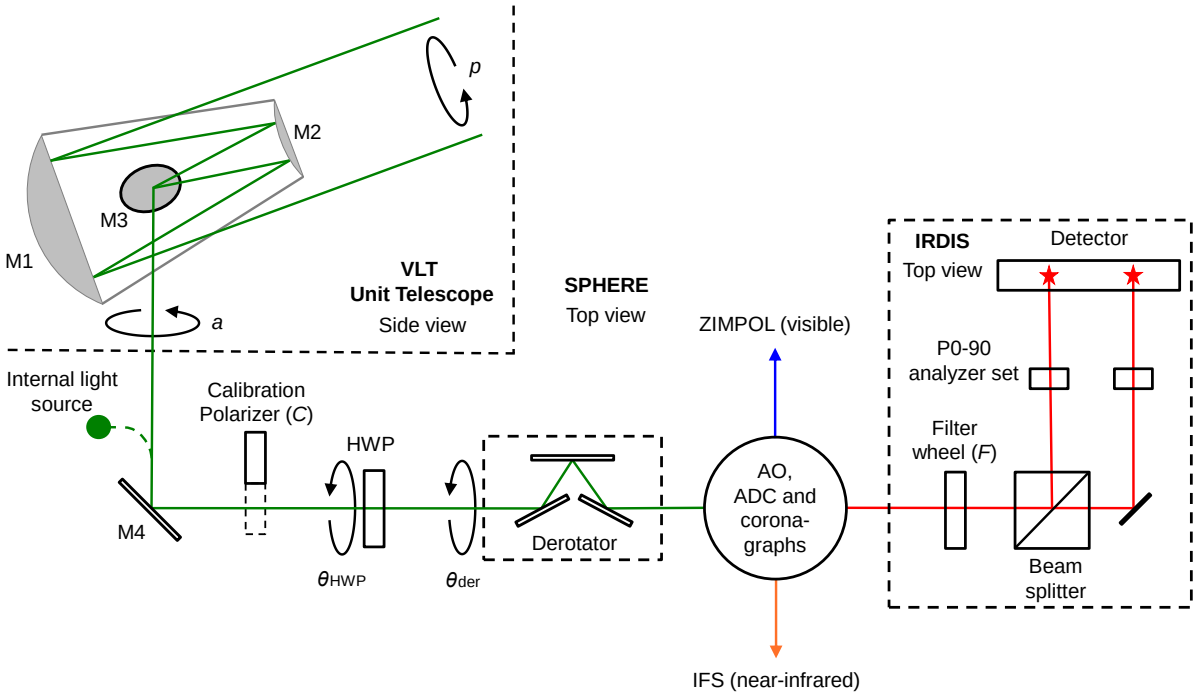

Figure 2.2: Overview of the optical path of the complete optical system, .i.e. the Unit Telescope (UT) and SPHERE/IRDIS, showing only the components relevant for polarimetric measurements. The green beam shows the light before color filters are applied, the blue beam represents the visible light to ZIMPOL and the red and orange beams show the near-infrared light to IRDIS and IFS, respectively (with the near-infrared light of shorter wavelengths to IFS). The black arrows indicate the astronomical target's parallactic angle *p*, the telescope's rotation with the altitude angle *a*, and the rotation of the HWP and derotator with the angles θ_{HWP} and θ_{der}, respectively. The vertical direction, i.e. perpendicular to the Nasmyth platform, points out of the paper.

simultaneously, one of the dichroic mirrors can be used to reflect the near-infrared light of longer wavelengths to IRDIS and to transmit light of shorter wavelengths to IFS.

The optical components of IRDIS are located within a cryostat cooled to 100 K (Dohlen et al., 2008). The light beam entering IRDIS passes a filter wheel containing various narrow-band filters and broad-band filters (Y-, J-, H- and K_s-band[2]; see Table 2.1) and a wheel containing stops (e.g. the Lyot stop) (Siebenmorgem et al., 2014). Subsequently, the light is split into parallel beams by a combination of a (non-polarizing) beam splitter and a mirror. The light beams then pass through a wheel containing two pairs of polarizers with orthogonal transmission axes (the analyzer set) after which the beams strike the same detector to form to adjacent images. The P0-90 analyzer set has the transmission axes of the polarizers at 0° (left detector half) and 90° (right detector half) with respect to the vertical, i.e. perpendicular to the Nasmyth platform. The P45-135 analyzer set has the transmission axes at 45° (left detector half) and 135° (right detector half). The P45-135 analyzer set is not used for science observations however, as measurements with it (contrary to measurements with the P0-90 analyzer set) suffer from severe loss of signal due to strong modification of the polarization signal by the many reflections in the optical path (see Section 4.1).

During science observations, the field of view rotates with the parallactic angle of the target being observed and the altitude angle of the telescope, because SPHERE is on the Nasmyth platform of the alt-azimuth mounted UT. With the derotator in field-tracking mode, the derotator rotates to correct for both the parallactic and altitude rotation, thereby keeping the image with north up on the detector and preventing smearing of the image. In pupil-tracking mode the derotator only compensates for the altitude angle, so that the image

[2] In this thesis, only the broadband filters are considered.

Table 2.1: Central wavelength and bandwidth of the broad-band filters available for IRDIS polarimetry (Siebenmorgem et al., 2014).

Filter	Central wavelength (nm)	Bandwidth (nm)
BB_Y	1042.5	139
BB_J	1257.5	197
BB_H	1625.5	291
BB_K_s	2181.3	313.5

rotates with the parallactic angle over the detector, but the optics of the instrument and telescope remain fixed with respect to the detector, allowing for angular differential imaging (ADI) to be performed. Finally, the derotator angle can be given an offset to rotate the image on the detector to any desired angle.

With polarimetric measurements in field-tracking mode, the HWP rotates such that after the derotator positive Stokes Q is also kept with north up on the detector. The same applies when the derotator angle has been given an offset, allowing for convenient (software) derotation of the image during the data reduction process. The HWP control law for pupil-tracking (see Section 6.1) that is required for measurements combining ADI and polarimetry is yet to be implemented.

In principle, Stokes Q can be determined from the intensity difference of the left and right images on the detector when using the P0-90 analyzer set (see Equation 2.3). As IRDIS is a dual-beam system, the opposite polarization directions are recorded simultaneously and therefore the errors due to left-over seeing effects that are not removed by the AO system are suppressed (Canovas et al., 2011). However, such measurements will still be inaccurate due to differential effects such as flat-fielding errors, differential aberrations, transmission differences between the two channels of the beam splitter and the analyzer set, and instrumental polarization (IP). IP is the polarization signal induced by the optics of the instrument (IP is thus part of the polarimetric response) and can not only change the polarization of polarized objects by a few percent, but it can also make unpolarized sources appear a few percent polarized if not accounted for.

To remove these errors, a second measurement is performed with the HWP rotated 45°, so that the incident angle of linear polarization rotates 90°. This way, the orthogonal polarization components are interchanged when passing through the optical path downstream of the HWP. With this so-called beam switching the above errors can be averaged out in a double difference (Bagnulo et al., 2009):

$$Q_{\mathrm{DD}} = \frac{1}{2}\left[\left(F_{0^\circ}^{0^\circ} - F_{90^\circ}^{0^\circ}\right) - \left(F_{0^\circ}^{45^\circ} - F_{90^\circ}^{45^\circ}\right)\right] \tag{2.10}$$

where the subscripts refer to the angle of the transmission axes of the polarizers and the superscripts to the change in the HWP angle. IP created downstream from the half-wave plate (HWP) is effectively removed by calculating this double difference, but the combined IP of the telescope and M4 and the IP of the HWP or derotator when they rotate between measurements, cannot be removed.

The total intensity I can be computed from the double sum of the same measurements:

$$I_{\mathrm{DD}} = \frac{1}{2}\left(F_{0^\circ}^{0^\circ} + F_{90^\circ}^{0^\circ} + F_{0^\circ}^{45^\circ} + F_{90^\circ}^{45^\circ}\right) \tag{2.11}$$

And finally, the normalized Stokes parameter q can be calculated:

$$q_{\mathrm{DD}} = \frac{Q_{\mathrm{DD}}}{I_{\mathrm{DD}}} \tag{2.12}$$

To also determine Stokes U, measurements are performed with the HWP offset by 22.5° and 67.5°, so that the angle of linear polarization of the incident light rotates by 45° and 135°, and the incident Stokes U passes the instrument as Q and can be measured by the P0-90 analyzer set:

$$U_{\mathrm{DD}} = \frac{1}{2}\left[\left(F_{0^\circ}^{22.5^\circ} - F_{90^\circ}^{22.5^\circ}\right) - \left(F_{0^\circ}^{67.5^\circ} - F_{90^\circ}^{67.5^\circ}\right)\right] \tag{2.13}$$

$$I_{\mathrm{DD}} = \frac{1}{2}\left(F_{0^\circ}^{22.5^\circ} + F_{90^\circ}^{22.5^\circ} + F_{0^\circ}^{67.5^\circ} + F_{90^\circ}^{67.5^\circ}\right) \tag{2.14}$$

$$u_{\mathrm{DD}} = \frac{U_{\mathrm{DD}}}{I_{\mathrm{DD}}} \tag{2.15}$$

Note that measurements of Stokes U are taken with the P0-90 analyzer set with a HWP rotation, and not with the P45-135 analyzer set, as such measurements suffer from severe loss of signal due to the strong modification of the polarization signal by the many reflections in the optical path (see Section 4.1).

3 Polarimetric sensitivity of IRDIS

IRDIS' dual-beam polarimetric mode is primarily used for high-contrast imaging of circumstellar disks using polarimetric differential imaging (PDI). However, by combining angular differential imaging (ADI) with polarimetry, exoplanetary polarization signals could be detected for the first time through direct imaging, providing additional information on the composition and structure of planetary atmospheres that cannot be obtained with spectroscopy. Because the degree of linear polarization of exoplanets at near-infrared wavelengths will generally only be between a few tenths of a percent and a percent, the aim is to achieve a polarimetric sensitivity, i.e. the noise level in the degree of linear polarization, of $\sim 0.1\%$. In Section 3.1 of this Chapter, the working principle of the combination of ADI and polarimetry will be outlined. The polarimetric sensitivity of IRDIS will subsequently be estimated in Section 3.2.

3.1 Combining ADI and polarimetry

Direct imaging of exoplanets is very challenging, because the contrast between a star and an orbiting planet is huge (several orders of magnitude) and, unless the planet is at a large angular separation from the star, the point spread function (PSF) of the much brighter star washes out that of the planet. In addition, time-varying atmospheric seeing on Earth produces random speckles with a similar morphology to a planet signal (also when using a coronagraph, although at a reduced level), obscuring possible exoplanet signals and making it hard to differentiate between a speckle and a real signal (Marois et al., 2006). One might expect that these speckles would average out and that the exoplanet would be revealed with sufficiently long integrations in field-tracking mode, i.e. when the derotator keeps the image with north up on the detector to prevent smearing of the image. However, in reality the noise pattern of the star's point spread function (PSF) becomes quasi-static, because the telescope and instrument optics have imperfections and the alignment of the optics varies slowly with time (e.g. because the telescope structure deflects under its own weight while it tracks the target). Moreover, this noise pattern rotates with respect to the detector during field-tracking. The noise can be reduced with a factor ~ 4 by subtracting a reference PSF from a nearby star, but the attainable sensitivity is then still insufficient to detect exoplanets.

With angular differential imaging (ADI), the star's PSF can be subtracted more effectively, enhancing the attainable sensitivity. ADI requires observations to be performed in pupil-tracking mode, in which the derotator only compensates for the altitude angle, so that the image rotates with the parallactic angle over the detector. As a result, the optics of the instrument and telescope remain fixed with respect to the detector, improving the stability of the quasi-static noise pattern, while the PSF's of possible exoplanets are smeared out (Marois et al., 2006). With ADI, a reference PSF is constructed by combining all images of a series of exposures, and then subtracted from the individual exposures to remove the quasi-static noise pattern. With sufficient rotation of the field of view, the contribution of possible exoplanets to the reference PSF is very small, so that their signals are still present in the exposures. Subsequently, the PSF subtracted exposures are software derotated to align the field of view and then median-combined, so that the planet signal adds up, while at the same time the noise is further averaged down. Various algorithms, such as Principal Component Analysis (PCA), have been devised that optimize the removal of the quasi-static noise pattern with a reference PSF and reduce the unstable noise close to the star (Lafrenière et al., 2007; Marois, Macin-

tosh, & Véran, 2010; Galicher et al., 2011; Brandt et al., 2013; Marois et al., 2014; Amara & Quanz, 2012; Meshkat et al., 2014; Soummer et al., 2012). Zurlo et al. (2016) and de Juan Ovelar et al. (submitted) attain a $\sim$ 2.5 orders of magnitude improvement in sensitivity after performing ADI with PCA on observations of HR 8799 with SPHERE/IRDIS and the Very Large Telescope (VLT) instrument NaCo, respectively, revealing the orbiting planets.

The IRDIS observations by Zurlo et al. (2016) took advantage of SPHERE's advanced adaptive optics system, coronagraphy and ADI with PCA to detect HR 8799's planets with huge signal-to-noise ratio (*SNR*). In K1- and K2-band, *SNR*'s of $\sim$ 200 are reached for some planets after observing almost 2 hours. Considering that the degree of linear polarization of hot exoplanets at near-infrared wavelengths is expected to generally be on the order of 1% (de Kok et al., 2011), combining ADI with polarimetry (de Juan Ovelar et al., submitted) could enable the first ever direct detection of exoplanetary polarization signals. By using IRDIS' dual-beam polarimetric mode, differential effects that severely limit the polarimetric sensitivity (e.g. flat-fielding errors, differential aberrations and seeing) and the instrumental polarization (IP) downstream of the HWP can be eliminated (see Section 2.2). Combining ADI with polarimetry could also further suppress the speckle noise, especially at small angular separations from the star, because the speckles originate from starlight that is in principle unpolarized. For the best performance, a new HWP control law (see Section 6.1) has to be implemented that keeps Stokes Q with north up on the detector during pupil-tracking.

3.2 Estimation of polarimetric sensitivity

Using HR 8799 as study case, IRDIS' polarimetric sensitivity when combining ADI and polarimetry is estimated in two independent ways. For the first estimate, the results of observations combining ADI and polarimetry with VLT/NaCo, in an attempt to measure the polarization signals of HR 8799's planets (de Juan Ovelar et al., submitted), are compared to (non-polarimetric) coronagraphic ADI observations of the same planets with IRDIS (Zurlo et al., 2016). Although the planet's polarization signals were not detected with the NaCo observations, IRDIS' polarimetric sensitivity (in Stokes q) can be estimated as:

$$q_{\text{noise,IRDIS}} = \frac{SNR_{\text{NaCo}}}{SNR_{\text{IRDIS}}} q_{\text{noise,NaCo}} \tag{3.1}$$

where $q_{\text{noise,IRDIS}}$ is the noise level in Stokes q at the planet's position (polarimetric sensitivity) predicted for IRDIS, SNR_{NaCo} and SNR_{IRDIS} are the intensity signal-to-noise ratios of the planet detections with NaCo and IRDIS, respectively, and $q_{\text{noise,NaCo}}$ is the noise level in Stokes q at the planet position (polarimetric sensitivity) attained with NaCo.

With 36 min of NaCo observations in K_s-band, *SNR*'s equal to 13.6 and 6.6 were reached for planet b and c, respectively, whereas planet d and e were not detected (de Juan Ovelar et al., submitted). The noise levels in Stokes q at the positions of planet b and c were 7.7% and 3.0%, respectively. With IRDIS, after nearly 2 hours of observations in K2-band, *SNR*'s of 140 and 220 were reached for planet b and c, respectively (Zurlo et al., 2016). Using this data, the polarimetric sensitivities of IRDIS are estimated and shown in Table 3.1. The estimated polarimetric sensitivity for planet c complies with the required sensitivity of $\sim$ 0.1%, while for planet b, the requirement is not met.

Table 3.1: Estimates of the polarimetric sensitivity in Stokes q attainable by IRDIS when observing HR8799's planets.

Planet	Sensitivity from NaCo to IRDIS (%)	Sensitivity from IRDIS ADI + polarimetry simulation (%)
b	0.75	1.53
c	0.09	0.56
d	-	0.12
e	-	0.10

A second, independent estimate of the polarimetric sensitivity of IRDIS when combining ADI and polarimetry is obtained by simulating single-beam polarimetric measurements with the (non-polarimetric) ADI data of HR 8799's planets taken with IRDIS in K2-band (Zurlo et al., 2016). The even and odd frames of this data set are

reduced with PCA (specifically KLIP; Soummer et al., 2012)[1], and the sum and difference of the two results is computed to simulate images of the total intensity (I) and one of the Stokes parameters (e.g. Q), respectively (see Figure 3.1). Because of SPHERE's advanced adaptive optics system and the use of PCA, the noise in the total intensity image is primarily read-out and/or photon noise and almost no residual speckles can be seen (Figure 3.1 (left)). Further suppression of speckle noise is therefore limited in the image of one of the Stokes parameters (Figure 3.1 (right)). However, at small angular separations from the star, or in bad seeing conditions, the simultaneous recording of opposite polarization directions with dual-beam polarimetry can yield an order of magnitude improvement in polarimetric sensitivity (Keller et al., 2010; Hinkley et al., 2009). The polarimetric sensitivities (in Stokes q) are estimated by dividing the pixel values at the position of the planet in the total intensity image by the corresponding pixel values in the image of one of the Stokes parameters[2]. The results are shown in Table 3.1. For planets d and e, the estimated polarimetric sensitivity complies with the required sensitivity of $\sim 0.1\%$, while the requirement is not met for planets b and c.

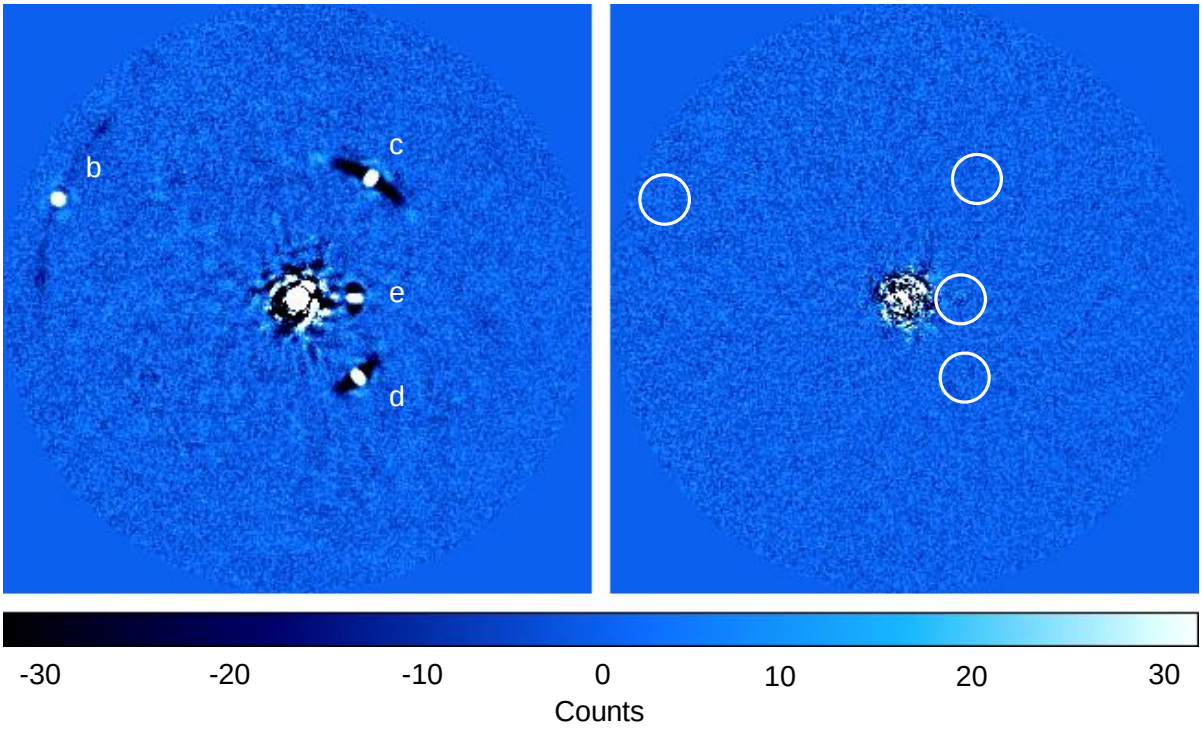

Figure 3.1: IRDIS K2-band images of HR 8799's planets. Left: total intensity image (I). Right: simulated single-beam polarimetric image of one of the Stokes parameters (e.g. Q), assuming zero planet polarization.

Although the NaCo and IRDIS data sets used for the first estimate of the polarimetric sensitivity are both reduced with PCA, the setups of the instruments, exposure times and color filters (K_s- vs. K2-band) were different. For the second estimate of the sensitivity, no real polarimetric data was used, but it was simulated. Also, for both estimates, the polarimetric sensitivity was estimated as the noise level in Stokes q rather than in the degree of linear polarization. Therefore, the values in Table 3.1 should be regarded as order of magnitude estimates of the attainable polarimetric sensitivities. Assuming the estimates are accurate, it is expected that SPHERE/IRDIS can reach sub-percent polarimetric sensitivity by combining extreme adaptive optics, coronagraphy, ADI with PCA and dual-beam polarimetry. Provided the degree of linear polarization of the exoplanets is $\sim 1\%$, this means that the polarization signals of planets c, d and e can be detected with high confidence level, and that of planet b only when its degree of linear polarization is very high ($\sim 5\%$). The real polarimetric sensitivity of IRDIS can in the end only be established by performing actual measurements combining ADI and polarimetry.

[1] The PCA reduction has been performed by Jos de Boer.
[2] As a non-coronagraphic total intensity image of the star was not available, a contrast curve could not be constructed.

4 Polarimetric response and accuracy of the instrument

With a predicted sub-percent polarimetric sensitivity, it is expected that SPHERE/IRDIS can detect the polarization signals of exoplanets. To derive the exoplanet's true degree and angle of linear polarization from a measurement, a model is needed that describes the polarimetric response of the complete optical system, i.e. the modification of the polarization signal induced by the telescope and instrument. For IRDIS, this optical system is complex and has many rotating components. In this Chapter, we estimate the model parameters of the optical path downstream of M4 from measurements using the internal light source. Subsequently, in Chapter 5, we estimate those of the telescope and M4 from observations of an unpolarized standard star.

In Section 4.1 of this Chapter, the model describing the complete optical system will be presented. Subsequently, in Section 4.2, the measurements with the internal light source and the data reduction will be discussed. The estimation of the model parameters and the results will be described in Section 4.3 and the polarimetric accuracy and uncertainty in estimated parameters will be examined in Section 4.4.

4.1 Model of complete optical system

The polarimetric response of an optical component can be represented by a 4×4 Mueller matrix M:

$$\boldsymbol{S}_{\text{out}} = M\boldsymbol{S}_{\text{in}}$$

$$\begin{bmatrix} I_{\text{out}} \\ Q_{\text{out}} \\ U_{\text{out}} \\ V_{\text{out}} \end{bmatrix} = \begin{bmatrix} I \to I & Q \to I & U \to I & V \to I \\ I \to Q & Q \to Q & U \to Q & V \to Q \\ I \to U & Q \to U & U \to U & V \to U \\ I \to V & Q \to V & U \to V & V \to V \end{bmatrix} \begin{bmatrix} I_{\text{in}} \\ Q_{\text{in}} \\ U_{\text{in}} \\ V_{\text{in}} \end{bmatrix} \tag{4.1}$$

where $\boldsymbol{S}_{\text{in}}$ is the incident Stokes vector, $\boldsymbol{S}_{\text{out}}$ is the exiting Stokes vector and M is the Mueller matrix describing the optical component. A nonzero value for an element $A \to B$ of the Mueller matrix implies that an A-component is converted to a B-component. The Mueller matrix of an optical element usually depends on the wavelength of the light, the angle of incidence and the direction of propagation through the optical component. The polarimetric response of a sequence of optical components $n = 1, 2, \ldots, N$ can be described as a multiplication of Mueller matrices as follows:

$$\boldsymbol{S}_{\text{out}} = M_N M_{N-1} \cdots M_n \cdots M_2 M_1 \boldsymbol{S}_{\text{in}} \tag{4.2}$$

When an optical component is rotated around the incident beam of light by an angle θ (see Figure 2.1) while keeping the angle of incidence the same, the reference frame of the incident light is rotated to that of the optical element by the rotation Mueller matrix $T(\theta)$, after which the Mueller matrix of the optical component is applied. The reference frame can then be rotated back to the original one with the rotation matrix $T(-\theta)$:

$$M_\theta = T(-\theta) M T(\theta) \tag{4.3}$$

where M_θ is the rotated component Mueller matrix and $T(\theta)$ is the rotation matrix:

$$T(\theta) = \begin{bmatrix} 1 & 0 & 0 & 0 \\ 0 & \cos(2\theta) & \sin(2\theta) & 0 \\ 0 & -\sin(2\theta) & \cos(2\theta) & 0 \\ 0 & 0 & 0 & 1 \end{bmatrix} \tag{4.4}$$

The polarimetric response of the complete optical system, i.e. the telescope and the instrument, is represented by:

$$\boldsymbol{S}_{\mathrm{meas}} = M_{\mathrm{sys}} \boldsymbol{S}_{\mathrm{in}} \tag{4.5}$$

with $\boldsymbol{S}_{\mathrm{in}}$ the Stokes vector incident on the telescope, M_{sys} the Mueller matrix describing the complete optical system and $\boldsymbol{S}_{\mathrm{meas}}$ the measured Stokes vector. To describe the complete optical system, it is not necessary to write M_{sys} as the sequence of all optical components (see Equation 4.2). Instead, components sharing the same reference frame can be grouped, so that M_{sys} can be described with the following five Mueller matrices (see Section 2.2 and Figure 2.2):

- M_{UT}, the three mirrors of the Unit Telescope (UT)
- M_{M4}, the first mirror of SPHERE, M4
- M_{HWP}, the near-infrared half wave plate (HWP)
- M_{der}, the three mirrors of the derotator
- M_{CI}, the optical path downstream of the derotator (CPI and IRDIS), including the analyzer set

Taking into account the rotations between these grouped components, the complete optical system can be described by (see Figure 2.2):

$$\boldsymbol{S}_{\mathrm{meas}} = \begin{bmatrix} I_{\mathrm{meas}} \\ Q_{\mathrm{meas}} \\ U_{\mathrm{meas}} \\ V_{\mathrm{meas}} \end{bmatrix} = M_{\mathrm{CI}} T(-\Theta_{\mathrm{der}}) M_{\mathrm{der}} T(\Theta_{\mathrm{der}}) T(-\Theta_{\mathrm{HWP}}) M_{\mathrm{HWP}} T(\Theta_{\mathrm{HWP}}) M_{\mathrm{M4}} T(a) M_{\mathrm{UT}} T(p) \boldsymbol{S}_{\mathrm{in}} \tag{4.6}$$

with p the astronomical target's parallactic angle (due to the Earth's rotation, the telescope rotates around its optical axis as seen from the celestial reference frame), a the altitude angle of the telescope (the telescope rotates with respect to the Nasmyth platform where SPHERE is located), and:

$$\Theta_{\mathrm{HWP}} = \theta_{\mathrm{HWP}} + \delta_{\mathrm{HWP}} \tag{4.7}$$

$$\Theta_{\mathrm{der}} = \theta_{\mathrm{der}} + \delta_{\mathrm{der}} \tag{4.8}$$

with θ_{HWP} the HWP angle, θ_{der} the derotator angle, and δ_{HWP} and δ_{der} the to-be-estimated offset angles (due to misalignments) of the HWP and derotator, respectively. $\theta_{\mathrm{HWP}} = 0^\circ$ when the HWP has its fast or slow optic axis aligned with the vertical, i.e. perpendicular to the Nasmyth platform (it is not known nor relevant which optic axis is aligned with the vertical), and $\theta_{\mathrm{der}} = 0^\circ$ when the derotator has its plane of incidence horizontal, i.e. parallel to the Nasmyth platform.

Ideally, the polarimetric response of the component groups would be determined by estimating all 16 elements of the Mueller matrices from calibration measurements that inject many different polarization states into the system. However, with IRDIS, the non-rotatable calibration polarizer can only inject positive Stokes Q, and polarized standard stars are limited in number and have a low degree of linear polarization at near-infrared wavelengths. To limit the number of model parameters to estimate, all component groups are modeled with the Mueller matrix of a linear diattenuator and retarder, M_{com}, that accurately describes (a sequence of) mirrors and the HWP (Trujillo-Bueno et al., 2002; Bass, 1995):

$$M_{\mathrm{com}} = \frac{1}{2} \begin{bmatrix} 1+\epsilon & 1-\epsilon & 0 & 0 \\ 1-\epsilon & 1+\epsilon & 0 & 0 \\ 0 & 0 & 2\sqrt{\epsilon}\cos\Delta & 2\sqrt{\epsilon}\sin\Delta \\ 0 & 0 & -2\sqrt{\epsilon}\sin\Delta & 2\sqrt{\epsilon}\cos\Delta \end{bmatrix} \tag{4.9}$$

For the HWP, M_{com} is defined with the positive Stokes Q-direction parallel to one of the optic axes. For the other groups, it is defined with the positive Stokes Q-direction perpendicular to the plane of incidence of the mirrors. In Equation 6.10, ϵ is the diattenuation, i.e. the different absorption of the perpendicular linearly polarized components of an incident beam of light, and Δ is the retardance (or relative retardation), i.e. the relative phase shift of the perpendicular linearly polarized components. Diattenuation causes instrumental polarization (IP), i.e. the polarization signal induced by the optics of the instrument, with $\epsilon < 1$ resulting in a positive Stokes Q-signal and $\epsilon > 1$ resulting in a negative Stokes Q-signal (ideally $\epsilon = 1$, yielding no IP). Retardance causes cross-talk, i.e. mixing of the polarized Stokes parameters, where ideally $\Delta = 180^\circ$ for the HWP or a mirror (or sequence of an odd number of mirrors such as the Unit Telescope or the derotator). For other values, a Stokes U-signal incident on the component is converted into Stokes V and vice versa. ϵ and Δ depend on the angle of incidence and the wavelength of the light and, for the mirrors, can be computed using the Fresnel equations (see for example Hecht (2002)).

When taking advantage of beam switching with the HWP and computing the Stokes parameters from the double difference (see Section 2.2), differential effects such as flat-fielding errors, differential aberrations and transmission differences do not have to be modeled (to first order). In addition, the IP of all mirrors, dichroics and other components downstream of the derotator are averaged out, because these components have a fixed orientation (except for the atmospheric dispersion corrector (ADC) that can rotate). Also, since the mirrors and dichroics have their plane of incidence approximately horizontal, their retardance is not important if the measurements are taken with the P0-90 analyzer set that only measures Stokes Q[1], assuming the transmission axes of the analyzer set are exactly perpendicular and parallel to the Nasmyth platform. The P45-135 analyzer set that measures Stokes U is not used, because measurements with it suffer from severe loss of signal due to the cross-talk of all the components downstream of the derotator. Therefore, assuming the ADC does not rotate or its effect is negligible, M_{CI} in Equation 4.6 can be set equal to the identity matrix. Besides removing the need to estimate the diattenuation and retardance of the optical components downstream of the derotator, this also means that the model does not need to be updated when one of these component is replaced or when its properties change over time.

Stokes Q (Q_{DD}) and the total intensity (I_{DS}) are computed from the double difference and double sum as follows:

$$Q_{DD} = \frac{1}{2}\left[Q_{meas}(p_1, a_1, \theta_{HWP,1}, \theta_{der,1}) - Q_{meas}(p_2, a_2, \theta_{HWP,2}, \theta_{der,2})\right] \tag{4.10}$$

$$I_{DS} = \frac{1}{2}\left[I_{meas}(p_1, a_1, \theta_{HWP,1}, \theta_{der,1}) + I_{meas}(p_2, a_2, \theta_{HWP,2}, \theta_{der,2})\right] \tag{4.11}$$

where Q_{meas} and I_{meas} are the measured Stokes Q and Stokes I from Equation 4.6, which are functions of the parallactic, altitude, HWP and derotator angles of the first measurements (subscript 1) and the parallactic, altitude, HWP and derotator angles of the second measurement (subscript 2). Finally, the normalized Stokes parameter q_{DD} can be calculated as:

$$q_{DD} = \frac{Q_{DD}}{I_{DS}} \tag{4.12}$$

4.2 Measurements and data reduction

To determine the polarimetric response of the optical path downstream of M4, measurements were taken with the internal light source while rotating the HWP and derotator between exposures. Because the internal light source was used, the normalized Stokes parameters calculated from these measurements can be modeled with only part of the polarimetric response model (see Equations 4.6 to 4.12):

$$\boldsymbol{S}_{meas} = \begin{bmatrix} I_{meas} \\ Q_{meas} \\ U_{meas} \\ V_{meas} \end{bmatrix} = M_{CI}\,T(-\Theta_{der})M_{der}\,T(\Theta_{der})\,T(-\Theta_{HWP})M_{HWP}\,T(\Theta_{HWP})\boldsymbol{S}_{in} \tag{4.13}$$

[1] This refers to Stokes Q in the instrument's reference frame. To measure Stokes Q and U from the celestial reference frame, the HWP is used (see Section 2.2).

$$Q_{\mathrm{DD}} = \frac{1}{2}\left[Q_{\mathrm{meas}}(\theta_{\mathrm{HWP},1}, \theta_{\mathrm{der},1}) - Q_{\mathrm{meas}}(\theta_{\mathrm{HWP},2}, \theta_{\mathrm{der},2})\right] \tag{4.14}$$

$$I_{\mathrm{DS}} = \frac{1}{2}\left[I_{\mathrm{meas}}(\theta_{\mathrm{HWP},1}, \theta_{\mathrm{der},1}) + I_{\mathrm{meas}}(\theta_{\mathrm{HWP},2}, \theta_{\mathrm{der},2})\right] \tag{4.15}$$

$$q_{\mathrm{DD}} = \frac{Q_{\mathrm{DD}}}{I_{\mathrm{DS}}} \tag{4.16}$$

with $\boldsymbol{S}_{\mathrm{in}}$ in this case the Stokes vector incident on the HWP. Note that this part of the model is not a function of the parallactic and altitude angle.

The following data sets were obtained:

- On August 15, 2015, a total of 528 exposures in Y-, J-, H- and K_s-band were taken with the internal light source, calibration polarizer (highly $+Q$-polarized input), HWP and P0-90 analyzer set inserted and with exposure times ranging from 2 s to 6 s (using a neutral density filter after the internal lamp for all exposures). The derotator and HWP were rotated with θ_{der} ranging from 0° to 90° and θ_{HWP} ranging from 0° to 101.25°. This data (hereafter called the polarized source measurements) is used to fit the retardances and offset angles of the HWP and derotator and the normalized Stokes q incident on the HWP.
- On June 12 and 13, 2016, a total of 400 exposures in Y-, J-, H- and K_s-band were taken with the internal light source, HWP and P0-90 analyzer set inserted, but without calibration polarizer (almost unpolarized input), and with exposure times ranging from 2 s to 6 s (using a neutral density filter after the internal lamp for all exposures). The derotator and HWP were rotated with θ_{der} and θ_{HWP} ranging from 0° to 101.25°. This data (hereafter called the unpolarized source measurements, although the source is actually very weakly polarized) is used to fit the diattenuations of the HWP and derotator and the three Stokes parameters of the normalized Stokes vector incident on the HWP.
- On June 12, 2016, internal dark frames were taken with exposure times ranging from 2 s to 6 s.
- On June 13, 2016, internal lamp flat frames were taken in Y-, J-, H- and K_s-band with the corresponding neutral density filter after the internal light source, without the calibration polarizer, HWP or analyzer set inserted and with $\theta_{\mathrm{der}} = 0°$.

The data is reduced as follows:

- Master dark frames are made by taking the median over all dark frames with the same exposure time.
- Normalized master flat frames (see Figure 4.1) are produced by subtracting the master dark frames of the corresponding exposure time from the internal lamp flat frames, applying a sigma-filter to remove hot, dead and random varying pixels (applied two times to remove the bad pixels that are left-over after the first sigma filter because they are adjacent to other bad pixels) and dividing all pixels by the median over two aperture with radii of 100 pixels located in the centers of the frame halves.
- The 928 exposures taken on August 15, 2015 and June 12 and 13, 2016 are reduced by subtracting master dark frames of the right exposure time, dividing by master flats of the correct broadband and neutral density filter, performing sigma-filtering two times and centering them using the outline of the pupil stop (see Figure 4.2 (right)).
- To compute the normalized Stokes parameters, Q- and I-images are constructed from two exposures with the same θ_{der}, broadband filter and setup of calibration polarizer, and with $\theta_{\mathrm{HWP},1}$ and $\theta_{\mathrm{HWP},2}$ (see Equations 4.14 and 4.15) differing 45° in the combinations $[\theta_{\mathrm{HWP},1}, \theta_{\mathrm{HWP},2}]$ = [0°, 45°]; [11.25°, 56.25°]; [22.5°, 67.5°]; [33.75°, 78.75°]; [90°, 45°]; [101.25°, 56.25°] (measurements with θ_{HWP} equal to 45° and 56.25° are used twice). Subsequently, median values of the Q- and I-images are computed in 9 apertures with radii of 100 pixels arranged in a 3 by 3 square covering almost the complete area of the frame. Finally, the median values of Q are divided by the median values of I, yielding 9 normalized Stokes parameters for every combination of θ_{der} and $\theta_{\mathrm{HWP},1}$ (see Equation 4.16). The normalized Stokes parameter have also been computed as the median over the apertures of the normalized Stokes q-images (Q-image divided by I-image), but the difference with the computation above is negligible.

- The diattenuation of the derotator cannot be determined from the normalized Stokes parameters computed above, because the derotator angle is the same for the two exposures used and so the effect of the diattenuation of the derotator is removed in the double difference. Therefore, using the unpolarized source measurements, additional Q- and I-images are constructed from two exposures with the same θ_{HWP} (rather than the same θ_{der}) and with $\theta_{\mathrm{der},1}$ and $\theta_{\mathrm{der},2}$ (see Equations 4.14 and 4.15) differing 45° in the combinations $[\theta_{\mathrm{der},1},\ \theta_{\mathrm{der},2}]$ = [0°, 45°]; [11.25°, 56.25°]; [22.5°, 67.5°]; [33.75°, 78.75°]; [90°, 45°]; [101.25°, 56.25°] (measurements with θ_{der} equal to 45° and 56.25° are used twice). The normalized Stokes parameters are then computed in the same way as described above.

The data reduction yields a total of 6696 data points that will be used to estimate the parameters of the part of the polarimetric response model downstream of M4.

The flux of the measurements with the internal light source is not uniform over the two detector halves, but shows a gradient. This gradient consists of two components: a gradient that depends on the total intensity of the incident light and a gradient that depends on the polarization state of the incident light. The total intensity dependent gradient (see Figure 4.1) has a different strength and orientation for every broadband filter, and is most prominent in K_s-band. It must originate downstream of the derotator, since it does not depend on the derotator or HWP angle. It may be due to imperfect alignment of optical components or differences in transmission or reflectivity over the surface of the components. As the gradient is also present in the lamp flat frames, the flat-field correction applied to the exposures suppresses the gradient. In the Stokes Q-image (actually already in the single difference of two exposures), the total intensity dependent gradient is completely removed (see Figure 4.2), but it is still visible in the double sum image. Therefore, the normalized Stokes parameters depend on the position of the apertures from which they are computed, resulting in an uncertainty in their values.

In the polarized source measurements, the double difference removes the total intensity-dependent gradient, but a polarization dependent gradient remains. This gradient is different in strength and orientation for each exposure and therefore seems to depend on the HWP and/or derotator orientation. As the HWP is close to a focal plane, a likely cause of the polarization dependent gradient is that the HWP retardance is different over the surface of the HWP. The gradient is not visible in the unpolarized source measurements, because the incident light is only very weakly polarized. To take into account the uncertainty in the normalized Stokes parameters due to the total intensity and polarization dependent gradients when estimating the model parameters, the normalized Stokes parameters are calculated in 9 apertures covering almost the complete area of the frame, as described above.

4.3 Estimation of model parameters

To estimate the model parameters from the measurements, non-linear least squares is used. The $n = 6696$ measurements of the normalized Stokes parameter $q_{\mathrm{meas},i}$ (the dependent variables) with $i = 1, 2, \ldots, n$ are modeled with the model function $q_{\mathrm{DD},i}(\boldsymbol{x}_i, \boldsymbol{\beta})$ (see Equation 4.16), where:

$$\boldsymbol{\beta} = \left[\beta_1,\ \beta_2,\ \ldots,\ \beta_m\right] \tag{4.17}$$

is the vector containing the m model parameters to be estimated (the retardances, diattenuations and offset angles of the derotator and HWP, and the Stokes parameters incident on the HWP in all filters), and where (see Figure 2.2):

$$\boldsymbol{x}_i = \left[F_i,\ C_i,\ \theta_{\mathrm{HWP},1,i},\ \theta_{\mathrm{der},1,i},\ \theta_{\mathrm{HWP},2,i},\ \theta_{\mathrm{der},2,i}\right] \tag{4.18}$$

is the vector containing the independent variables of the i-th measurement. F_i is the broadband filter used and C_i indicates whether the measurement is with polarized or unpolarized source (whether the calibration polarizer is inserted). $\theta_{\mathrm{HWP},1}$ and $\theta_{\mathrm{der},1}$ are the HWP and derotator angle, respectively, of the first of the two exposures used to compute q_{DD}, and $\theta_{\mathrm{HWP},2}$ and $\theta_{\mathrm{der},2}$ are the HWP and derotator angle, respectively, of the

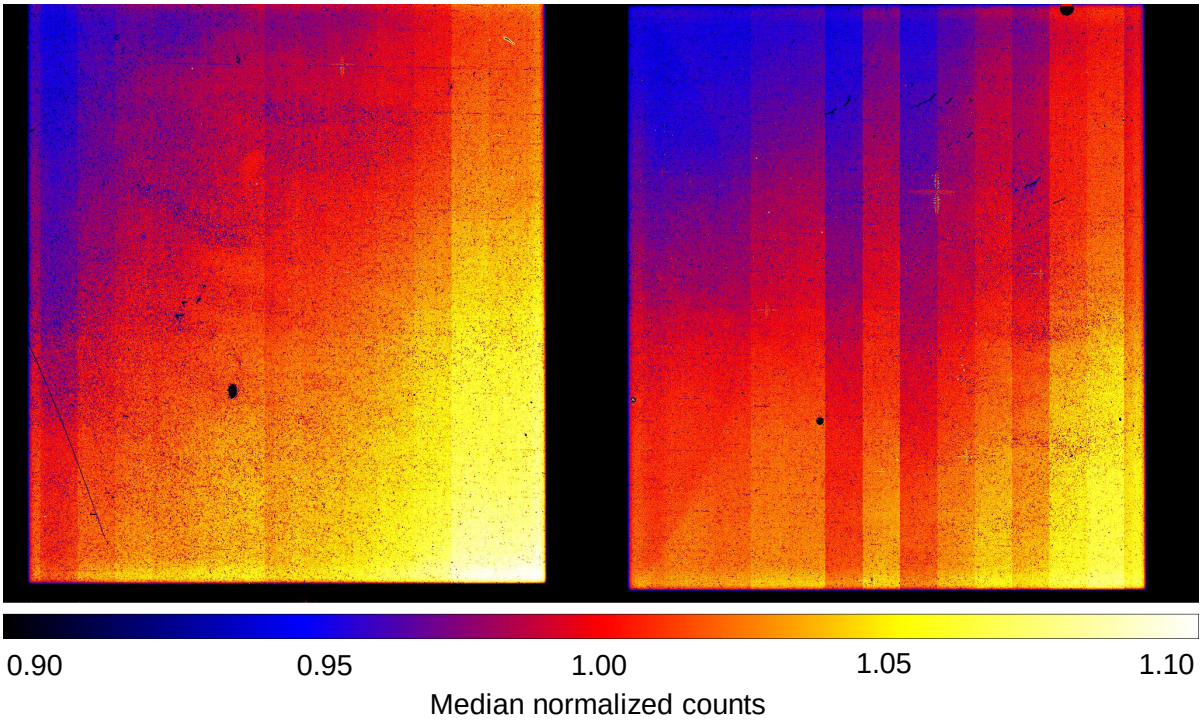

Figure 4.1: Dark-subtracted and sigma-filtered master flat in K_s-band showing the total intensity-dependent gradient on the two frame halves. The gradient has a different strength and orientation for every broadband filter, and is most prominent in K_s-band.

second of the two exposures used to compute q_{DD} (see Equations 4.14 to 4.16)[2].

The model parameter values that best fit the data are found by adjusting the parameter values in β to minimize the sum of squared residuals *SSR*:

$$SSR = \sum_{i=1}^{n} r_i^2 \tag{4.21}$$

with:

$$r_i = q_{\text{meas},i} - q_{DD}(\boldsymbol{x}_i, \beta) \tag{4.22}$$

the residuals of fit. We have written a program that performs this estimation of the model parameters. It allows the user to specify the parameters to be estimated, the initial parameter values, the lower and upper limits of the parameters, the minimization solver type (in this case sequential least squares programming), the maximum number of iterations and the required precision of the fit.

The resulting model parameter values are shown in Table 4.1. In this Table, $q_{\text{in,pol}}$ is the normalized Stokes q incident on the HWP for the polarized source measurements and $q_{\text{in,unpol}}$, $u_{\text{in,unpol}}$ and $v_{\text{in,unpol}}$ are the normalized Stokes parameters incident on the HWP for the unpolarized source measurements. ϵ_{HWP}, Δ_{HWP} and δ_{HWP}, and Δ_{der}, ϵ_{der} and δ_{der} are the diattenuations, retardances and angle offsets of the HWP and

[2]The variables contained by $\boldsymbol{x}_i$ are obtained from the headers of the .fits-files of the measurements. The HWP and derotator angles are computed from the headers as (with n an integer):

$$\theta_{\text{HWP}} = INS4.DROT3.BEGIN - 152.15^\circ + n \cdot 180^\circ \tag{4.19}$$

$$\theta_{\text{der}} = INS4.DROT2.BEGIN + n \cdot 360^\circ \tag{4.20}$$

with n an integer.

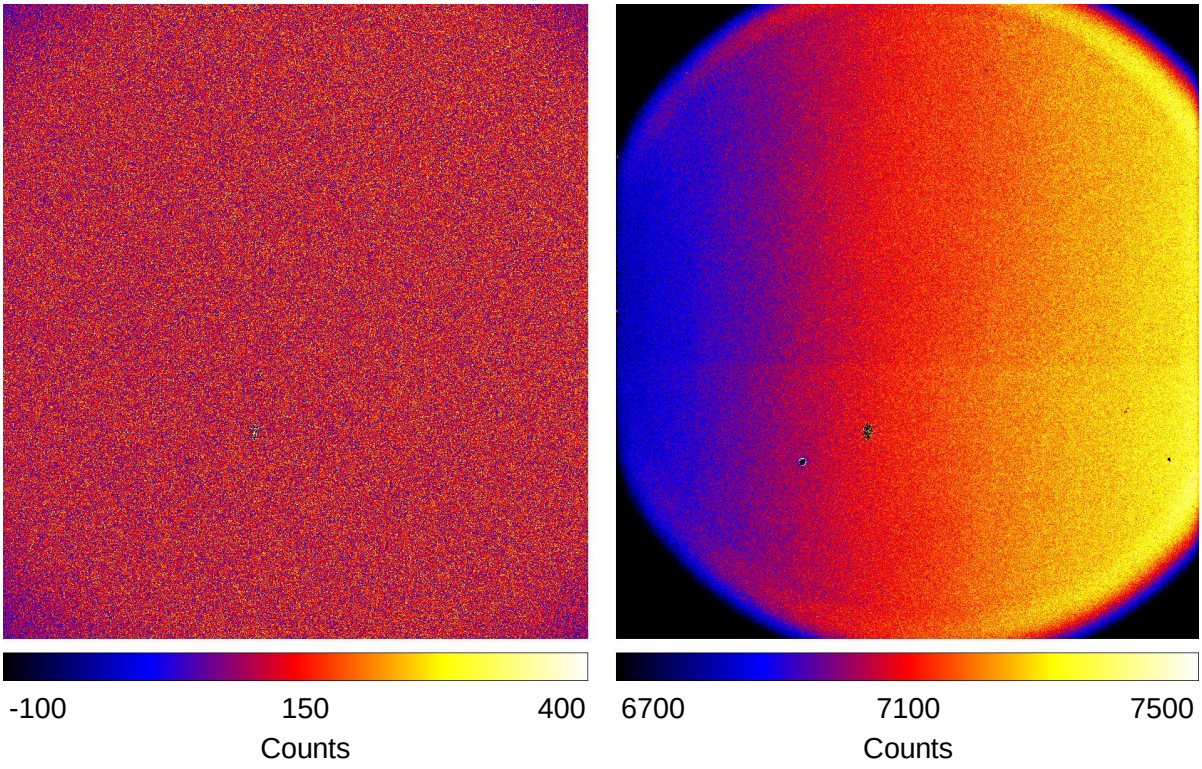

Figure 4.2: Stokes *Q*-images of the polarized source (left) and unpolarized source measurements (right) in K_s-band. Both images are taken with $\theta_{der} = 0°$, $\theta_{HWP,1} = 0°$ and $\theta_{HWP,2} = 45°$. The double difference completely removes the total intensity-dependent gradient and so the left image shows no left-over structure, as the incident light was only very weakly polarized. The right image on the other hand still shows structure, because the double difference does not remove the polarization dependent gradient present in these measurements with highly polarized incident light.

derotator, respectively.

The program has not estimated all parameters simultaneously, because then the estimates of ϵ_{HWP} and ϵ_{der} are dominated by the polarized source measurements, which have larger residuals than the unpolarized source measurements. To make sure ϵ_{HWP} and ϵ_{der} are estimated from the more suitable unpolarized source measurements, the program first estimates $q_{in,pol}$, Δ_{HWP}, δ_{HWP}, Δ_{der} and δ_{der} with the polarized source measurements, then $q_{in,unpol}$, $u_{in,unpol}$, $v_{in,unpol}$, ϵ_{HWP} and ϵ_{der} with the unpolarized source measurements, and repeats these two model fits until convergence. Moreover, only $q_{in,pol}$ is estimated, and not $u_{in,pol}$ and $v_{in,pol}$, because it is assumed that the transmission axis of the linear calibration polarizer is aligned vertical (perpendicular to the Nasmyth platform) and it is very unlikely for the light to have a circularly polarized component after passing a linear polarizer.

Figure 4.3 shows the plots of the ideal, measured and fitted normalized Stokes parameters of the polarized source measurements in H-band as a function of HWP and derotator angle and Figure 4.4 shows the corresponding residuals of fit. The ideal curves are computed with 100% linearly polarized light incident on the HWP, no angle offsets and the HWP and derotator retardance equal to 180°. Measured and fitted normalized Stokes parameters of the unpolarized source measurements in H-band are displayed in Figures 4.5 (regular beam switching with the HWP) and 4.7 (beam switching with the derotator), respectively, with the corresponding residuals in Figures 4.6 and 4.8, respectively. The ideal curves, with completely unpolarized light incident on the HWP and the HWP and derotator diattenuation equal to 1, are not shown, as they coincide with the x-axis of the graphs.

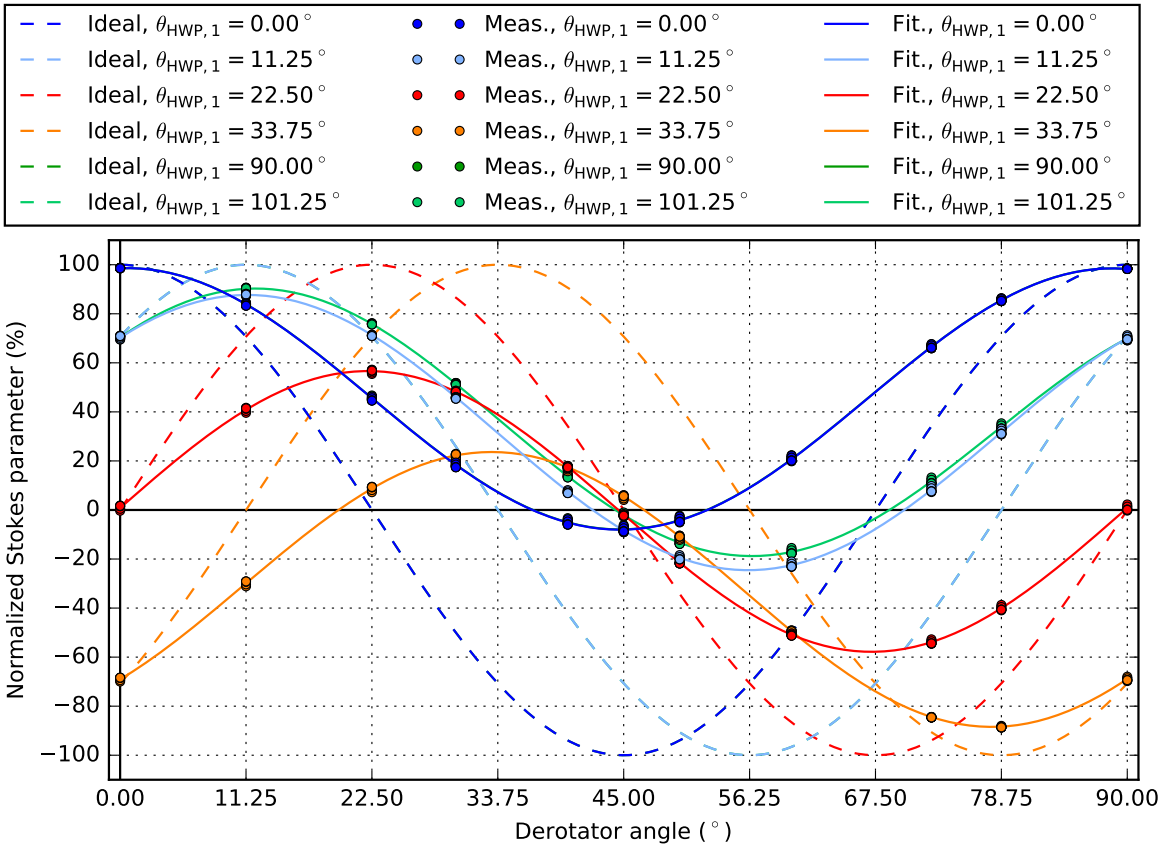

Figure 4.3: Ideal, measured and fitted normalized Stokes parameters of the polarized source measurements in H-band as a function of HWP and derotator angle.

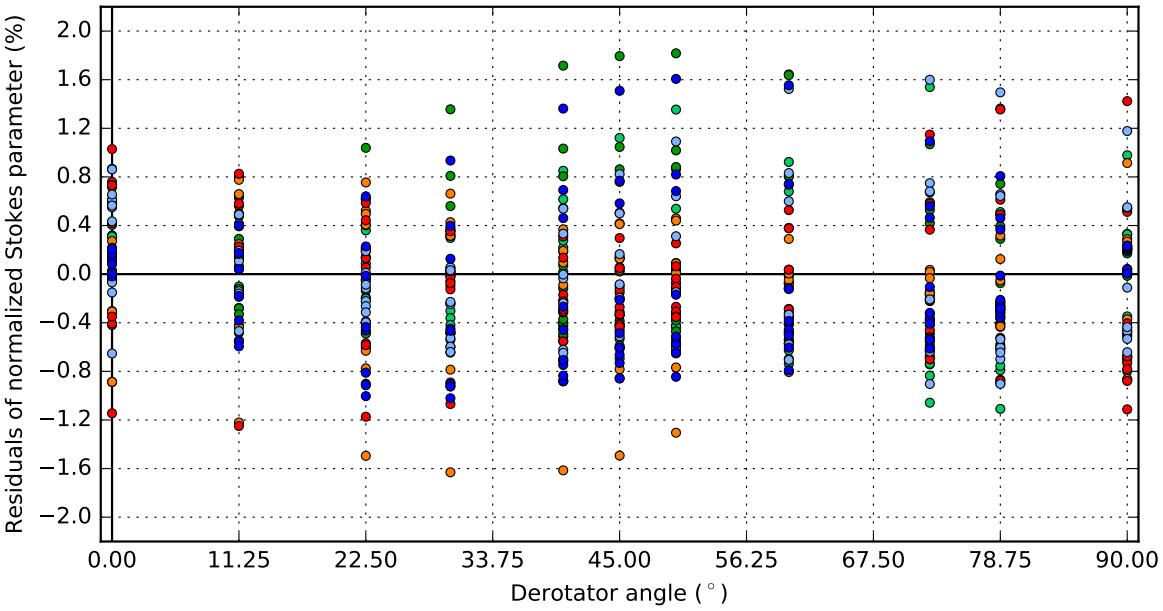

Figure 4.4: Residuals of the normalized Stokes parameters of the polarized source measurements in H-band as a function of HWP and derotator angle.

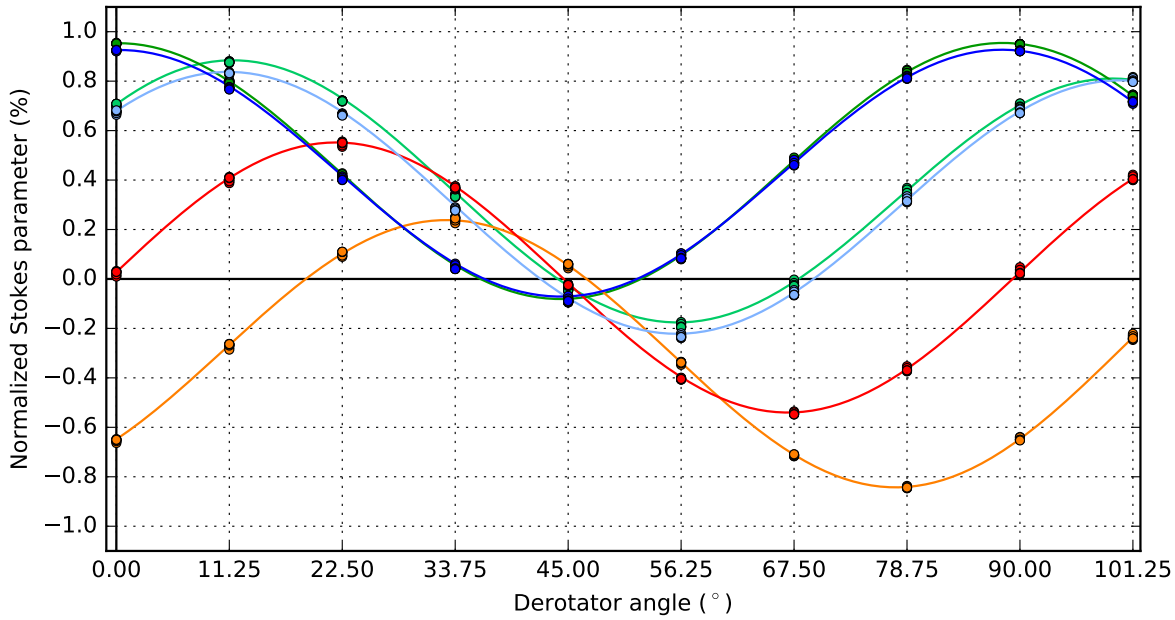

Figure 4.5: Measured and fitted normalized Stokes parameters of the unpolarized source measurements in H-band as a function of HWP and derotator angle. The legend of Figure 4.3 also applies to this Figure.

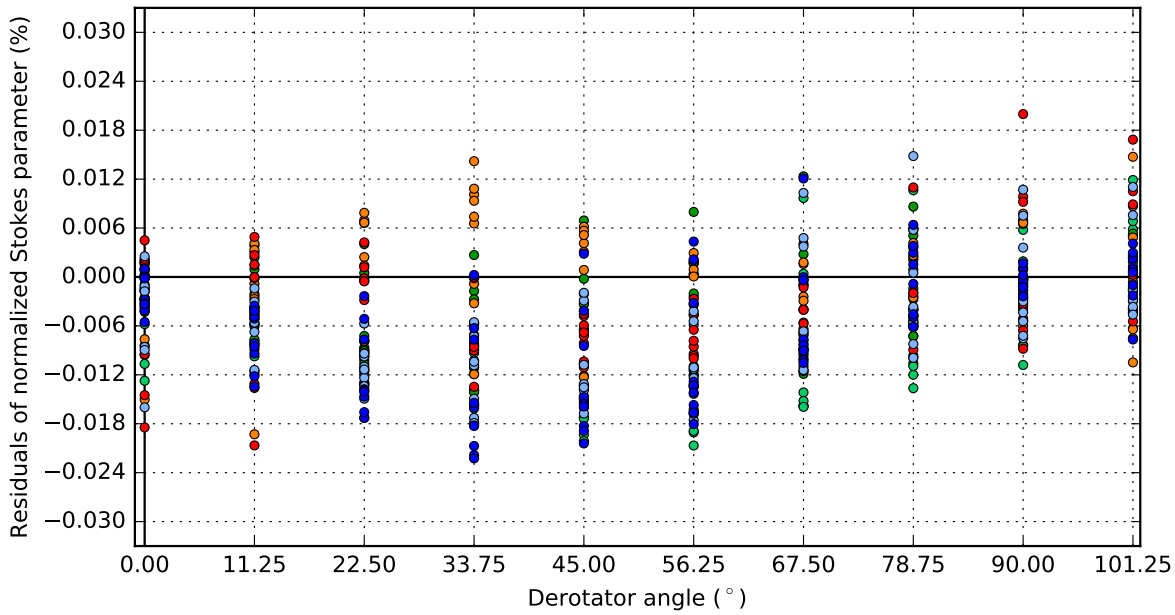

Figure 4.6: Residuals of the normalized Stokes parameters of the unpolarized source measurements in H-band as a function of HWP and derotator angle.

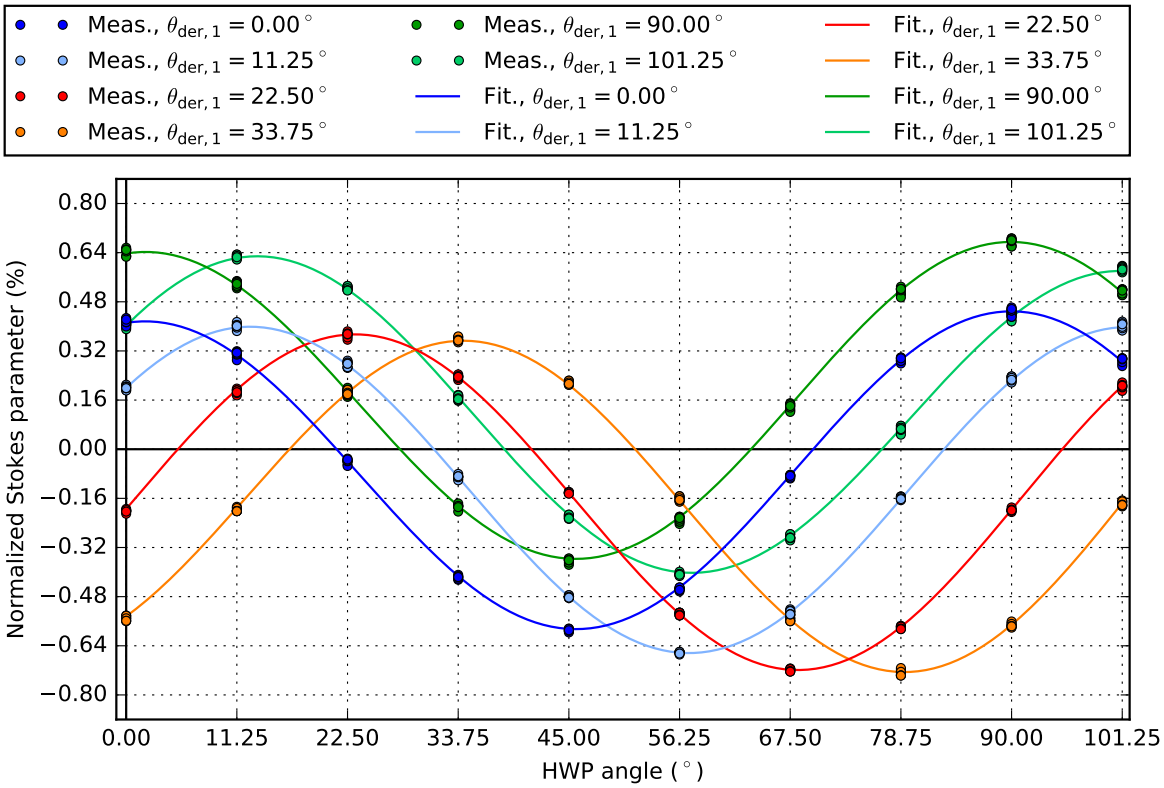

Figure 4.7: Measured and fitted normalized Stokes parameters of the unpolarized source measurements in H-band from beam switching with the derotator as a function of derotator and HWP angle.

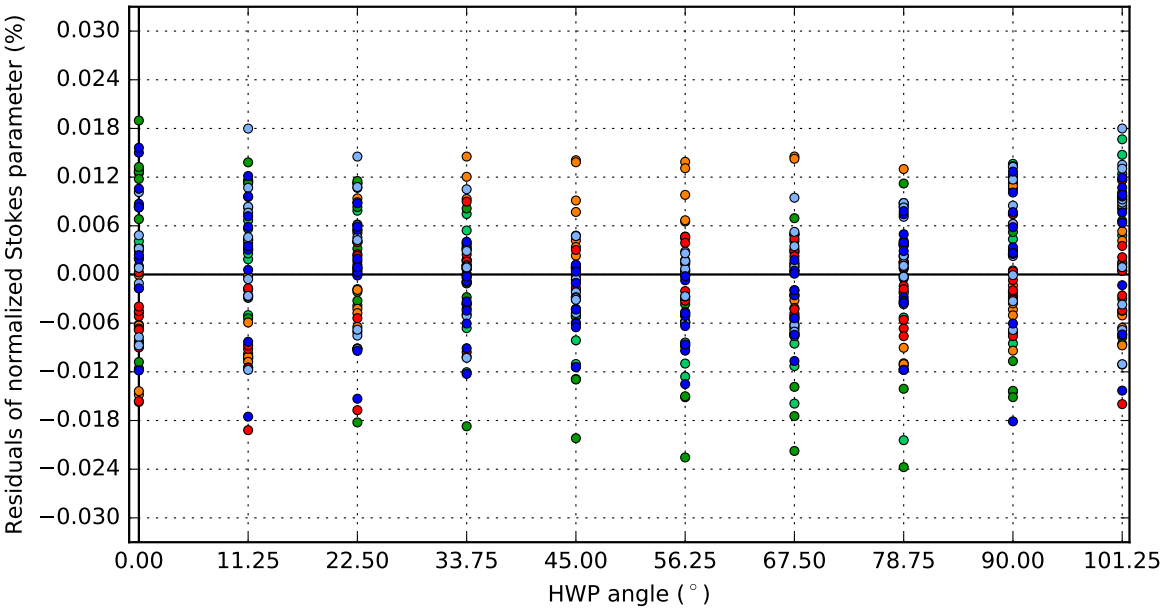

Figure 4.8: Residuals of the normalized Stokes parameters of the unpolarized source measurements in H-band from beam switching with the derotator as a function of derotator and HWP angle.

Table 4.1: Estimated parameters and their errors of the part of the model describing the instrument downstream of M4 in Y-, J-, H- and K_s-band.

Parameter	Value in BB_Y	Value in BB_J	Value in BB_H	Value in BB_K_s
$q_{\text{in,pol}}$ (%)	96.07 ± 0.08	97.91 ± 0.03	99.10 ± 0.05	96.88 ± 0.05
$q_{\text{in,unpol}}$ (%)	1.752 ± 0.001	1.2029 ± 0.0003	0.9444 ± 0.0005	0.8223 ± 0.0006
$u_{\text{in,unpol}}$ (%)	0.060 ± 0.002	0.0577 ± 0.0004	0.0396 ± 0.0007	0.0588 ± 0.0007
$v_{\text{in,unpol}}$ (%)	-0.010 ± 0.003	-0.003 ± 0.002	0.0070 ± 0.0008	-0.0045 ± 0.0008
ϵ_{HWP}	$1.00046 \pm 3 \cdot 10^{-5}$	$1.000851 \pm 9 \cdot 10^{-6}$	$1.00055 \pm 1 \cdot 10^{-5}$	$1.00082 \pm 2 \cdot 10^{-5}$
Δ_{HWP} (°)	184.2 ± 0.2	182.5 ± 0.2	170.5 ± 0.1	177.5 ± 0.1
δ_{HWP} (°)	$0.18589 \pm 5 \cdot 10^{-5}$	$0.18589 \pm 5 \cdot 10^{-5}$	$0.18589 \pm 5 \cdot 10^{-5}$	$0.18589 \pm 5 \cdot 10^{-5}$
ϵ_{der}	$1.00182 \pm 4 \cdot 10^{-5}$	$1.01658 \pm 1 \cdot 10^{-5}$	$1.00453 \pm 1 \cdot 10^{-5}$	$0.99302 \pm 1 \cdot 10^{-5}$
Δ_{der} (°)	126.1 ± 0.1	203.9 ± 0.1	99.39 ± 0.06	84.17 ± 0.05
δ_{der} (°)	$0.53088 \pm 5 \cdot 10^{-5}$	$0.53088 \pm 5 \cdot 10^{-5}$	$0.53088 \pm 5 \cdot 10^{-5}$	$0.53088 \pm 5 \cdot 10^{-5}$

From the model fit and the estimated parameters, the following conclusions are drawn:

- Since for all filters $q_{\text{in,pol}}$ is lower than 100%, the calibration polarizer and/or analyzer polarizers appear not to be perfect. Based on the value of $q_{\text{in,pol}}$ alone, the extinction ratios of the calibration and analyzer polarizers cannot be determined. For the correction of polarimetric science measurements (with only the analyzer polarizers inserted) using the response model, it is assumed that the calibration polarizer and analyzer have the same extinction ratio. The effect of the analyzer polarizers is then approximated by a polarimetric efficiency equal to $\sqrt{q_{\text{in,pol}}}$ (see Equation 5.6). To increase the model accuracy, the calibration and analyzer polarizers should also be included in the model and the results should be validated with the factory specifications of the polarizers.
- For the unpolarized source measurements, the light incident on the HWP is linearly polarized in the positive Q-direction and the degree of linear polarization decreases with increasing wavelength (from Y- to K_s-band). This polarization signal must be instrumental polarization caused by M4, that is in between the HWP and the light source. This is also in good agreement with the estimated diattenuation of M4 (see Table 5.2), and shows that the internal light source is almost completely unpolarized.
- The derotator retardance Δ_{der} deviates strongly from the ideal value of 180° in all filters and therefore is the main cause of the departure of the fitted curves from the ideal curves in Figure 4.3 and the sinusoids of the curves in Figures 4.5 and 4.7. The consequences of the derotator retardance will be further discussed below.
- The HWP retardance Δ_{HWP} is close to the ideal value of 180° in all filters (with the largest deviation in H-band) and therefore the HWP modifies the polarization signal much less than the derotator does. To validate the estimated values of Δ_{HWP} in the four filters, these values are compared to the HWP retardance specified by the manufacturer as a function of wavelength in Figure 4.9. In this Figure, the retardance is expressed as the path difference caused by the HWP, where $\Delta_{\text{HWP}} = 180°$ equals a path difference of a half wavelength. It follows that the estimated values of Δ_{HWP} are accurate, since they follow the general shape of the curve and are well within the specified 4% manufacturing tolerance in path difference (B. Halle Nachfl. GmbH, 2016).
- As the offset angles of the HWP and derotator, δ_{HWP} and δ_{der}, must be independent of wavelength, single values valid for all filters are estimated from the complete set of polarized source measurements.
- Since ϵ_{HWP} and ϵ_{HWP} are very close to the ideal value of 1 in all filters (with the largest deviation for the derotator in J-band), the instrumental polarization caused by the HWP and the derotator is very small (the derotator diattenuation is not fully removed when performing beam switching and calculating the double difference if the derotator rotates during an exposure, e.g. when observing in field-tracking mode). This is expected for the derotator, as its main surface coating is protected silver that is highly reflective. Considering that the derotator has its plane of incidence horizontal (parallel to the Nasmyth platform) when $\theta_{\text{der}} = 0°$, one would expect ϵ_{der} to be smaller than 1, while it is larger than 1 in three of the four filters. However, the estimated values of ϵ_{der} are consistent with those of Δ_{der} (see Figure 4.10): they show a similar curve as a function of central wavelength, and Δ_{der} passes from

values higher to values lower than 90° around the same central wavelength as ϵ_{der} changes from values higher to values lower than 1. Apparently the complex combination of coatings on the derotator causes the diattenuation to be different than expected.

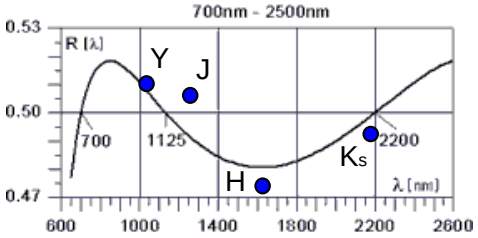

Figure 4.9: Path difference (as a fraction of wavelength) between the perpendicular linearly polarized components induced by the HWP as a function of wavelength as specified by the manufacturer (B. Halle Nachfl. GmbH, 2016) compared to the estimated retardance of the HWP (Δ_{HWP}; expressed as path difference) in Y-, J-, H- and K_s-band.

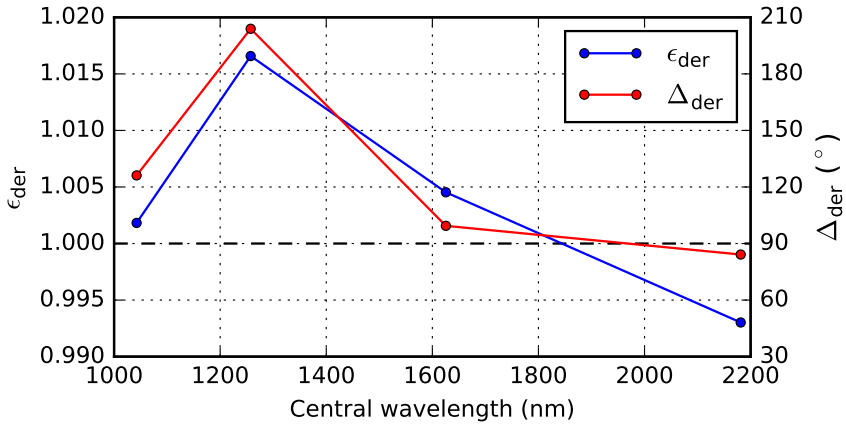

Figure 4.10: Estimated derotator diattenuation (ϵ_{der}) and retardance (Δ_{der}) as a function of the central wavelength of the Y-, J-, H- and K_s-band.

To better understand the implications of the estimated parameters, the polarimetric efficiency, i.e. the fraction of the linearly polarized light entering the system that is actually measured, of the instrument downstream of M4 is determined by computing the degree of linear polarization (see Equation 2.8) of the polarized source measurements. The degree of linear polarization is computed from two normalized Stokes parameters with $\theta_{HWP,1}$ differing 22.5° or 67.5°. The measured and fitted polarimetric efficiency in H-band as a function of HWP and derotator angle is shown in Figure 4.11[3].

In the ideal case, the polarimetric efficiency would be 100%. However, a dramatic decrease in polarimetric efficiency is seen around θ_{der} = 45°, reaching values as low as $\sim$ 5%. The low efficiency at these angles is caused by the derotator retardance that strongly deviates from the ideal value of 180°. Since Δ_{der} = 99.39°, the derotator acts almost as a quarter wave plate (Δ = 90°) so that around θ_{der} = 45° almost all incident linearly polarized light is converted into circularly polarized light, i.e. the derotator causes severe cross-talk. This circularly polarized light can not be measured by IRDIS and therefore the largest part of the incident linear polarization signal is lost. The effect of the retardance of the HWP is much smaller than that of the derotator, (Δ_{HWP} = 170.5°, relatively close to the ideal value of 180°) and is visible as the skewness and shifting of the fitted curves in Figure 4.11. The angle offsets δ_{HWP} and δ_{der} cause a small shift of the curves

[3]The derotator and HWP angles are calculated as the average of the derotator and HWP angles corresponding to the normalized Stokes parameters used to compute the degree of linear polarization.

and $q_{\text{in,pol}}$ (i.e. the efficiency of the polarizers) determines the maximum of the curves around $\theta_{\text{der}} = 0°$ and $\theta_{\text{der}} = 90°$.

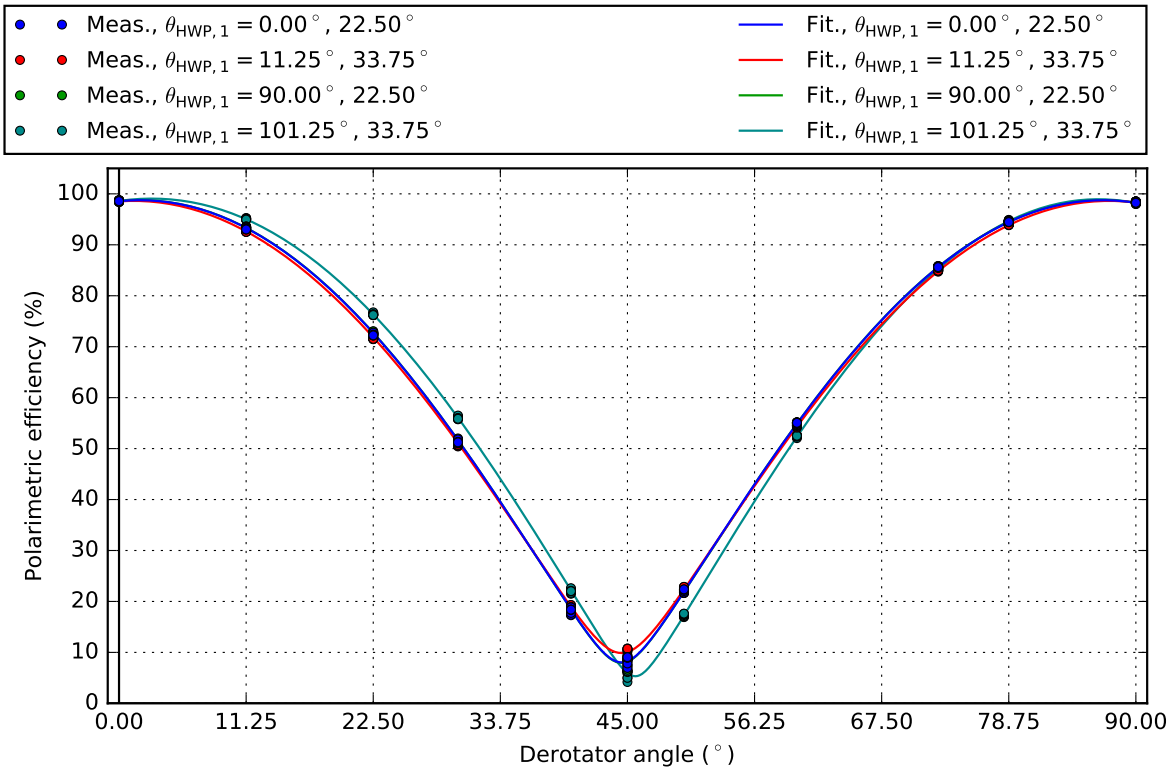

Figure 4.11: Measured and fitted polarimetric efficiency of the instrument downstream of M4 as a function of HWP and derotator angle in H-band. Note that the measurement points and fitted curves for $\theta_{\text{HWP,1}} = 0.00°, 22.50°$ (blue) and $\theta_{\text{HWP,1}} = 90.00°, 22.50°$ (green) are overlapping.

The retardance of the derotator (and HWP) not only affects the polarimetric efficiency, but also causes an offset of the angle of linear polarization. Figure 4.12 shows the ideal, measured and fitted angle of linear polarization (see Equation 2.9) and the offset of the angle of linear polarization induced by the instrument downstream of M4 corresponding to the curves of Figure 4.11. Ideally, the angle of linear polarization would rotate with two times the rotation rate of the derotator. However, due to in particular the derotator retardance, the polarization angle oscillates around the ideal angle, with the maximum deviation and the fastest rotation rate around $\theta_{\text{der}} = 45°$ and a maximum offset angle of $\sim 30°$.

Figures 4.13 and 4.14 show the polarimetric efficiency and angle of linear polarization offset in Y-, J-, H- and K_s-band for $\theta_{\text{HWP,1}} = 0°$ and 22.5° and for derotator angles from 0° to 180° (the curves repeat for $\theta_{\text{der}} > 180°$). In Figure 4.13, the strong decrease in efficiency is seen around $\theta_{\text{der}} = 45°$ and $\theta_{\text{der}} = 135°$, with minimum values in H-band of $\sim 8\%$ and $\sim 24\%$, respectively. Also K_s-band (efficiency $\gtrsim 8\%$) shows a strongly varying performance, while in Y-band ($\gtrsim 54\%$) and especially J-band ($\gtrsim 88\%$) the polarimetric efficiency is much better around $\theta_{\text{der}} = 45°$ and $\theta_{\text{der}} = 135°$.

Figure 4.14 shows that a low polarimetric efficiency is accompanied by a large offset in angle of linear polarization. While the oscillation around the ideal value is marginally visible in J-band, with a maximum deviation $\sim 3°$, the offset of the angle of linear polarization is $\lesssim 9°$ in Y-band and $\lesssim 30°$ in H-band. For K_s-band, the angle of linear polarization does not even return to the ideal value around $\theta_{\text{der}} = 45°$ and $\theta_{\text{der}} = 135°$, but continues rotating beyond $-90°$ (where a rotation of +90° is indistinguishable from $-90°$).

The curves in Figures 4.13 and 4.14 show asymmetry with respect to $\theta_{\text{der}} = 90°$ caused by the retardance of the HWP (strongest asymmetry in H-band). The exact shape of the curves depends on the HWP

angle (see Figures 4.11 and 4.12), and therefore the minimum polarimetric efficiency and maximum offset of angle of linear polarization stated above should be understood as approximate values only. The polarimetric efficiency during science observations, and an observation strategy to prevent observing at a low efficiency are discussed in Section 6.1.

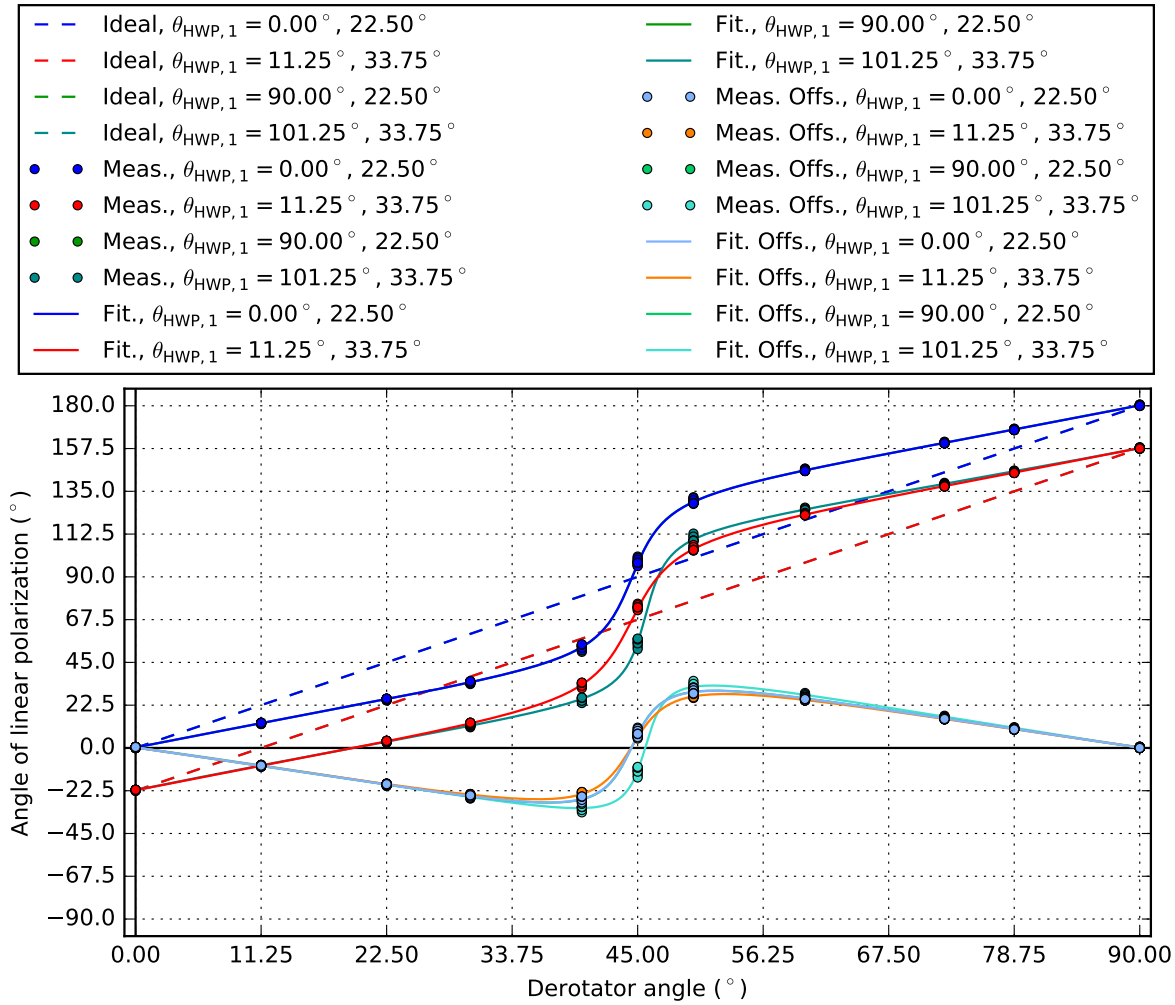

Figure 4.12: Ideal, measured and fitted angle of linear polarization and the offset of the angle of linear polarization induced by the instrument downstream of M4 as a function of HWP and derotator angle in H-band. Note that the measurement points and fitted curves for $\theta_{\mathrm{HWP},1} = 0.00^\circ, 22.50^\circ$ (blue and light blue) and $\theta_{\mathrm{HWP},1} = 90.00^\circ, 22.50^\circ$ (green and light green) are overlapping.

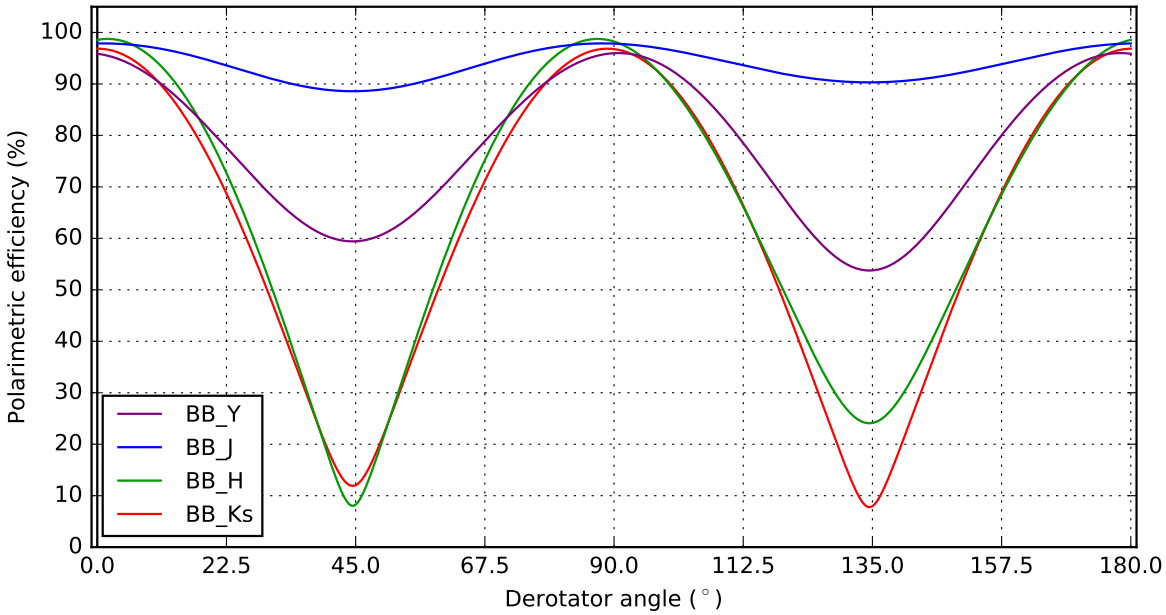

Figure 4.13: Fitted polarimetric efficiency of the instrument downstream of M4 with $\theta_{HWP,1}$ = 0°, 22.5° as a function of derotator angle in Y-, J-, H- and K_s-band.

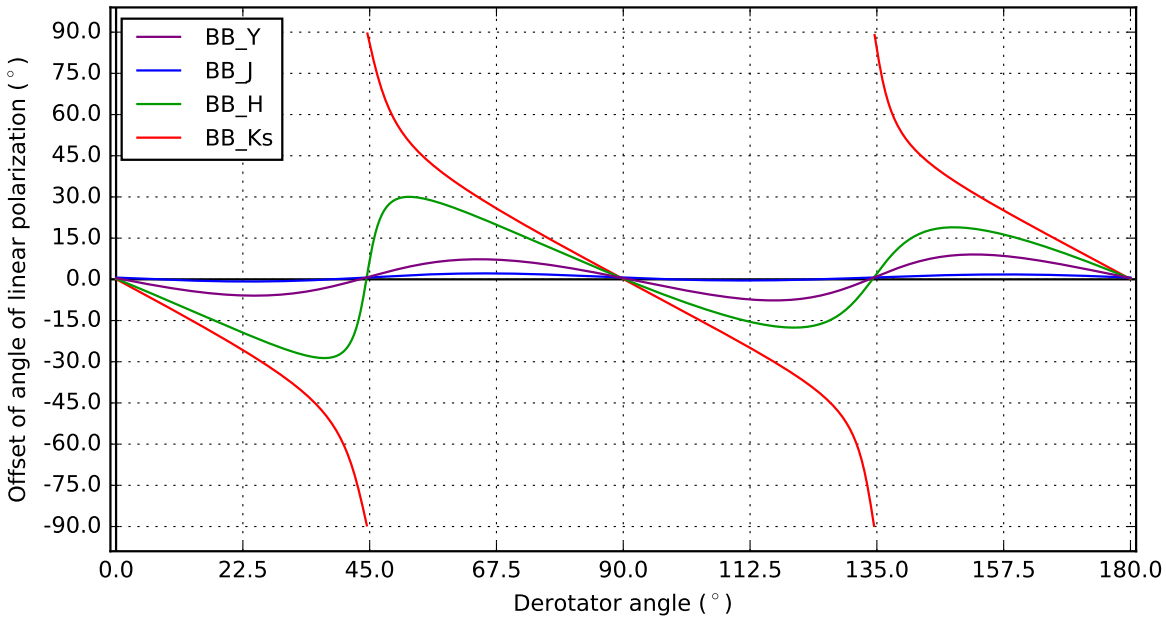

Figure 4.14: Fitted offset of angle of linear polarization induced by the instrument downstream of M4 with $\theta_{HWP,1}$ = 0°, 22.5° as a function of derotator angle in Y-, J-, H- and K_s-band.

4.4 Estimation of polarimetric accuracy and uncertainty in estimated parameters

To estimate the polarimetric accuracy of the part of the model downstream of M4, the accuracy of fit is calculated as the corrected sample standard deviation of the residuals s_{res}:

$$s_{\text{res}} = \sqrt{\frac{SSR}{n-k}} \tag{4.23}$$

with SSR the sum of squared residuals (see Equation 4.21), n the number data points and k the number of estimated parameters. The accuracy of fit is calculated separately for every combination of broadband filter and calibration polarizer setup by calculating SSR, n and k for the particular set of data points. Since δ_{HWP} and δ_{der} are estimated from all the polarized source measurements, their contribution to k is assigned a value of 0.25 (4 filters).

The accuracies of fit calculated this way show the random errors of the measurements, and not the systematic errors (.e.g. uncertainty of the HWP and derotator angles and of the orientation of the transmission axes of the analyzer polarizers). However, since the residuals of fit (see Figures 4.4, 4.6 and 4.8) are close to being normally distributed and many of the estimated parameters are consistent or validated with data from the manufacturer (HWP retardance), the systematic errors are likely small. Therefore, it is assumed that the polarimetric accuracy of the model can be accurately represented by the accuracies of fit.

The resulting accuracies of fit are shown in Table 4.2. From this Table, it follows that the accuracy of fit of the unpolarized source measurements is very high, well within the required absolute polarimetric accuracy of $< 0.1\%$ in all filters. For the polarized source measurements, the fit seems less accurate, but as the measurements were taken with almost 100% linearly polarized light incident on the HWP, the accuracy of fit is relative, i.e. it has to be scaled by the input polarization, so that for 1% linearly polarized incident light, the values are almost 100 times smaller. The accuracy of fit of the polarized source measurements is well below the required relative accuracy of $\sim 1\%$ in all filters. Finally, the values in Table 4.2 show that the total intensity dependent and polarization dependent gradients have a limited effect on the accuracy, which can also be seen from Figures 4.3, 4.5 and 4.7, because the 9 data points (from the 9 apertures covering almost the complete area of the frame) at every combination of θ_{der} and $\theta_{\text{HWP},1}$ are very close together. The total absolute polarimetric accuracy is discussed in Section 6.3.

Table 4.2: Accuracy of the fit of the part of the model describing the instrument downstream of M4 in Y-, J-, H- and K_s-band. Note that for the polarized source measurements the accuracy is relative.

Source	Filter	Accuracy of fit (%)
Unpolarized	BB_Y	0.023
	BB_J	0.0069
	BB_H	0.0083
	BB_K_s	0.0083
Polarized	BB_Y	0.74
	BB_J	0.41
	BB_H	0.59
	BB_K_s	0.55

The uncertainties of the parameters in Table 4.1 (after the $\pm$-sign) are 1σ-errors (1 times the standard deviation) computed from the square root of the diagonal elements of the covariance matrix of the estimated parameters $\Sigma_{\hat{\beta}\hat{\beta}}$:

$$\Sigma_{\hat{\beta}\hat{\beta}} = \tau (J^{\mathsf{T}} J)^{-1} \tau \tag{4.24}$$

where J is the Jacobian matrix:

$$J = \begin{bmatrix} \frac{\partial q_{\mathrm{DD},1}(\boldsymbol{x}_1, \boldsymbol{\beta})}{\partial \beta_1} & \cdots & \frac{\partial q_{\mathrm{DD},1}(\boldsymbol{x}_1, \boldsymbol{\beta})}{\partial \beta_m} \\ \vdots & \ddots & \vdots \\ \frac{\partial q_{\mathrm{DD},n}(\boldsymbol{x}_n, \boldsymbol{\beta})}{\partial \beta_1} & \cdots & \frac{\partial q_{\mathrm{DD},n}(\boldsymbol{x}_n, \boldsymbol{\beta})}{\partial \beta_m} \end{bmatrix} \tag{4.25}$$

with n the number of measurements and m the number of estimated model parameters. τ is an $m \times m$ matrix with on its diagonal the standard deviations corresponding to the model parameters. The standard deviation of each diagonal element is equal to the corrected sample standard deviation (s_{res}) of the fit from which that particular parameter is estimated. All these standard deviations are taken from Table 4.2, except for those of δ_{HWP} and δ_{der} that are calculated from the *SSR*, n and k of the complete set of polarized source measurements.

By taking the diagonal values of $\Sigma_{\hat{\beta}\hat{\beta}}$ as the uncertainties of the parameters, it is assumed that the parameter values are not correlated. However, in reality all the parameters are weakly correlated, in particular because δ_{HWP} and δ_{der} are estimated from the complete set of polarized source measurements. Moreover, because the uncertainties of the parameters are calculated from the corrected sample standard deviations of the residuals, they do not account for the (likely small) systematic errors. Finally, the uncertainties in Table 4.1 are computed using a linear approximation through the Jacobian, so they should be considered first order estimates. Under these assumptions, all model parameters describing optical components are accurate to at least four significant digits.

5 Polarimetric response and accuracy of the telescope and M4

To derive an exoplanet's true degree and angle of linear polarization, a model describing the polarimetric response of the complete optical system has been developed in Chapter 4. In the same Chapter, the model parameters of the optical path downstream of M4 are estimated from measurements using the internal light source. In this Chapter, the diattenuations of the telescope and M4 are estimated from observations of an unpolarized standard star. In Section 5.1 of this Chapter, the observations of the unpolarized standard star and the data reduction will be discussed. Subsequently, the diattenuations, their uncertainty and the polarimetric accuracy will be estimated using these measurements in Section 5.2.

5.1 Measurements and data reduction

To determine the polarimetric response of the Unit Telescope (UT) and M4, an unpolarized standard star has been observed at different telescope altitude angles. The normalized Stokes parameters calculated from these measurements can be modeled with the complete polarimetric response model (see Equations 4.6 to 4.12):

$$\boldsymbol{S}_{\text{meas}} = \begin{bmatrix} I_{\text{meas}} \\ Q_{\text{meas}} \\ U_{\text{meas}} \\ V_{\text{meas}} \end{bmatrix} = M_{\text{CI}}\, T(-\Theta_{\text{der}}) M_{\text{der}}\, T(\Theta_{\text{der}})\, T(-\Theta_{\text{HWP}}) M_{\text{HWP}}\, T(\Theta_{\text{HWP}}) M_{\text{M4}}\, T(a) M_{\text{UT}}\, T(p) \boldsymbol{S}_{\text{in}} \tag{5.1}$$

$$Q_{\text{DD}} = \frac{1}{2}\left[Q_{\text{meas}}(p_1, a_1, \theta_{\text{HWP},1}, \theta_{\text{der},1}) - Q_{\text{meas}}(p_2, a_2, \theta_{\text{HWP},2}, \theta_{\text{der},2})\right] \tag{5.2}$$

$$I_{\text{DS}} = \frac{1}{2}\left[I_{\text{meas}}(p_1, a_1, \theta_{\text{HWP},1}, \theta_{\text{der},1}) + I_{\text{meas}}(p_2, a_2, \theta_{\text{HWP},2}, \theta_{\text{der},2})\right] \tag{5.3}$$

$$q_{\text{DD}} = \frac{Q_{\text{DD}}}{I_{\text{DS}}} \tag{5.4}$$

On June 15, 2016, the unpolarized standard star HD176425 (Turnshek et al., 1990; 0.020$\pm$0.009% polarized in B-band) was observed in Y-, J-, H- and K_s-band to determine the diattenuations of the telescope and M4 (their retardances will be determined in the future, for example from observations of a polarized standard star). For the observations, the HWP and P0-90 analyzer set were inserted and the derotator was oriented with its plane of incidence horizontal (parallel to the Nasmyth platform; $\theta_{\text{der}} = 0^\circ$) during all observations to ensure a high polarimetric efficiency. SPHERE's adaptive optics system was turned off (open-loop) to obtain seeing limited images of the star and therefore reach a high photon count per detector integration time. For every filter, 10 HWP cycles (measurements with $\theta_{\text{HWP}} = 0^\circ; 45^\circ; 22.5^\circ$ and 67.5° to determine Stokes Q and U) were taken at very different altitude angles and parallactic angle combinations. This way, the diattenuation of the telescope, the diattenuation of M4 and the linear Stokes parameters Q and U of the star can be distinguished when fitting the data to the model. The number of detector integration times was

equal to 10 and the exposure time was 2 s to keep the HWP cycles short and therefore limit the variation of the parallactic and altitude angles during a HWP cycle.

The measurements are reduced by subtracting the master dark frame of the same exposure time and dividing by master flats of the correct broadband filter that both have been made for the measurements with the internal light source (the error introduced because of the neutral density filters used when taking the lamp flat frames is very limited). Sky background subtraction is not possible because the star's point spread function (PSF) covers almost the complete frame half. Subsequently, sigma-filtering is performed twice and an initial centering of the frames is performed using a Moffat function (Moffat, 1969). With a few iterations, the frames are centered with an accuracy of a third of a pixel. Then the *Q*-, *U*- and *I*-images are constructed (see Equations 5.2 and 5.3 and note that Stokes *U* in the celestial reference frame is measured as Stokes *Q* instrument's reference frame by rotating the HWP; after every subtraction or addition, the resulting images are centered again, with the difference images centered using the summed images). Finally, the normalized Stokes parameters *q* and *u* are determined by divided the sum of the values in an aperture in the *Q* and *U*-images by the sum of the values in the same aperture in the *I*-images (see Equation 5.4). The normalized Stokes parameters have also been computed as the median over the apertures of the normalized Stokes *q*- and *u*-images (*Q*-image or *U*-image divided by *I*-image), but this results in large errors because these images have a higher noise level.

The radius of the aperture used to calculate the normalized Stokes parameters is determined from plots of the normalized Stokes parameters as a function of aperture radius. In Y-, J- and H-band, an aperture radius of 200 pixels is used, because at this radius the curves have approached a nearly constant value (see Figure 5.1). In K_s-band, the curves do not approach a constant value, but decrease with increasing aperture radius due to a thermal background that most likely originates from the telescope (see Figure 5.2). Since the intensity of the star's PSF decreases with increasing distance from the center, the thermal background becomes more prominent for larger aperture radii. Although the thermal background is removed after computing the double difference (*Q*- and *U*-images), it is not removed after computing the double sum (*I*-images), and therefore the normalized Stokes parameters decrease with increasing aperture radius. An aperture radius of 125 pixels is selected for the measurements in K_s-band, because: 1) the curves of the other filters start to approach a constant value at this radius, 2) the thermal background starts to become visible in the raw frames at this radius, and 3) the estimated diattenuations of the UT and M4 are in line with expectations based on the estimated diattenuations in the other filters and their deviation from the analytical values (see Table 5.1).

5.2 Estimation of model parameters, polarimetric accuracy and uncertainty in parameters

To estimate the diattenuations of the telescope and M4 from the measurements, non-linear least squares is used (see Section 4.3 and Equations 4.17, 4.18, 4.21 and 4.22), with in this case the vector containing the independent variables of the *i*-th data point given by (see Figure 2.2):

$$\boldsymbol{x}_i = \left[F_i,\ C_i,\ p_{1,i},\ a_{1,i},\ \theta_{\mathrm{HWP},1,i},\ \theta_{\mathrm{der},1,i},\ p_{2,i},\ a_{2,i},\ \theta_{\mathrm{HWP},2,i},\ \theta_{\mathrm{der},2,i}\right] \tag{5.5}$$

where $p_{1,i}$ and $a_{1,i}$ are the parallactic and altitude angle of the first measurement used to construct the *Q*- and *U*-images, and $p_{1,i}$ and $a_{1,i}$ are the parallactic and altitude angle of the second measurement used to construct the *Q*- and *U*-images (see Equations 5.2 and 5.3)[1]. Note that the calibration polarizer is not inserted in any of the measurements. For the part of the model downstream of M4, the estimated parameters from Table 4.1 are used with M_{CI} in Equation 5.1 equal to:

$$M_{\mathrm{CI}} = \begin{bmatrix} 1 & 0 & 0 & 0 \\ 0 & d & 0 & 0 \\ 0 & 0 & 1 & 0 \\ 0 & 0 & 0 & 1 \end{bmatrix} \tag{5.6}$$

[1] The parallactic angle is computed as the average of the parallactic angles at the start and end of the measurement as specified in the headers of the .fits-files of the measurements. Since only the start value of the altitude angle is specified, the altitude angle is obtained by interpolation (and extrapolation at the end of sequence of measurements).

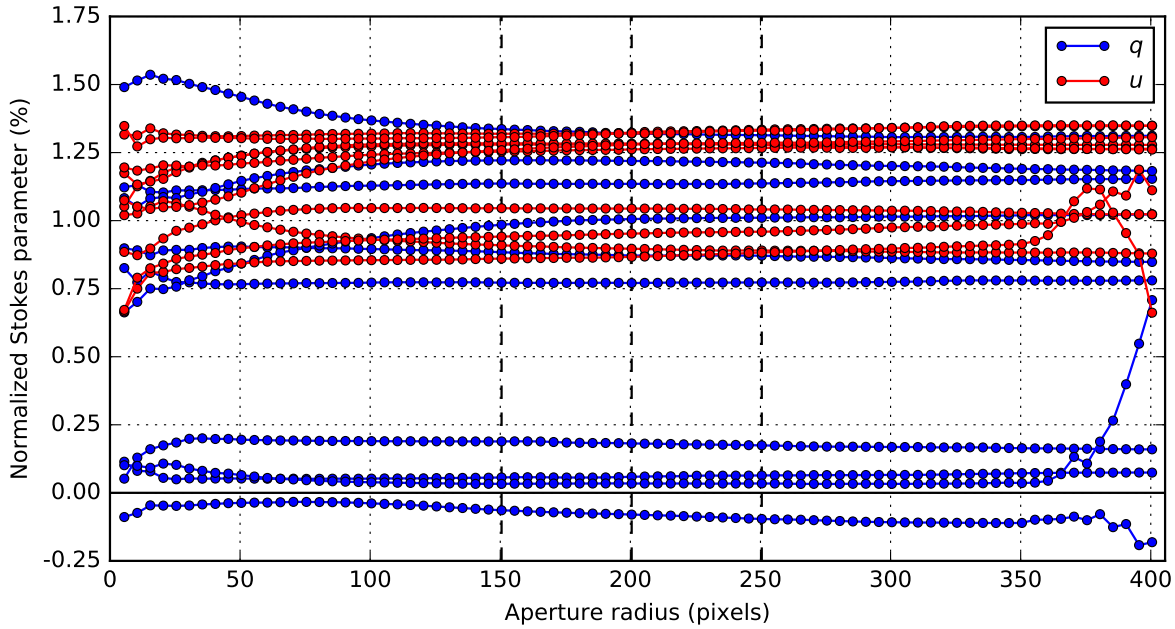

Figure 5.1: Normalized Stokes parameters *q* and *u* as a function of aperture radius in H-band. The central and outer dashed lines indicate the radii of the apertures from which the normalized Stokes parameters and their error bars in Figure 5.3 have been determined, respectively.

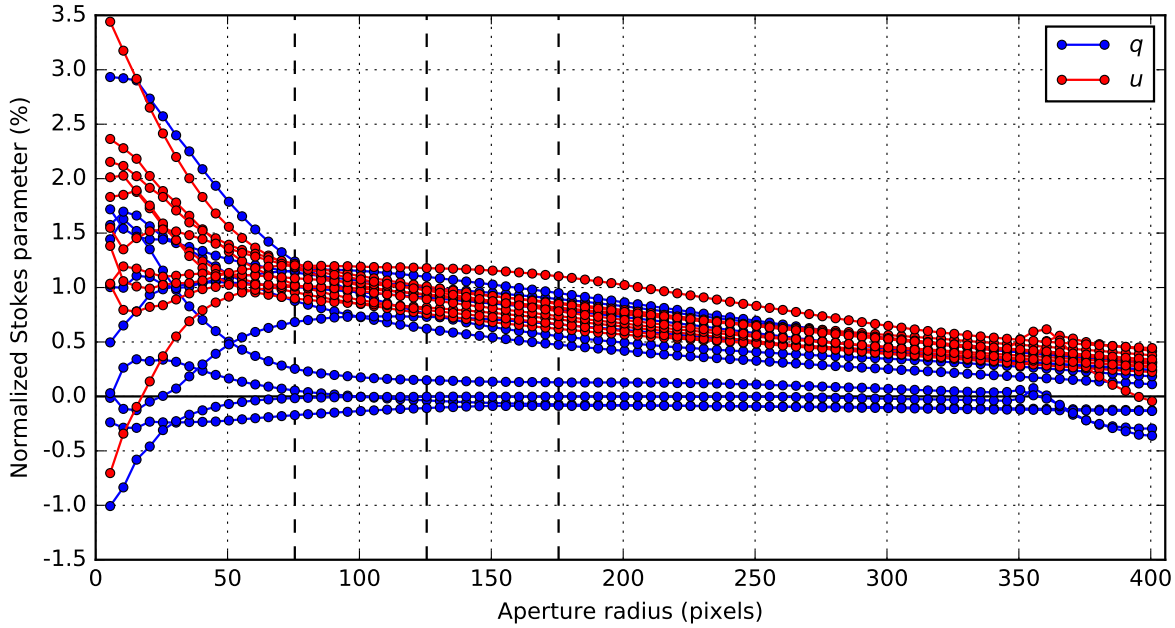

Figure 5.2: Normalized Stokes parameters *q* and *u* as a function of aperture radius in K_s-band. The central and outer dashed lines indicate the radii of the apertures from which the normalized Stokes parameters and their error bars in Figure 5.4 have been determined, respectively.

where $d = \sqrt{q_{\text{in,pol}}}$ is the polarimetric efficiency of the analyzer polarizers (see Section 4.3).

A similar program to that described in Section 4.3 has been written that performs the estimation of the model parameters. Since the retardances of the telescope and M4 cannot be accurately estimated from observations of an unpolarized standard star, they have been computed with the Fresnel equations using the complex refractive index of aluminum (the surface material of the telescope mirrors and M4) obtained from RefractiveIndex.INFO (2016). The retardance of the telescope is computed as the retardance of M3, because M1 and M2 are rotationally symmetric with respect to the optical axis of the telescope and therefore will not appreciably modify the polarization state of the light (Tinbergen, 2005).

The resulting model parameter values are shown in Table 5.1. In this Table, ϵ_{UT} and ϵ_{M4} are the diattenuations of the UT and M4, respectively, and Δ_{UT} and Δ_{M4} are their retardances. Figures 5.3 and 5.4 show the analytical, measured and fitted normalized Stokes parameters q and u as a function of telescope altitude angle in H- and K_s-band, respectively. The residuals of fit in Y-, J-, H- and K_s-band are shown in Figure 5.5. Note that the telescope altitude angle is restricted to angles larger than 20°. The analytical curves of Figures 5.3 and 5.4 have been computed with the Fresnel equations using the complex refractive index of aluminum and by modeling the telescope with the Mueller matrix of M3. The error bars are calculated (rather arbitrarily) as half the difference between the normalized Stokes parameters determined from apertures with radii 50 pixels larger and smaller than the radius of the aperture used to calculate q and u used for estimating the diattenuations (see Figures 5.1 and 5.2). They show the systematic error in the normalized Stokes parameters, which is small in Y-, J- and H-band, but large in K_s-band due to the thermal background (see Section 5.1).

Figure 5.6 shows the analytical, measured and fitted plots of the degree of linear polarization (see Equation 2.8) as a function of telescope altitude angle in Y-, J-, H- and K_s-band. The degree of linear polarization is computed from the normalized Stokes parameters and represents the instrumental polarization (IP) of the telescope and M4[2]. The angle of linear polarization (see Equation 2.9) induced by the instrumental polarization of the telescope and M4 when the incident light is completely unpolarized is shown in Figure 5.7.

Table 5.1: Estimated diattenuations and their errors and computed retardances of the part of the model describing the telescope and M4 in Y-, J-, H- and K_s-band.

Parameter	Value in BB_Y	Value in BB_J	Value in BB_H	Value in BB_K_s
ϵ_{UT}	0.9526 ± 0.0004	0.9662 ± 0.0003	0.9738 ± 0.0002	0.9785 ± 0.0006
ϵ_{M4}	0.9666 ± 0.0004	0.9761 ± 0.0003	0.9813 ± 0.0002	0.9851 ± 0.0006
Δ_{UT} (°)	188.1	186.6	185.0	183.7
Δ_{M4} (°)	188.1	186.6	185.0	183.7

From the model fit and the estimated parameters, the following conclusions are drawn:

- The error on the estimated value of ϵ_{UT} due to using a computed, rather than a measured value of Δ_{M4} is expected to be small, because the real value of Δ_{M4} is likely close to the computed value and its effect on the instrumental polarization of the UT is relatively small (computed value of Δ_{M4} is relatively close to the ideal value of 180°). The estimated value of ϵ_{M4} is not affected by the value of Δ_{M4}.
- When also estimating the Stokes vector incident on the telescope, the resulting degree of linear polarization of the star is very low in all filters (generally much less than 0.1%), confirming that the standard star observed is unpolarized. To avoid fitting noise, only the diattenuations of the UT and M4 are fitted and not the incident Stokes vector.
- For completely unpolarized incident light, the instrumental polarization of M4 in Stokes q follows from $q_{\text{IP,M4}} = (1 - \epsilon_{\text{M4}})/(1 + \epsilon_{\text{M4}})$. Since M4 is in between the internal light source and the HWP, its IP should correspond to the estimated $q_{\text{in,unpol}}$ from Table 4.1. The values of $q_{\text{IP,M4}}$ and $q_{\text{in,unpol}}$ are compared in Table 5.2, from which follows that the observations of the unpolarized standard star are in good agreement with the measurements with the internal light source, particularly in J- and H-band.

[2]The altitude angles are calculated as the average of the altitude angles corresponding to the normalized Stokes parameters q and u used to compute the degree of linear polarization.

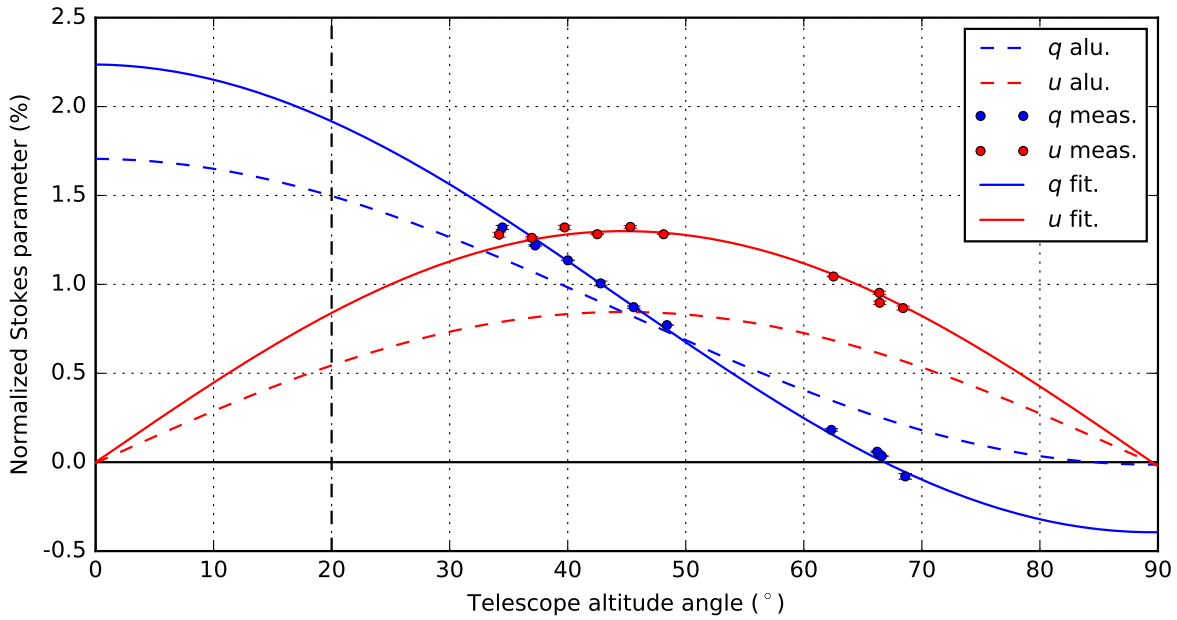

Figure 5.3: Analytical (aluminum), measured (including error bars) and fitted normalized Stokes parameters *q* and *u* as a function of telescope altitude angle in H-band. Note that the altitude angle is restricted to angles larger than 20°.

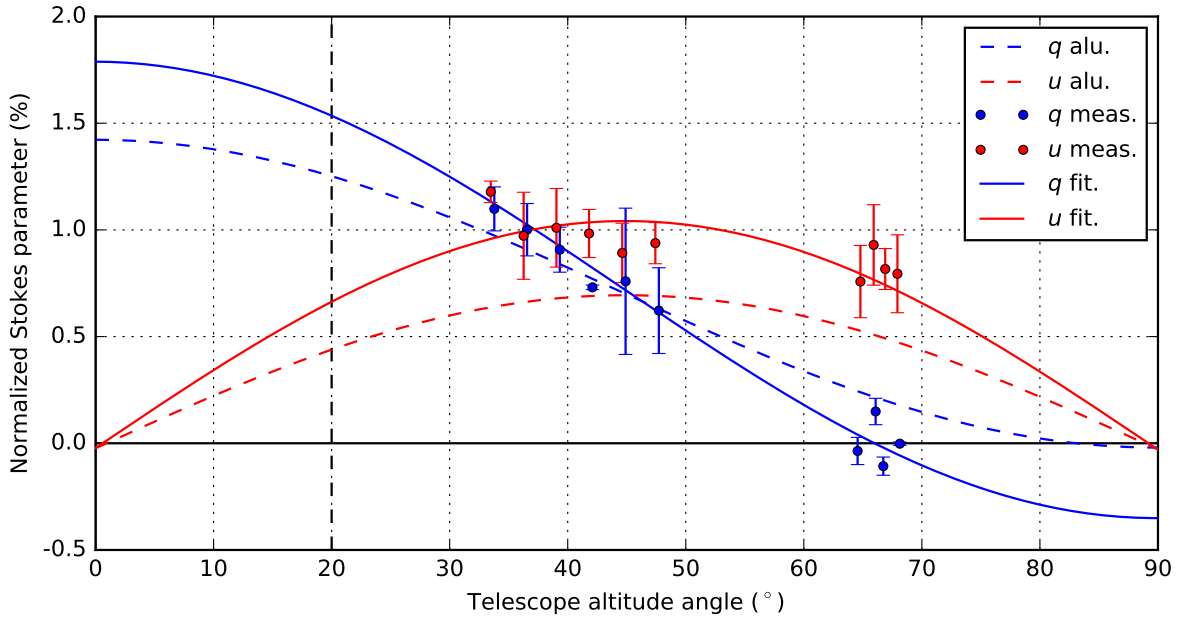

Figure 5.4: Analytical (aluminum), measured (including error bars) and fitted normalized Stokes parameters *q* and *u* as a function of telescope altitude angle in K_s-band. Note that the telescope's altitude angle is restricted to angles larger than 20°.

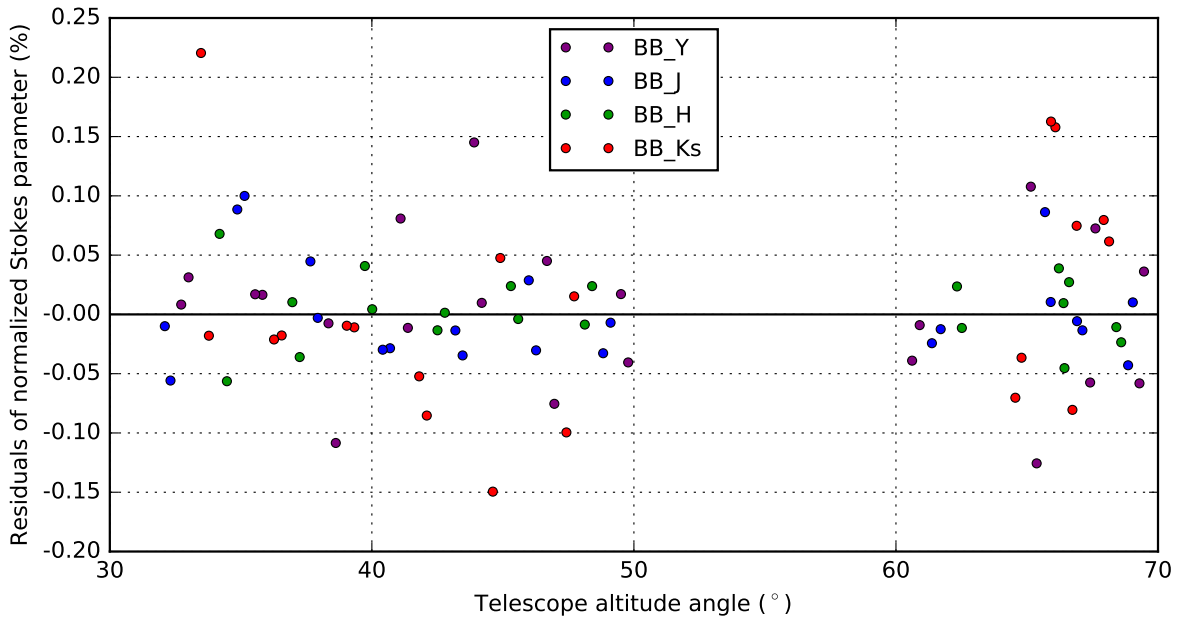

Figure 5.5: Residuals of the normalized Stokes parameters *q* and *u* as a function of telescope altitude angle in Y-, J-, H- and K_s-band.

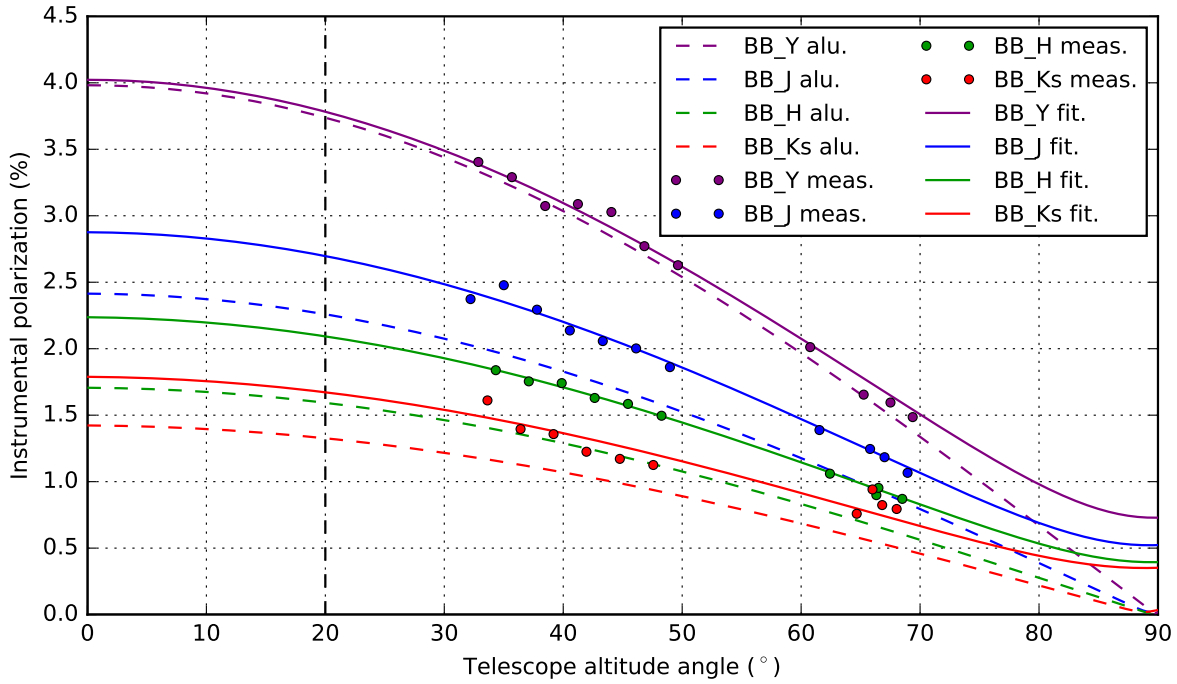

Figure 5.6: Analytical (aluminum), measured and fitted instrumental polarization of the telescope and M4 as a function of telescope altitude angle in Y-, J-, H- and K_s-band. Note that the telescope's altitude angle is restricted to angles larger than 20°.

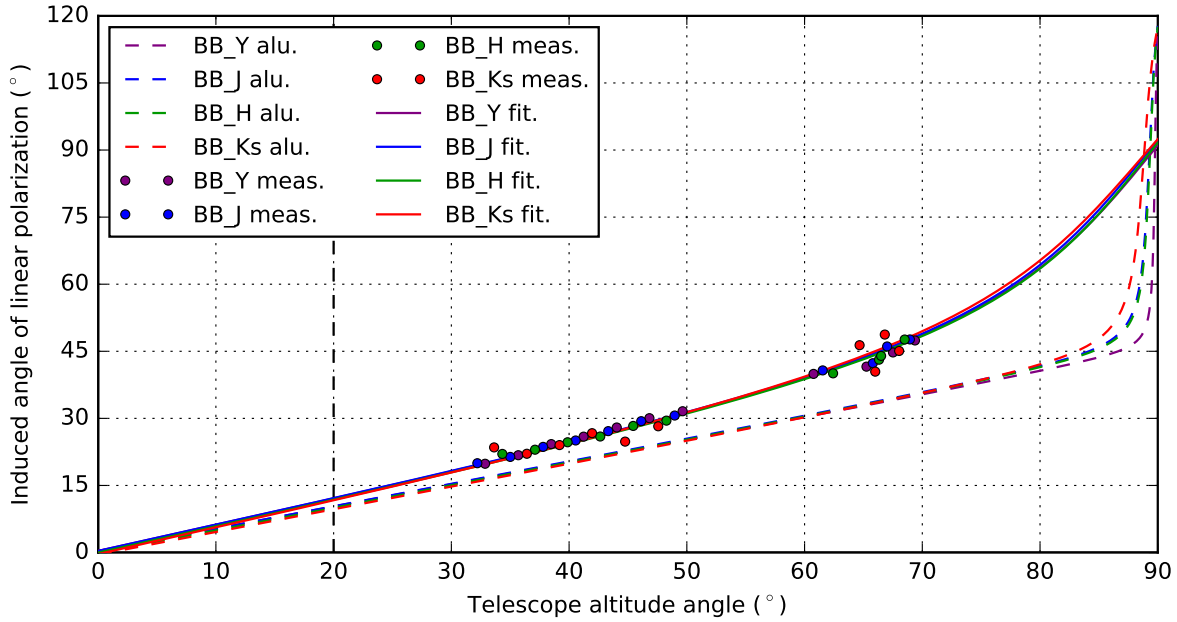

Figure 5.7: Analytical (aluminum), measured and fitted angle of linear polarization induced by the telescope and M4 (unpolarized incident light) as a function of telescope altitude angle in Y-, J-, H- and K_s-band. Note that the telescope's altitude angle is restricted to angles larger than 20°.

The difference between the values could be due to the internal light source possibly not being fully unpolarized or instrumental polarization of other components in the calibration unit.

- From Figure 5.6, it follows that the IP increases with decreasing altitude angle with the maximum IP (at an altitude angle of 20°) equal to 3.8%, 2.7%, 2.1% and 1.7% in Y-, J-, H- and K_s-band, respectively. The corresponding minimum values (at an altitude angle of 90°) are 0.73%, 0.51%, 0.38% and 0.34%, respectively. As the HWP is downstream from M4, this IP cannot be removed by performing beam switching with the HWP and computing the double difference. The IP can only be limited by timing an observing run such that the target is at a high altitude angle.
- If science observations are not corrected for the IP of the telescope and M4 with the polarimetric response model, not only the measured degree of linear polarization is inaccurate, but also the angle of linear polarization (see Figure 5.7).
- The estimated values of ϵ_{UT} (which is basically the diattenuation of M3 because M1 and M2 are rotationally symmetric) are consistent with those of ϵ_{M4} as both show a similar curve as a function of central wavelength (see Figure 5.8). In the ideal case, ϵ_{UT} and ϵ_{M4} would be equal, and the instrumental polarization of M4 is completely canceled by that of M3 at an altitude angle of 90° (M3 and M4 in crossed configuration). However, as ϵ_{UT} and ϵ_{M4} are not equal, probably due to differences in the aluminum oxide layers of the mirrors (see van Harten et al., 2009) or due to the presence of dust (both can change in time), the instrumental polarization is not totally canceled at an altitude angle of 90° (see Figure 5.6). During observations with ZIMPOL, an additional HWP in between M3 and M4 is used to rotate the IP of M3 such that it is ideally completely canceled by M4 at any altitude angle. Roelfsema et al. (2010) claim to reach a polarimetric accuracy of 0.1% with ZIMPOL using this technique. However, as the diattenuations of M3 and M4 are not equal at near-infrared wavelengths, and since this is probably caused by different aluminum oxide layers or dust, the diattenuations are likely not equal at visible wavelengths either. Therefore, it is unlikely that the accuracy claimed by Roelfsema et al. (2010) is actually reached.

Table 5.2: Calculated instrumental polarization of M4 in Stokes q, $q_{IP,M4}$, compared to the estimated $q_{in,pol}$ from Table 4.1 in Y-, J-, H- and K_s-band.

Filter	$q_{IP,M4}$ (%)	$q_{in,unpol}$ (%)
BB_Y	1.698	1.752
BB_J	1.209	1.2029
BB_H	0.9438	0.9444
BB_K_s	0.7506	0.8223

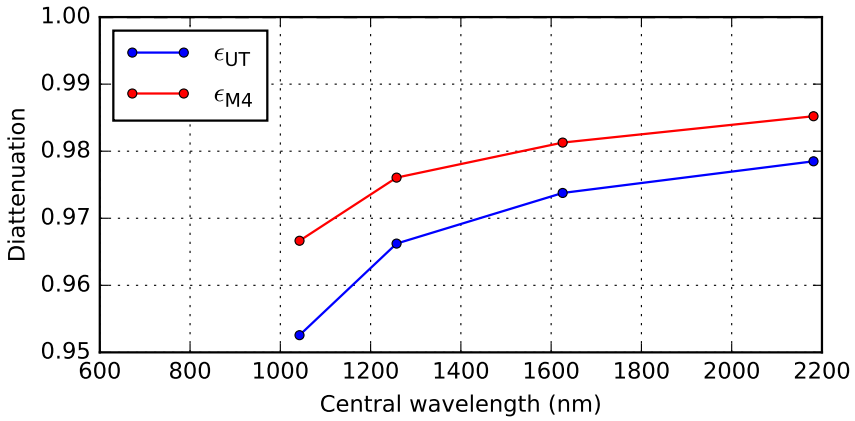

Figure 5.8: Estimated diattenuation of the UT (ϵ_{UT}) and M4 (ϵ_{M4}) as a function of the central wavelength of the Y-, J-, H- and K_s-band.

To estimate the polarimetric accuracy of the part of the model describing the telescope and M4, the accuracy of fit for each filter is calculated as the corrected sample standard deviation of the residuals (see Equation 4.23). The results are shown in Table 5.3. From this Table, it follows that the accuracy of the part of the model describing the telescope and M4 is well within the required absolute polarimetric accuracy of $< 0.1\%$ in Y-, J- and H-band, and $\sim 0.1\%$ in K_s-band (assuming systematic errors are small and that the polarimetric accuracy of the model can be accurately represented by the accuracies of fit). The total absolute polarimetric accuracy is discussed in Section 6.3.

The uncertainties of the parameters in Table 5.1 (after the $\pm$-sign) are 1σ-errors computed from the square root of the diagonal elements of the covariance matrix of the estimated parameters (see Equation 4.24). The standard deviations of the matrix τ are taken from Table 5.3. Although the values of ϵ_{UT} and ϵ_{M4} for the different filters are completely uncorrelated, the uncertainties in Table 5.1 should still be considered first order estimates because systematic errors are not accounted for and a linear approximation through the Jacobian is used. Under these assumptions, the diattenuations of the telescope and M4 are accurate to at least four significant digits.

Table 5.3: Accuracy of the fit of the part of the model describing the telescope and M4 in Y-, J-, H- and K_s-band.

Filter	Accuracy of fit (%)
BB_Y	0.068
BB_J	0.044
BB_H	0.032
BB_K_s	0.098

6 Application of the polarimetric calibration to science observations

The polarimetric response model describing the complete optical system has been validated using measurements with the internal light source and observations of an unpolarized standard star. In this Chapter, the model will be applied to science observations and the accuracy of such measurements will be estimated. In Section 6.1, the model will be used to calculate the polarimetric efficiency and instrumental polarization (IP) during observations in field-tracking and pupil-tracking mode, and an observation strategy to maximize the efficiency and minimize the IP will be presented. Subsequently, in Section 6.2, the model will be used to accurately determine the linearly polarized intensity and angle of linear polarization over the circumstellar disk of TW Hya to exemplify the correction of the complete system's polarimetric response. Finally, the polarimetric accuracy of science measurements after correcting for the polarimetric response of the complete optical system, i.e. the uncertainty in the measured polarization signal, will be estimated in Section 6.3.

6.1 IP and polarimetric efficiency during science observations

Science observations with IRDIS polarimetry can currently only be performed in field-tracking mode, in which the field of view remains fixed with north up on the detector. To achieve this, the derotator rotates according to the control law:

$$\theta_{\text{der}} = \frac{1}{2}\left(-p + a + \eta\right) \tag{6.1}$$

with θ_{der} the derotator angle, p the astronomical target's parallactic angle, a the altitude angle of the telescope and η a position angle offset of the image due to a user-defined derotator offset. To also keep Stokes Q with north up on the detector, the HWP rotates according to the control law:

$$\theta_{\text{HWP}} = -p + a + \frac{1}{2}\left(\eta + \gamma\right) \tag{6.2}$$

with θ_{HWP} the HWP angle and γ an offset of the angle of linear polarization due to a user-defined HWP offset. Beam switching with the HWP (to determine Stokes Q and U from the double difference) is performed relative to this HWP angle.

Using these control laws and the estimated parameters in Table 4.1, the polarimetric efficiency of SPHERE/IRDIS downstream of M4 during field-tracking in H-band is computed as a function of parallactic and altitude angle. The result is shown in Figure 6.1. From this Figure, it follows that for particular combinations of the parallactic and altitude angle, the derotator (and HWP) angle is such that the polarimetric efficiency is very low (see Figure 4.11), with a minimum efficiency of 8.1%. Around the same angles, also the offset of the angle of linear polarization is large (plot not shown; see Figure 4.12). The shape of the polarimetric efficiency plots are similar for the other filters, but the minimum values are different (see Figure 4.13). In K_s-band, the efficiency also reaches very low values (minimum of 7.9%), while in Y-band (efficiency $>$ 54.8%) and especially J-band ($>$ 89.5%) the polarimetric efficiency is much better.

Although the polarimetric efficiency can be corrected for with the polarimetric response model, the loss

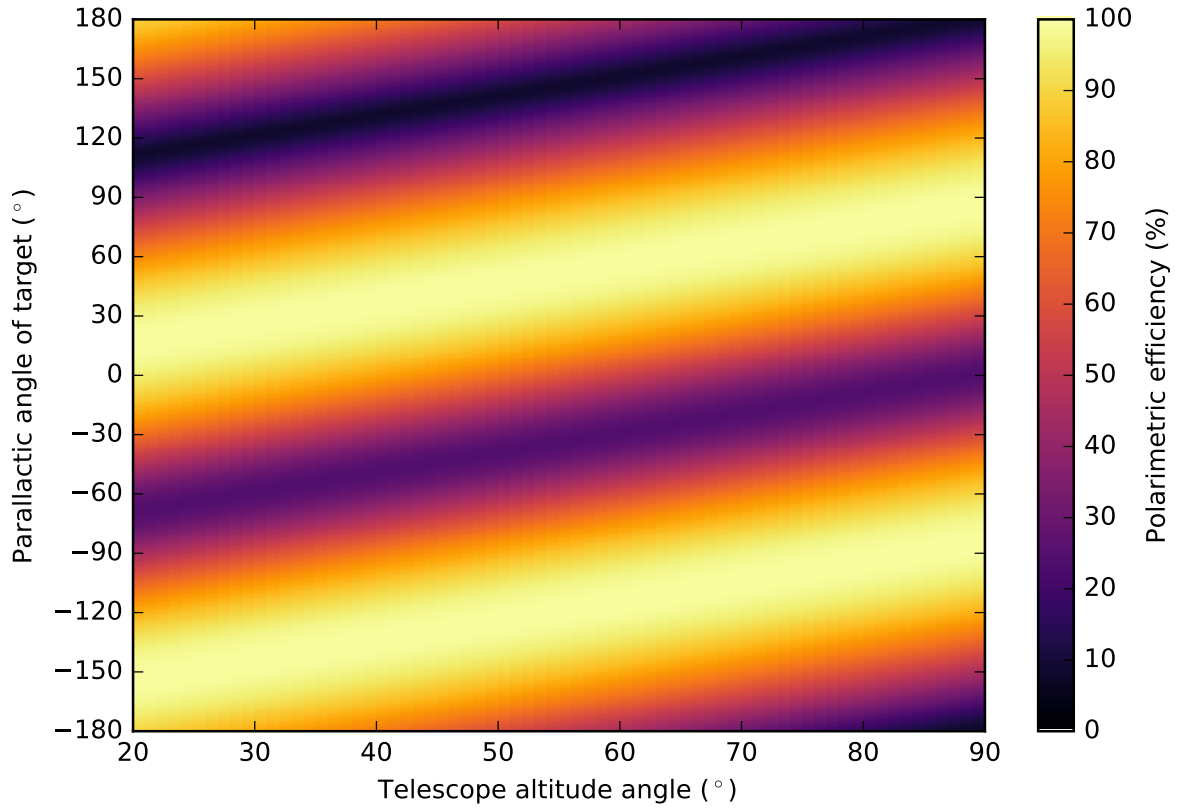

Figure 6.1: Polarimetric efficiency of the instrument downstream of M4 in H-band as a function of parallactic angle of the target and telescope altitude angle in field-tracking mode.

of signal (and the offset in angle of linear polarization) should be limited during observations in field-tracking mode with the following observation strategy:

- When no strict wavelength requirements are present, observe in J-band.
- If Y-, H- or K_s-band has to be used, adjust the time of observation such that the measurements can be taken at combinations of parallactic and altitude angle that result in a high polarimetric efficiency (see Figure 6.1).
- If (part of) the observations have to be performed at an unfavorable combination of parallactic and altitude angle, offset the derotator by applying an η-offset (position angle offset of the image) equal to[1]:

$$\eta = \overline{p} - \overline{a} + n \cdot 180^\circ \tag{6.3}$$

  with $\overline{p}$ and $\overline{a}$ the average parallactic and altitude angle of the observations, respectively, and n an integer. Because of the offset, the image is not with north up on the detector anymore, and so the image needs to be software derotated in the data reduction. Figure 6.2 shows the polarimetric efficiency of the instrument downstream of M4 during field-tracking in H-band after applying an offset $\eta = 90^\circ$ that changes the parallactic and altitude angle combinations with a low efficiency into ones with a high efficiency and vice versa.
- For observations with a large variation in parallactic and altitude angle (e.g. long observing runs or observations including the meridian crossing), split the observations in multiple parts with a different η-offset each.

[1] The keyword for η in the observation templates is INS.CPRT.POSANG.

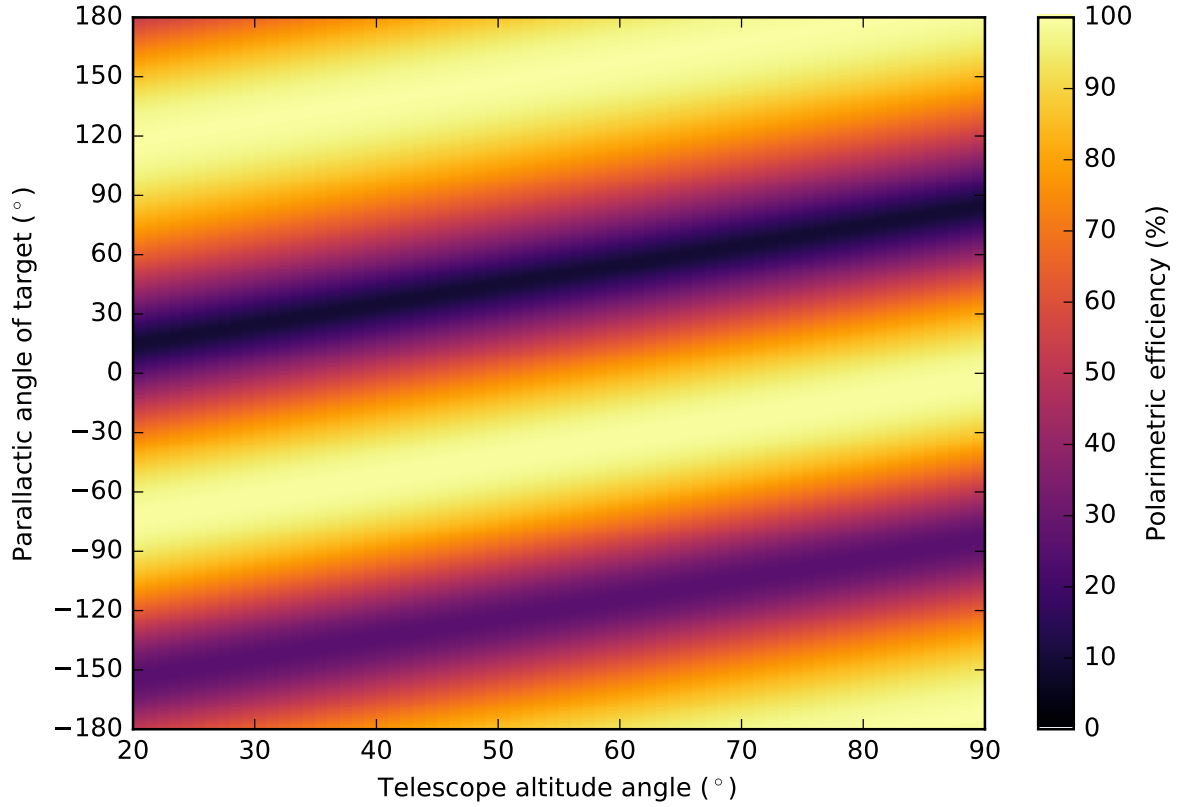

Figure 6.2: Polarimetric efficiency of the instrument downstream of M4 in H-band as a function of parallactic angle of the target and telescope altitude angle in field-tracking mode with the derotator and HWP angles offset by 45° (η = 90°).

In addition to offsetting the derotator, the HWP can be offset by applying a γ-offset (offset of the angle of linear polarization) to improve the polarimetric efficiency a few percent more, especially in H-band where the HWP retardance is furthest from the ideal value[2].

In pupil-tracking mode, in which the derotator only compensates for the altitude angle so that the image rotates with the parallactic angle over the detector, the derotator rotates according to the control law:

$$\theta_{\text{der}} = \frac{1}{2}\left(a + \eta + \eta_{\text{pupil}}\right) \tag{6.4}$$

where η_{pupil} is the fixed position angle offset of the image to align the spider mask with the diffraction pattern of the M2 support structure (the 'spider'; $\eta_{\text{pupil}} \approx 135°$). Currently, pupil-tracking has not yet been commissioned for IRDIS' polarimetric mode. For this, the following HWP control law should be implemented that keeps Stokes Q with north up on the detector[3]:

$$\theta_{\text{HWP}} = a + \frac{1}{2}\left(-p + \eta + \gamma + \eta_{\text{pupil}}\right) \tag{6.5}$$

The polarimetric efficiency of the instrument downstream of M4 during pupil-tracking in H-band as a function of parallactic and altitude angle is shown in Figure 6.3. From this Figure, it follows that for altitude

[2]The use of a γ-offset is left for future work.

[3]Polarimetric observations in pupil-tracking mode are possible without this HWP control law, .e.g. by performing beam switching with the HWP relative to the vertical (perpendicular with respect to the Nasmyth platform). However, the angle of linear polarization will then rotate over the detector and the data can only be reduced using the polarimetric response model (see Section 6.2).

angles between 20° and 75°, the efficiency in H-band is always higher than 80.3%. For altitude angles higher than 75°, the efficiency can go down to 63.8% and an η-offset, similar to that used for field-tracking, could be applied. The polarimetric efficiency plots look similar for the other filters. Also in Y- and K_s-band an η-offset can be applied, since the efficiency at altitude angles higher than 75° goes down to 76.6% and 66.3%, respectively, while in J-band (efficiency $>$ 93.6%) no η-offset is required.

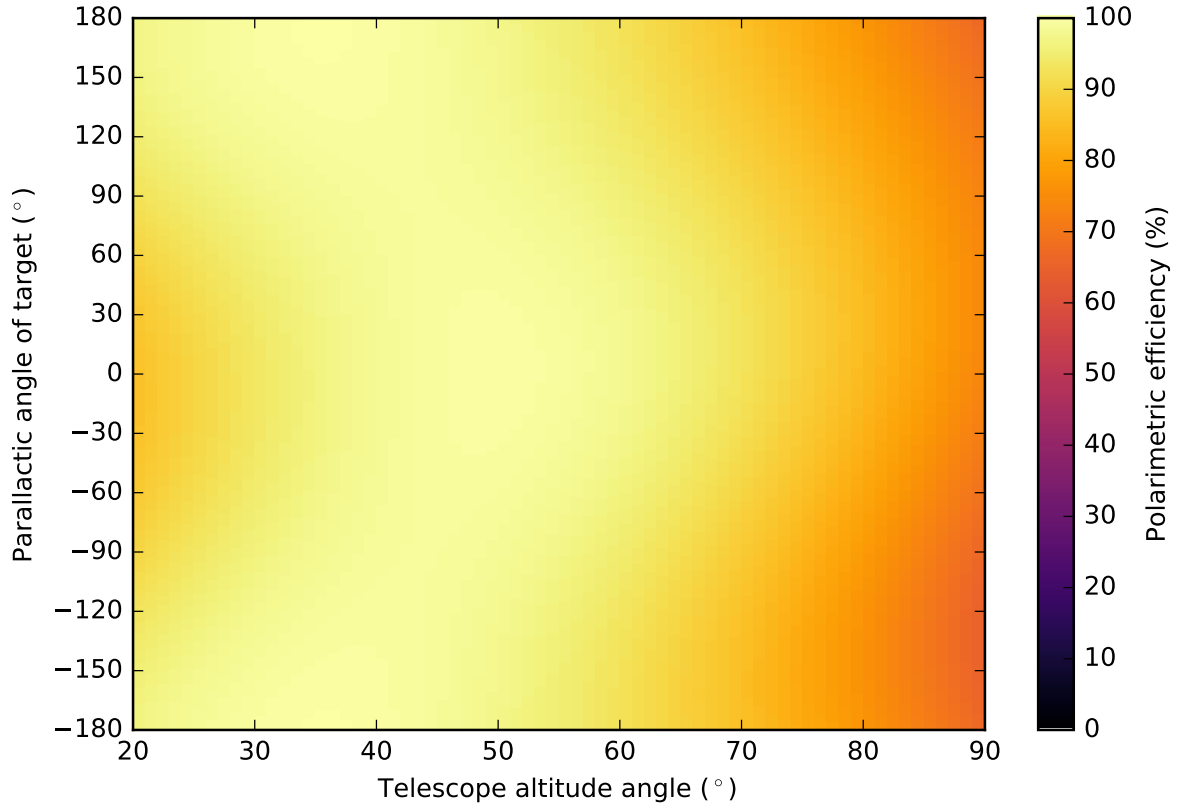

Figure 6.3: Polarimetric efficiency of the instrument downstream of M4 in H-band as a function of parallactic angle of the target and telescope altitude angle in pupil-tracking mode.

The instrumental polarization (IP; expressed as degree of linear polarization) of the telescope and M4 in H-band as a function of parallactic and altitude angle is shown in Figure 6.4. The IP only depends on the altitude angle; it is independent of the parallactic angle or the derotator and HWP control laws used (field-tracking or pupil-tracking). The IP is maximum at an altitude angle of 20° and equals 3.9%, 2.8%, 2.1% and 1.7% in Y-, J-, H- and K_s-band, respectively. The corresponding minimum values (at an altitude angle of 90°) are 0.73%, 0.51%, 0.38% and 0.34%, respectively. The IP can be limited by observing at longer wavelengths (e.g. K_s-band) and by adjusting the time of observation such that the observations are performed at a high altitude angle (both are also favorable for the atmospheric seeing, but an η-offset might be needed to keep the polarimetric efficiency high when observing at high altitude angles). For the observation strategy, the IP is less important than the polarimetric efficiency, as large IP does not necessarily imply a loss of signal and the IP can be corrected for with the polarimetric response model.

6.2 Correcting science observations

To derive an exoplanet's true degree and angle of linear polarization, the measurements need to be corrected for the polarimetric response of the complete optical system. For this, Stokes *I*-, *Q*- and *U*-images are prepared in the usual way (dark-subtraction, flat-fielding, sigma-filtering, centering and determining Stokes *I* from the double sum and Stokes *Q* and *U* from the double difference), but no corrections for the instrumental

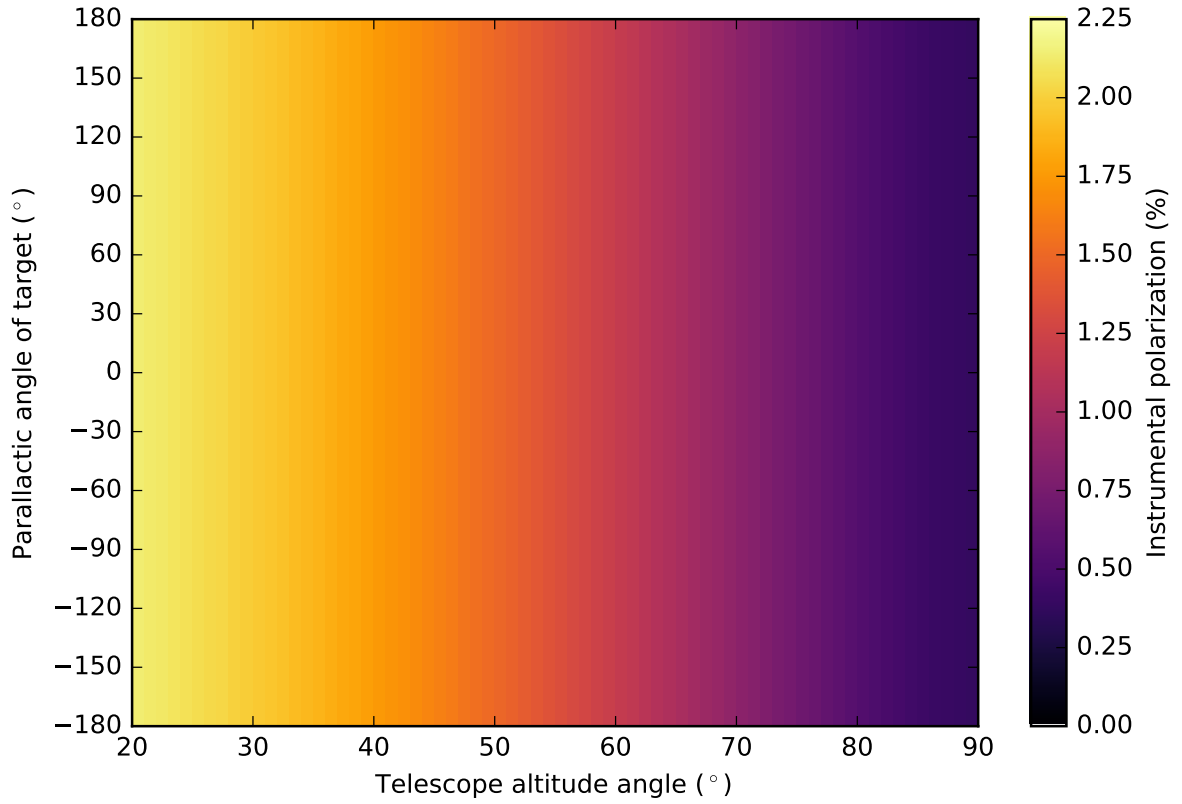

Figure 6.4: Instrumental polarization of the telescope and M4 in H-band as a function of parallactic angle of the target and telescope altitude angle.

polarization (see for example (Canovas et al., 2011)) or polarimetric efficiency are made. Subsequently, every measurement of Stokes I and Stokes Q or U is modeled with the polarimetric response model. Using the model equations describing the measurements, a total of three corrected images (Stokes I, Q and U) is constructed by computing — for every image pixel individually — a weighted linear least-squares solution from the values of that particular pixel in all prepared images (similar to the method used for the Gemini Planet Imager (Perrin et al., 2015)).

Our correction procedure is performed mathematically as follows. For every pixel, the measurements are described as:

$$\boldsymbol{Y} = X\boldsymbol{S}_{\text{in}} \tag{6.6}$$

with $\boldsymbol{Y}$ a column vector containing the n measured pairs of Stokes I and Stokes Q or U for that pixel, $\boldsymbol{S}_{\text{in}}$ the Stokes vector incident on the telescope for that pixel and X a matrix that contains the model equations describing the measurements. These model equations are derived from the Mueller matrix describing the complete optical system M_{sys} (see Section 4.1) with the estimated parameters from Table 4.1:

$$M_{\text{sys}} = M_{\text{CI}}\,T(-\Theta_{\text{der}})M_{\text{der}}\,T(\Theta_{\text{der}})\,T(-\Theta_{\text{HWP}})M_{\text{HWP}}\,T(\Theta_{\text{HWP}})M_{\text{M4}}\,T(a)M_{\text{UT}}\,T(p) \tag{6.7}$$

with:

$$\Theta_{\text{HWP}} = \theta_{\text{HWP}} + \delta_{\text{HWP}} \tag{6.8}$$

$$\Theta_{\text{der}} = \theta_{\text{der}} + \delta_{\text{der}} \tag{6.9}$$

The component groups M_{UT}, M_{M4}, M_{HWP}, and M_{der} are modeled with the component Mueller matrix M_{com}:

$$M_{\mathrm{com}} = \frac{1}{2}\begin{bmatrix} 1+\epsilon & 1-\epsilon & 0 & 0 \\ 1-\epsilon & 1+\epsilon & 0 & 0 \\ 0 & 0 & 2\sqrt{\epsilon}\cos\Delta & 2\sqrt{\epsilon}\sin\Delta \\ 0 & 0 & -2\sqrt{\epsilon}\sin\Delta & 2\sqrt{\epsilon}\cos\Delta \end{bmatrix} \tag{6.10}$$

and M_{CI} is equal to:

$$M_{\mathrm{CI}} = \begin{bmatrix} 1 & 0 & 0 & 0 \\ 0 & d & 0 & 0 \\ 0 & 0 & 1 & 0 \\ 0 & 0 & 0 & 1 \end{bmatrix} \tag{6.11}$$

where $d = \sqrt{q_{\mathrm{in,pol}}}$ is the efficiency of the analyzer polarizers (see Section 4.3).

The model equation describing the i-th measurement of Stokes I is equal to the first row (green) of the Mueller matrix $M_{\mathrm{DS},i}$ that describes the i-th double sum and that is a function of the average parallactic, altitude, HWP and derotator angles of the first (subscript 1) and second (subscript 2) measurement:

$$\begin{aligned} M_{\mathrm{DS},i} &= \frac{1}{2}\left[M_{\mathrm{sys}}(p_{1,i}, a_{1,i}, \theta_{\mathrm{HWP},1,i}, \theta_{\mathrm{der},1,i}) + M_{\mathrm{sys}}(p_{2,i}, a_{2,i}, \theta_{\mathrm{HWP},2,i}, \theta_{\mathrm{der},2,i})\right] \\ &= \begin{bmatrix} (I\rightarrow I)_{\mathrm{DS},i} & (Q\rightarrow I)_{\mathrm{DS},i} & (U\rightarrow I)_{\mathrm{DS},i} & (V\rightarrow I)_{\mathrm{DS},i} \\ (I\rightarrow Q)_{\mathrm{DS},i} & (Q\rightarrow Q)_{\mathrm{DS},i} & (U\rightarrow Q)_{\mathrm{DS},i} & (V\rightarrow Q)_{\mathrm{DS},i} \\ (I\rightarrow U)_{\mathrm{DS},i} & (Q\rightarrow U)_{\mathrm{DS},i} & (U\rightarrow U)_{\mathrm{DS},i} & (V\rightarrow U)_{\mathrm{DS},i} \\ (I\rightarrow V)_{\mathrm{DS},i} & (Q\rightarrow V)_{\mathrm{DS},i} & (U\rightarrow V)_{\mathrm{DS},i} & (V\rightarrow V)_{\mathrm{DS},i} \end{bmatrix} \end{aligned} \tag{6.12}$$

Similarly, the equation describing the i-th measurement of Stokes Q or U is equal to the second row (blue) of the Mueller matrix $M_{\mathrm{DD},i}$ that describes the i-th double difference (Stokes U in the celestial reference frame is measured as Stokes Q in the instrument's reference frame by rotating the HWP):

$$\begin{aligned} M_{\mathrm{DD},i} &= \frac{1}{2}\left[M_{\mathrm{sys}}(p_{1,i}, a_{1,i}, \theta_{\mathrm{HWP},1,i}, \theta_{\mathrm{der},1,i}) - M_{\mathrm{sys}}(p_{2,i}, a_{2,i}, \theta_{\mathrm{HWP},2,i}, \theta_{\mathrm{der},2,i})\right] \\ &= \begin{bmatrix} (I\rightarrow I)_{\mathrm{DD},i} & (Q\rightarrow I)_{\mathrm{DD},i} & (U\rightarrow I)_{\mathrm{DD},i} & (V\rightarrow I)_{\mathrm{DD},i} \\ (I\rightarrow Q)_{\mathrm{DD},i} & (Q\rightarrow Q)_{\mathrm{DD},i} & (U\rightarrow Q)_{\mathrm{DD},i} & (V\rightarrow Q)_{\mathrm{DD},i} \\ (I\rightarrow U)_{\mathrm{DD},i} & (Q\rightarrow U)_{\mathrm{DD},i} & (U\rightarrow U)_{\mathrm{DD},i} & (V\rightarrow U)_{\mathrm{DD},i} \\ (I\rightarrow V)_{\mathrm{DD},i} & (Q\rightarrow V)_{\mathrm{DD},i} & (U\rightarrow V)_{\mathrm{DD},i} & (V\rightarrow V)_{\mathrm{DD},i} \end{bmatrix} \end{aligned} \tag{6.13}$$

With the pair of model equations for each measurement, the matrix X can be constructed and Equation 6.6 can be written as:

$$\boldsymbol{Y} = \begin{bmatrix} I_1 \\ Q_1 \\ I_2 \\ Q_2 \\ \vdots \\ I_n \\ Q_n \end{bmatrix} = \begin{bmatrix} (I\rightarrow I)_{\mathrm{DS},1} & (Q\rightarrow I)_{\mathrm{DS},1} & (U\rightarrow I)_{\mathrm{DS},1} & (V\rightarrow I)_{\mathrm{DS},1} \\ (I\rightarrow Q)_{\mathrm{DD},1} & (Q\rightarrow Q)_{\mathrm{DD},1} & (U\rightarrow Q)_{\mathrm{DD},1} & (V\rightarrow Q)_{\mathrm{DD},1} \\ (I\rightarrow I)_{\mathrm{DS},2} & (Q\rightarrow I)_{\mathrm{DS},2} & (U\rightarrow I)_{\mathrm{DS},2} & (V\rightarrow I)_{\mathrm{DS},2} \\ (I\rightarrow Q)_{\mathrm{DD},2} & (Q\rightarrow Q)_{\mathrm{DD},2} & (U\rightarrow Q)_{\mathrm{DD},2} & (V\rightarrow Q)_{\mathrm{DD},2} \\ \vdots & \vdots & \vdots & \vdots \\ (I\rightarrow I)_{\mathrm{DS},n} & (Q\rightarrow I)_{\mathrm{DS},n} & (U\rightarrow I)_{\mathrm{DS},n} & (V\rightarrow I)_{\mathrm{DS},n} \\ (I\rightarrow Q)_{\mathrm{DD},n} & (Q\rightarrow Q)_{\mathrm{DD},n} & (U\rightarrow Q)_{\mathrm{DD},n} & (V\rightarrow Q)_{\mathrm{DD},n} \end{bmatrix} \begin{bmatrix} I_{\mathrm{in}} \\ Q_{\mathrm{in}} \\ U_{\mathrm{in}} \\ V_{\mathrm{in}} \end{bmatrix} \tag{6.14}$$

For every pixel, the incident Stokes vector is computed as the weighted linear least-squares solution:

$$\hat{\boldsymbol{S}}_{\mathrm{in}} = \underset{\boldsymbol{S}_{\mathrm{in}}}{\arg\min} \left\| W^{1/2}(\boldsymbol{Y} - X\boldsymbol{S}_{\mathrm{in}}) \right\|^2 \tag{6.15}$$

or:

$$\hat{\boldsymbol{S}}_{\mathrm{in}} = (X^{\mathsf{T}} W X)^{-1} X^{\mathsf{T}} W \boldsymbol{Y} \tag{6.16}$$

where W is the weight matrix that can for example be computed from the signal-to-noise ratios of the planet

in the prepared *I*-images to give more weight to the higher-quality measurements (usually the reciprocal of the variance of the measurements is used as weights in weighted least squares):

$$W = \begin{bmatrix} SNR^2_{\mathrm{DS},1} & 0 & 0 & 0 & \cdots & 0 & 0 \\ 0 & SNR^2_{\mathrm{DS},1} & 0 & 0 & \cdots & 0 & 0 \\ 0 & 0 & SNR^2_{\mathrm{DS},2} & 0 & \cdots & 0 & 0 \\ 0 & 0 & 0 & SNR^2_{\mathrm{DS},2} & \cdots & 0 & 0 \\ \vdots & \vdots & \vdots & \vdots & \ddots & 0 & 0 \\ 0 & 0 & 0 & 0 & 0 & SNR^2_{\mathrm{DS},n} & 0 \\ 0 & 0 & 0 & 0 & 0 & 0 & SNR^2_{\mathrm{DS},n} \end{bmatrix} \tag{6.17}$$

Finally, the normalized Stokes parameters, degree of linear polarization and angle of linear polarization in each pixel can be computed (see Equations 2.8 and 2.9).

To exemplify the correction of the optical system's polarimetric response, the method described above is used to accurately determine the linearly polarized intensity[4] and angle of linear polarization over the circumstellar disk of TW Hya, using the coronagraphic observations in field-tracking mode by van Boekel et al. (submitted). A comparison of this method with a reduction that does not use our polarimetric response model is shown in Figure 6.5. Figure 6.5a shows three prepared *Q*-images of the disk of TW Hya (so-called butterfly patterns) with $\theta_{\mathrm{der}} = 349.7^\circ, 342.0^\circ$ and 334.1° (from left to right). With an ideal instrument, the axes of the black 'wings' of the butterfly patterns would be aligned vertically, and the axes of the white 'wings' horizontally. However, due to in particular the derotator retardance, the butterfly patterns rotate clockwise (i.e. offset of angle of linear polarization, see Figure 4.12) and the signal-to-noise ratio (*SNR*) decreases (i.e. lower polarimetric efficiency, see Figure 4.11) for increasing deviation of the derotator angle from 0° (or 360°). The rotation of the butterfly patterns can be accounted for in the data reduction without using the polarimetric response model by assuming that the angle of linear polarization over the disk is azimuthal everywhere (the disk is seen almost pole-on), i.e. perpendicular to the line connecting a point on the disk with the star. The resulting linearly polarized intensity image (scaled with the square of the distance from the central star) is shown in Figure 6.5b[5].

Using the polarimetric response model and the least-squares method described above, a polarized intensity image can be constructed without making assumptions about the polarization signal of the disk. Figure 6.5c shows the *Q*-images after they have been corrected pixel-by-pixel with the polarimetric response model. Although it is preferred to directly compute the final *Q*- and *U*-images using linear least-squares, the correction is performed on individual HWP cycles to illustrate the effect of the method. The model used only included the retardance of the derotator, the telescope and M4, and it was assumed that the incident Stokes *V* can be neglected[6]. From Figure 6.5c, it can be seen that the model accurately corrects the rotation of the butterfly patterns as well as the decrease in polarimetric efficiency. Because the correction of the polarimetric efficiency increases the pixel values of the images, also the noise in the images is increased (the *SNR* of an image does not change). This is clearly visible in the rightmost image of Figure 6.5c. By using weighted least-squares with the *SNR* of the images as weights (see Equation 6.17), more weight can be given to the higher-quality images that have been obtained with a higher polarimetric efficiency.

The linearly polarized intensity image (scaled with the square of the distance from the central star) after accounting for the polarimetric response of the optical system with linear least-squares is shown in Figure 6.5d. Since this image is constructed without making assumptions about the polarization signal of the disk, it is more accurate than Figure 6.5b. In addition, the angle of linear polarization over the disk does not have to be azimuthal, but is computed instead (indicated with the white lines). It appears that the assumption of azimuthally polarized light used to construct Figure 6.5b is accurate, and therefore Figures 6.5b and d are very similar. However, in case of local inhomogeneities in particle density and/or particle properties within a disk, the angle of linear polarization will not necessarily be azimuthal and assuming azimuthally polarized light (as for Figure 6.5b) will then yield an erroneous polarized intensity image. Moreover, by making this assumption, it will be very hard to prove deviations from the assumed polarization direction. By using the

[4] The degree of linear polarization of the disk is hard to obtain, because the total intensity over the disk cannot be accurately determined due to residual speckles from the star that overlap with the disk.

[5] This reduction has been performed by Jos de Boer.

[6] A correction using the complete polarimetric response model is left for future work.

least-squares method to account for the polarimetric response, the most accurate polarized intensity image will result and the angle of linear polarization can be computed. Therefore it is recommended to always reduce the data with the least-squares method, regardless of which disk has been observed and which filter has been used.

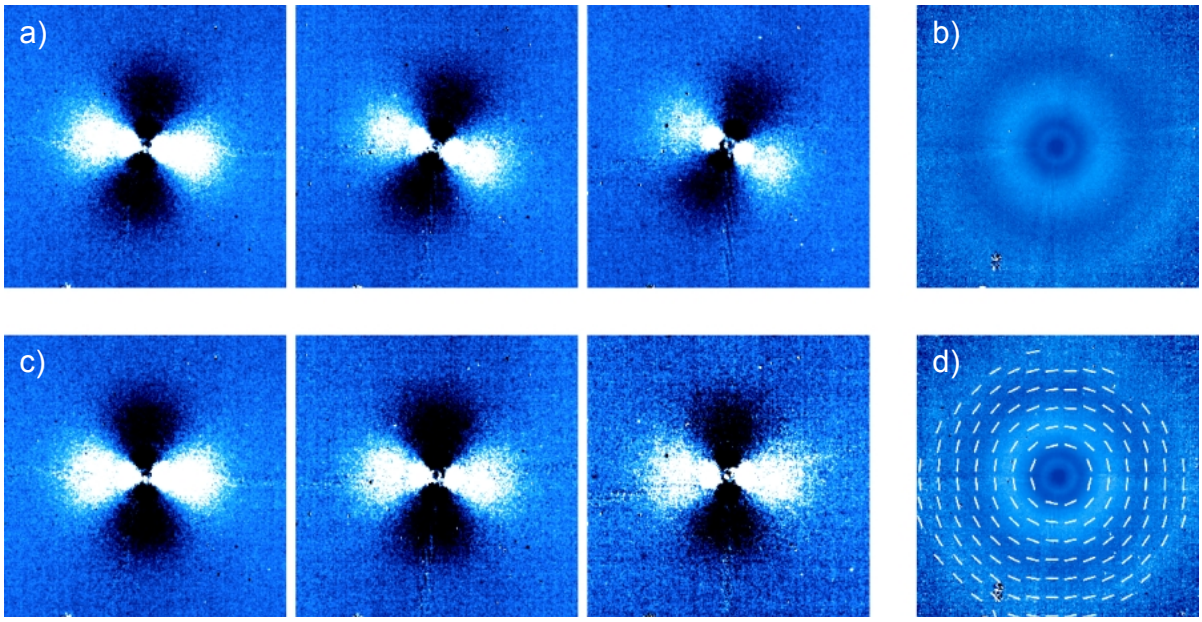

Figure 6.5: Correction of the optical system's polarimetric response to accurately determine the linearly polarized intensity and angle of linear polarization over the circumstellar disk of TW Hya. Panel a) shows the uncorrected Stokes *Q*-images observed with (from left to right) $\theta_{\text{der}} = 349.7°, 342.0°, 334.1°$. Panel b) shows the linearly polarized intensity image (scaled with the square of the distance from the central star) of TW Hya's disk after correcting the rotation of the *Q*- and *U*-images by assuming azimuthally polarized light. Panel c) shows the Stokes *Q*-images after correction with the polarimetric response model and panel d) shows the linearly polarized intensity (scaled with the square of the distance from the central star) and angle of linear polarization over TW Hya's disk after accounting for the polarimetric response of the optical system with weighted linear least-squares.

6.3 Polarimetric accuracy of science observations

Because the degree of linear polarization of exoplanets at near-infrared wavelengths will generally only be between a few tenths of a percent and a percent, the aim is to achieve a total absolute polarimetric accuracy of $\sim 0.1\%$. To attain this total accuracy, an absolute polarimetric accuracy, i.e. the uncertainty in the instrumental polarization, of $< 0.1\%$ and a relative polarimetric accuracy, i.e. the accuracy that scales with the input polarization signal, of $\sim 1\%$ is aimed for. Assuming that the measurements are independent, i.e. the errors are uncorrelated, the absolute polarimetric accuracy s_{abs} is calculated as:

$$s_{\text{abs}} = \sqrt{s_{\text{unpol}}^2 + s_{\text{std}}^2} \tag{6.18}$$

with s_{unpol} the accuracy of fit of the unpolarized source measurements (see Table 4.2) and s_{std} the accuracy of fit of the observations of the unpolarized standard star (see Table 5.3). The relative polarimetric accuracy, s_{rel}, is equal to the accuracy of fit of the polarized source measurements (see Table 4.2). The absolute and relative accuracies in Y-, J-, H- and K_s-band are shown in Table 6.1. From this Table, and assuming that systematic errors are small, it follows that the requirements on the absolute and relative accuracies are (amply) met for all filters.

Table 6.1: Absolute polarimetric accuracy and relative polarimetric accuracy in Y-, J-, H- and K_s-band.

Filter	Absolute polarimetric accuracy (%)	Relative polarimetric accuracy (%)
BB_Y	0.072	0.74
BB_J	0.045	0.41
BB_H	0.033	0.59
BB_K_s	0.099	0.55

The total absolute polarimetric accuracies in Stokes q and u, s_q and s_u, respectively, follow from[7]:

$$s_q = s_{abs} + s_{rel}\hat{q}_{in} \tag{6.21}$$

$$s_u = s_{abs} + s_{rel}\hat{u}_{in} \tag{6.22}$$

where $\hat{q}_{in}$ and $\hat{u}_{in}$ are the incident Stokes q and u that follow from the least-squares solution that accounts for the polarimetric response of the complete optical system. To compute the accuracy of measuring the degree and angle of linear polarization, see Sparks and Axon (1999) and Patat and Romaniello (2006). The total absolute accuracies of measuring Stokes q or u of a 1% polarized exoplanet and a 30% polarized disk in Y-, J-, H- and K_s-band are shown in Table 6.2. Assuming systematic errors are small, and correcting for the polarimetric response of the complete optical system, the polarization signal of the exoplanet can be measured with an accuracy well within the required total absolute accuracy of $< 0.1\%$ in Y-, J- and H-band. In K_s-band, the accuracy is $\sim 0.1\%$.

For the disk, the attainable accuracies are below 0.3% in all filters, which can be regarded as a high accuracy considering the high degree of linear polarization of the incident light. However, in reality the accuracy of measuring the polarization signal of a disk is much lower, because the total intensity across the disk cannot be accurately determined due to residual speckles from the star that fall within the disk image. Reasonable estimates of the total intensity of the disk can be made by subtracting the point spread function (PSF) of a reference star from the disk images (see for example (Canovas et al., 2013)), but it is unlikely that the total intensity can be determined with sub-percent accuracy. Therefore, the accuracy of 0.3% for the disk should be considered a lower limit.

Table 6.2: Total absolute polarimetric accuracy in Stokes q (or u) for 1% polarized exoplanet and a 30% polarized disk in Y-, J-, H- and K_s-band.

Filter	s_q for 1% polarized exoplanet (%)	s_q for 30% polarized disk (%)
BB_Y	0.079	0.29
BB_J	0.049	0.17
BB_H	0.039	0.21
BB_K_s	0.10	0.26

[7] In the general case, the polarimetric accuracy would be described by a 4×4 matrix ΔX (Ichimoto et al., 2008). With this matrix, the accuracy of measuring the Stokes vector, $\Delta \boldsymbol{S}$, can be computed from the measured incident Stokes vector $\hat{\boldsymbol{S}}_{in}$ (from the least-squares solution that account for the polarimetric response of the complete optical system):

$$\Delta \boldsymbol{S} = \Delta X \hat{\boldsymbol{S}}_{in} \tag{6.19}$$

For H-band, the matrix ΔX would for example be equal to:

$$\Delta X_H = \begin{bmatrix} - & - & - & - \\ 0.033 & 0.59 & - & - \\ 0.033 & - & 0.59 & - \\ - & - & - & - \end{bmatrix} \tag{6.20}$$

With IRDIS, it is not possible to determine all elements of ΔX, because for the calibration only a very limited number of different polarization states can be injected into the optical system.

7 Conclusions and recommendations

Currently, the characterization of the atmospheres of exoplanets through direct imaging leverages on the analysis of only the intensity of their light as a function of wavelength and time. However, additional information on the composition and structure of exoplanetary atmospheres could be deduced with polarimetry. The main objective of this master thesis is to investigate the feasibility of combining angular differential imaging (ADI) and accurately calibrated polarimetry with the recently commissioned VLT instrument SPHERE/IRDIS to for the first time detect and possibly characterize exoplanetary atmospheres through direct imaging polarimetry at near-infrared wavelengths.

To this end, IRDIS' polarimetric sensitivity, i.e. the noise level in the degree of linear polarization, was estimated to assess whether IRDIS can detect the expected polarization signal of exoplanets. To derive the exoplanet's true degree and angle of linear polarization from a successful measurement of the polarization signal, a model describing the polarimetric response of the complete optical system, i.e. the modification of the polarization signal induced by the telescope and instrument, was established. Finally, the polarimetric accuracy of the measurements, i.e. the uncertainty in the measured polarization signal, was estimated. Because the degree of linear polarization of exoplanets at near-infrared wavelengths will generally only be between a few tenths of a percent and a percent, both a polarimetric sensitivity and a total absolute polarimetric accuracy (after correcting for the polarimetric response of the complete optical system) of $\sim$ 0.1% was aimed for. In Section 7.1 of this Chapter, the conclusions will be presented. After that, in Section 7.2, recommendations will be made to improve the work of this thesis and an observation strategy for the polarimetric mode of IRDIS will be proposed.

7.1 Conclusions

This thesis work has led to the following conclusions:

- Using HR 8799's planetary system as a study case, IRDIS' polarimetric sensitivity is estimated by extrapolating the results from NaCo observations to IRDIS, and by simulating single-beam polarimetric measurements with real IRDIS data. Based on these estimates, SPHERE/IRDIS is predicted to reach sub-percent polarimetric sensitivity when combining extreme adaptive optics, coronagraphy, ADI with advanced data reduction techniques (e.g. PCA) and dual-beam polarimetry. Given that an exoplanet will generally be between a few tenths of a percent and a percent polarized, it is expected that IRDIS can detect the polarization signals of exoplanets. Whether or not IRDIS can really reach the required polarimetric sensitivity can in the end only be established by performing actual measurements combining ADI and polarimetry.
- The polarimetric response model describing the complete optical system is validated with measurements using the internal light source and observations of an unpolarized standard star. For the optical path downstream of M4 (SPHERE's first mirror), the polarimetric efficiency, i.e. the fraction of the linearly polarized light entering the system that is actually measured, is found to be a function of parallactic and altitude angle when observing in field-tracking mode (in which the field of view is kept with

north up on the detector). The polarimetric efficiency reaches very low values for particular combinations of the parallactic and altitude angle in H-band (minimum 8.1%) and K_s-band (7.9%), while in Y-band (54.8%) and especially J-band (89.5%) the polarimetric efficiency is much better. In addition, the angle of linear polarization oscillates around the ideal value in field-tracking mode, with an extreme maximum deviation in K_s-band (90°) and smaller deviations in Y-, J- and H-band ($\lesssim 3°$, $\lesssim 9°$ and $\lesssim 30°$, respectively). In pupil-tracking mode[1], in which the field of view rotates with respect to the detector so that ADI can be performed, the polarimetric efficiency of the instrument downstream of M4 is also a function of parallactic and altitude angle, but reaches less dramatic minimum values of 93.6%, 76.6%, 63.8% and 66.3% in J-, Y-, H- and K_s-band, respectively.

By calculating a double difference from two exposures taken at half wave plate (HWP) angles 45° apart, the instrumental polarization (IP), i.e. the polarization signal induced by the optics of the instrument, downstream of M4 is kept very small in all filters. The combined IP of the telescope and M4 cannot be removed however, and varies with telescope altitude angle. The IP is maximum at an altitude angle of 20° (minimum allowed altitude angle for the telescope) and equals 3.9%, 2.8%, 2.1% and 1.7% in Y-, J-, H- and K_s-band, respectively. The corresponding minimum values (at an altitude angle of 90°) are 0.73%, 0.51%, 0.38% and 0.34%, respectively. Because the IP at an altitude angle of 90° is not (close to) zero at near-infrared wavelengths, it is probably not zero at visible wavelengths either. Hence the IP of the telescope and M4 probably do not exactly cancel each other when using the additional HWP upstream of M4 employed by SPHERE/ZIMPOL, and it is therefore unlikely that the claimed polarimetric accuracy of 0.1% for ZIMPOL will be reached.

- To derive an exoplanet's true degree and angle of linear polarization from the measured polarization signal, a weighted linear least-squares method is developed that corrects for the polarimetric response of the complete optical system. As an example, this method is used to accurately determine the linearly polarized intensity and angle of linear polarization over the circumstellar disk of TW Hya. Using this method, the most accurate polarized intensity image results and the angle of linear polarization can be derived without assumptions about the polarization signal of the disk, allowing multiple scattering in the disk to be detected.
- The polarimetric accuracy of science measurements is estimated from the accuracies of fitting the model parameters to the measurements with the internal light source and to the observations of the unpolarized standard star. Assuming that systematic errors are small, an absolute polarimetric accuracy, i.e. the uncertainty in the instrumental polarization, of $< 0.1\%$ and a relative polarimetric accuracy, i.e. the accuracy that scales with the input polarization signal, of $< 1\%$ is achieved for all filters. After correcting for the polarimetric response of the complete optical system, the polarization signal of a 1% polarized exoplanet can be measured with a total absolute polarimetric accuracy of 0.079%, 0.049%, 0.039% and 0.10% in Y-, J-, H- and K_s-band, respectively. Given that an exoplanet will generally be between a few tenths of a percent and a percent polarized, IRDIS should be able to accurately measure the degree (and angle) of linear polarization of exoplanets.

Hence, if SPHERE/IRDIS can indeed attain the predicted sub-percent polarimetric sensitivity when combining angular differential imaging and polarimetry, exoplanetary atmospheres can be characterized for the first time through direct imaging polarimetry.

7.2 Recommendations

The following recommendations are made to improve the work of this thesis:

- After actual measurements combining ADI and polarimetry will have been performed with IRDIS, the data reduction strategy that maximizes the polarimetric sensitivity and accuracy should be found. In addition, a contrast curve should be constructed so that future targets for this observation mode can be selected.
- The accuracy of the polarimetric response model should be increased by determining the retardances of the telescope and M4 in Y-, J-, H- and K_s-band from observations of a polarized standard star (rather than from analytical formulae). To further enhance the accuracy, the specifications of the calibration and analyzer polarizers should be obtained, and the modeling of these polarizers should be

[1] Currently, pupil-tracking has not yet been commissioned for IRDIS' polarimetric mode.

improved. Also the atmospheric dispersion corrector (ADC) could be included in the model, as it is the only rotating component of SPHERE that is not accounted for yet. Moreover, total least squares could be used to also take into account the observational errors on the independent variables (parallactic, altitude, HWP and derotator angle). The response model could be made spatial dependent by separately estimating the model parameters for each of the 9 apertures used for the internal source measurements (or even for every pixel separately). Finally, a polarimetric response model should be made for ZIMPOL as well, since its measurement accuracy can probably be significantly improved (as the IP of the telescope and M4 is likely higher than predicted for example).

- The estimates of the polarimetric accuracy should be improved by including systematic errors (if known). Perhaps the accuracy can be computed as a function of parallactic, altitude, HWP and derotator angle by propagating the errors on the estimated parameters using a Monte Carlo simulation.

Finally, to limit the loss of signal due to the varying polarimetric efficiency and to obtain the most accurate results, the following (observation) strategy is recommended when using IRDIS' polarimetry in field-tracking mode:

- When no strict wavelength requirements are present, observe in J-band.
- If Y-, H- or K_s-band has to be used, adjust the time of observation such that the measurements can be taken taken at combinations of parallactic and altitude angle that result in a high polarimetric efficiency (see Figure 6.1).
- If (part of) the observations have to be performed at an unfavorable combination of parallactic and altitude angle, offset the derotator by applying an η-offset (position angle offset of the image) equal to[2]:

$$\eta = \overline{p} - \overline{a} + n \cdot 180^{\circ} \tag{7.1}$$

  with $\overline{p}$ and $\overline{a}$ the average parallactic and altitude angle of the observations, respectively, and n an integer. Because of the offset, the image is not with north up on the detector anymore, and so the image needs to be software derotated in the data reduction.
- For observations with a large variation in parallactic and altitude angle (e.g. long observing runs or observations around the meridian crossing), split the observations in multiple parts with a different η-offset each.
- Observe at longer wavelengths (e.g. K_s-band) and adjust the time of observation such that the observations are performed at a high altitude angle to limit the instrumental polarization (this might result in large parallactic and altitude angle variations, possibly requiring multiple η-offsets).
- Always use the weighted least-squares method to account for the polarimetric response when reducing the data, as this yields the most accurate linearly polarized intensity image and most accurate degree and angle of linear polarization.

[2]The keyword for η in the observation templates is INS.CPRT.POSANG.

References

Amara, A., & Quanz, S. P. (2012). PYNPOINT: an image processing package for finding exoplanets. *Monthly Notices of the RAS*, *427*, 948-955.

B. Halle Nachfl. GmbH. (2016). Retrieved September 1, 2016, from http://www.b-halle.de/EN/Catalog/Retarders/Achromatic_Quartz_and_MgF2_Retarders.php.

Bagnulo, S., Landolfi, M., Landstreet, J. D., Landi Degl'Innocenti, E., Fossati, L., & Sterzik, M. (2009). Stellar Spectropolarimetry with Retarder Waveplate and Beam Splitter Devices. *Publications of the ASP*, *121*, 993-1015.

Bass, M. (1995). *Handbook of Optics Volume II* (2nd ed.). New York: McGraw-Hill.

Bazzon, A., Gisler, D., Roelfsema, R., Schmid, H. M., Pragt, J., Elswijk, E., ... Wildi, F. (2012). SPHERE / ZIMPOL: characterization of the FLC polarization modulator. *Proceedings of SPIE*, *8446*.

Beuzit, J.-L., Feldt, M., Dohlen, K., Mouillet, D., Puget, P., Wildi, F., ... Waters, R. (2008). SPHERE: a 'Planet Finder' instrument for the VLT. *Proceedings of SPIE*, *7014*.

Bonnefoy, M., Zurlo, A., Baudino, J. L., Lucas, P., Mesa, D., Maire, A.-L., ... Wildi, F. (2016). First light of the VLT planet finder SPHERE. IV. Physical and chemical properties of the planets around HR8799. *Astronomy and Astrophysics*, *587*, A58.

Brandt, T. D., McElwain, M. W., Turner, E. L., Abe, L., Brandner, W., Carson, J., ... Tamura, M. (2013). New Techniques for High-contrast Imaging with ADI: The ACORNS-ADI SEEDS Data Reduction Pipeline. *Astrophysical Journal*, *764*, 183.

Canovas, H., Ménard, F., Hales, A., Jordán, A., Schreiber, M. R., Casassus, S., ... Pinte, C. (2013). Near-infrared imaging polarimetry of HD 142527. *Astronomy and Astrophysics*, *556*, A123.

Canovas, H., Rodenhuis, M., Jeffers, S. V., Min, M., & Keller, C. U. (2011). Data-reduction techniques for high-contrast imaging polarimetry. Applications to ExPo. *Astronomy and Astrophysics*, *531*, A102.

Chauvin, G., Lagrange, A. M., Dumas, C., Zuckerman, B., Mouillet, D., Song, I., ... Lowrance, P. (2005). Giant planet companion to 2MASSW J1207334-393254. *Astronomy and Astrophysics*, *438*, L25.

Chilcote, J., Barman, T., Fitzgerald, M. P., Graham, J. R., Larkin, J. E., Macintosh, B., ... Wolff, S. (2015). The First H-band Spectrum of the Giant Planet β Pictoris b. *Astrophysical Journal Letters*, *798*, L3.

Claudi, R. U., Turatto, M., Gratton, R. G., Antichi, J., Bonavita, M., Bruno, P., ... Puget, P. (2008). SPHERE IFS: the spectro differential imager of the VLT for exoplanets search. *Proceedings of SPIE*, *7014*, 70143E.

de Juan Ovelar, M., Snik, F., Meshkat, T., de Kok, R. J., Thalmann, C., Kenworthy, M. A., ... Kasper, M. (submitted). First attempt to obtain Polarimetric Angular Differential images of the HR8799 b and c exoplanets. *Astronomy and Astrophysics*.

de Kok, R. J., Stam, D. M., & Karalidi, T. (2011). Characterizing Exoplanetary Atmospheres through Infrared Polarimetry. *Astrophysical Journal*, *741*, 59.

Dohlen, K., Langlois, M., Saisse, M., Hill, L., Origne, A., Jacquet, M., ... Beuzit, J.-L. (2008). The infra-red dual imaging and spectrograph for SPHERE: design and performance. *Proceedings of SPIE*, *7014*, 3.

RefractiveIndex.INFO. (2016). Retrieved April 4, 2016, from http://www.refractiveindex.info/.

ESO. (2014). The VLT 8.2-meter Unit Telescopes. Retrieved September 24, 2014, from http://www.eso.org/sci/facilities/paranal/telescopes/ut.html.

Galicher, R., Marois, C., Macintosh, B., Barman, T., & Konopacky, Q. (2011). M-band Imaging of the HR 8799 Planetary System Using an Innovative LOCI-based Background Subtraction Technique. *Astrophysical Journal Letters*, *739*, L41.

Hansen, J. E., & Travis, L. D. (1974). Light scattering in planetary atmospheres. *Space Science Reviews*, *16*, 527.

Hecht, E. (2002). *Optics* (4th ed.). San Francisco: Addison Wesley.

Hinkley, S., Oppenheimer, B. R., Soummer, R., Brenner, D., Graham, J. R., Perrin, M. D., ... Kuhn, J. (2009). Speckle Suppression Through Dual Imaging Polarimetry, and a Ground-based Image of the HR 4796A Circumstellar Disk. *Astrophysical Journal*, *701*, 804-810.

Ichimoto, K., Lites, B., Elmore, D., Suematsu, Y., Tsuneta, S., Katsukawa, Y., ... Cruz, T. (2008). Polarization Calibration of the Solar Optical Telescope onboard Hinode. *Solar Physics*, *249*, 233-261.

Ingraham, P., Marley, M. S., Saumon, D., Marois, C., Macintosh, B., Barman, T., ... Wolff, S. G. (2014). Gemini Planet Imager Spectroscopy of the HR 8799 Planets c and d. *Astrophysical Journal Letters*, *794*, L15.

Keller, C. U., Schmid, H. M., Venema, L. B., Hanenburg, H., Jager, R., Kasper, M., ... Yaitskova, N. (2010). EPOL: the exoplanet polarimeter for EPICS at the E-ELT. *Proceedings of SPIE*, *7735*, 6.

Kemp, J. C., Henson, G. D., Steiner, C. T., & Powell, E. R. (1987). The optical polarization of the sun measured at a sensitivity of parts in ten million. *Nature*, *326*, 270-273.

Konopacky, Q. M., Barman, T. S., Macintosh, B. A., & Marois, C. (2013). Detection of Carbon Monoxide and Water Absorption Lines in an Exoplanet Atmosphere. *Science*, *339*, 1398-1401.

Lafrenière, D., Jayawardhana, R., & van Kerkwijk, M. H. (2008). Direct Imaging and Spectroscopy of a Planetary-Mass Candidate Companion to a Young Solar Analog. *Astrophysical Journal Letters*, *689*, L153-L156.

Lafrenière, D., Marois, C., Doyon, R., Nadeau, D., & Artigau, É. (2007). A New Algorithm for Point-Spread Function Subtraction in High-Contrast Imaging: A Demonstration with Angular Differential Imaging. *Astrophysical Journal*, *660*, 770-780.

Langlois, M., Dohlen, K., Vigan, A., Zurlo, A., Moutou, C., Schmid, H. M., ... Wildi, F. (2014). High contrast polarimetry in the infrared with SPHERE on the VLT. *Proceedings of SPIE*, *9147*, 1.

Macintosh, B., Graham, J. R., Barman, T., De Rosa, R. J., Konopacky, Q., Marley, M. S., ... Zuckerman, B. (2015). Discovery and spectroscopy of the young jovian planet 51 Eri b with the Gemini Planet Imager. *Science*, *350*, 64-67.

Marley, M. S., & Sengupta, S. (2011). Probing the physical properties of directly imaged gas giant exoplanets through polarization. *Monthly Notices of the RAS*, *417*, 2874-2881.

Marois, C., Correia, C., Galicher, R., Ingraham, P., Macintosh, B., Currie, T., & De Rosa, R. (2014). GPI PSF subtraction with TLOCI: the next evolution in exoplanet/disk high-contrast imaging. *Proceedings*

of SPIE, *9148*.

Marois, C., Lafrenière, D., Doyon, R., Macintosh, B., & Nadeau, D. (2006). Angular Differential Imaging: A Powerful High-Contrast Imaging Technique. *Astrophysical Journal*, *641*, 556-564.

Marois, C., Macintosh, B., Barman, T., Zuckerman, B., Song, I., Patience, J., ... Doyon, R. (2008). Direct Imaging of Multiple Planets Orbiting the Star HR 8799. *Science*, *322*, 1348-.

Marois, C., Macintosh, B., & Véran, J.-P. (2010). Exoplanet imaging with LOCI processing: photometry and astrometry with the new SOSIE pipeline. *Proceedings of SPIE*, *7736*.

Marois, C., Zuckerman, B., Konopacky, Q. M., Macintosh, B., & Barman, T. (2010). Images of a fourth planet orbiting HR 8799. *Nature*, *468*, 1080-1083.

Meshkat, T., Kenworthy, M. A., Quanz, S. P., & Amara, A. (2014). Optimized Principal Component Analysis on Coronagraphic Images of the Fomalhaut System. *Astrophysical Journal*, *780*, 17.

Miles-Páez, P. A., Zapatero Osorio, M. R., Pallé, E., & Peña Ramírez, K. (2013). Linear polarization of rapidly rotating ultracool dwarfs. *Astronomy and Astrophysics*, *556*, A125.

Moffat, A. F. J. (1969). A Theoretical Investigation of Focal Stellar Images in the Photographic Emulsion and Application to Photographic Photometry. *Astronomy and Astrophysics*, *3*, 455.

Oppenheimer, B. R., Baranec, C., Beichman, C., Brenner, D., Burruss, R., Cady, E., ... Zimmerman, N. (2013). Reconnaissance of the HR 8799 Exosolar System. I. Near-infrared Spectroscopy. *Astrophysical Journal*, *768*, 24.

Patat, F., & Romaniello, M. (2006). Error Analysis for Dual-Beam Optical Linear Polarimetry. *Publications of the ASP*, *118*, 146-161.

Pater, I., & Lissauer, J. J. (2010). *Planetary Sciences* (2nd ed.). Cambridge: Cambridge University Press.

Perrin, M. D., Duchene, G., Millar-Blanchaer, M., Fitzgerald, M. P., Graham, J. R., Wiktorowicz, S. J., ... Wolff, S. G. (2015). Polarimetry with the Gemini Planet Imager: Methods, Performance at First Light, and the Circumstellar Ring around HR 4796A. *Astrophysical Journal*, *799*, 182.

Roelfsema, R., Schmid, H. M., Pragt, J., Gisler, D., Waters, R., Bazzon, A., ... Wildi, F. (2010). The ZIMPOL high-contrast imaging polarimeter for SPHERE: design, manufacturing, and testing. *Proceedings of SPIE*, *7735*.

Schmid, H.-M., Downing, M., Roelfsema, R., Bazzon, A., Gisler, D., Pragt, J., ... Wildi, F. (2012). Tests of the demodulating CCDs for the SPHERE / ZIMPOL imaging polarimeter. *Proceedings of SPIE*, *8446*.

Seager, S., Whitney, B. A., & Sasselov, D. D. (2000). Photometric Light Curves and Polarization of Close-in Extrasolar Giant Planets. *Astrophysical Journal*, *540*, 504.

Sengupta, S., & Marley, M. S. (2010). Observed Polarization of Brown Dwarfs Suggests Low Surface Gravity. *Astrophysical Journal Letters*, *722*, L142-L146.

Sengupta, S., & Marley, M. S. (2016). Detecting Exomoons around Self-luminous Giant Exoplanets through Polarization. *Astrophysical Journal*, *824*, 76.

Siebenmorgem, R., Mouillet, D., Mawet, D., Wahhaj, Z., van den Ancker, M., Smette, A., ... SPHERE Consortium (2014). SPHERE User Manual Issue P95. *ESO*.

Soummer, R., Pueyo, L., & Larkin, J. (2012). Detection and Characterization of Exoplanets and Disks Using Projections on Karhunen-Loève Eigenimages. *Astrophysical Journal Letters*, *755*, L28.

Sparks, W. B., & Axon, D. J. (1999). Panoramic Polarimetry Data Analysis. *Publications of the ASP*, *111*, 1298-1315.

Stam, D. M., Hovenier, J. W., & Waters, L. B. F. M. (2004). Using polarimetry to detect and characterize Jupiter-like extrasolar planets. *Astronomy and Astrophysics*, *428*, 663.

Thalmann, C., Schmid, H. M., Boccaletti, A., Mouillet, D., Dohlen, K., Roelfsema, R., ... Wildi, F. (2008). SPHERE ZIMPOL: overview and performance simulation. *Proceedings of SPIE*, *7014*.

The Extrasolar Planets Encyclopaedia. (2016). Retrieved August 26, 2016, from http://exoplanet.eu/.

Tinbergen, J. (2005). *Astronomical Polarimetry*. Cambridge: Cambridge University Press.

Trujillo-Bueno, J., Moreno-Insertis, F., & Sanchez Martinez, F. (2002). *Astrophysical Spectropolarimetry*. Cambridge: Cambridge University Press.

Turnshek, D. A., Bohlin, R. C., Williamson, R. L., II, Lupie, O. L., Koornneef, J., & Morgan, D. H. (1990). An atlas of Hubble Space Telescope photometric, spectrophotometric, and polarimetric calibration objects. *Astronomical Journal*, *99*, 1243-1261.

van Harten, G., Snik, F., & Keller, C. U. (2009). Polarization Properties of Real Aluminum Mirrors, I. Influence of the Aluminum Oxide Layer. *Publications of the ASP*, *121*, 377.

Wagner, K., Apai, D., Kasper, M., Kratter, K., McClure, M., Robberto, M., & Beuzit, J.-L. (2016). Direct imaging discovery of a Jovian exoplanet within a triple-star system. *Science*, *353*, 673-678.

Wildi, F., Mouillet, D., Beuzit, J.-L., Feldt, M., Dohlen, K., Fusco, T., ... Puget, P. (2009). Calibrating SPHERE, the exo-planet imager for the VLT. *Proceedings of SPIE*, *7440*.

Zurlo, A., Vigan, A., Galicher, R., Maire, A.-L., Mesa, D., Gratton, R., ... Antichi, J. (2016). First light of the VLT planet finder SPHERE. III. New spectrophotometry and astrometry of the HR 8799 exoplanetary system. *Astronomy and Astrophysics*, *587*, A57.

A Application for observing time

European Organisation for Astronomical Research in the Southern Hemisphere

OBSERVING PROGRAMMES OFFICE • Karl-Schwarzschild-Straße 2 • D-85748 Garching bei München • e-mail: opo@eso.org • Tel.: +49 89 320 06473

APPLICATION FOR OBSERVING TIME PERIOD: **98A**

Important Notice:

By submitting this proposal, the PI takes full responsibility for the content of the proposal, in particular with regard to the names of CoIs and the agreement to act according to the ESO policy and regulations, should observing time be granted.

1. Title Category: **C–7**

Characterizing hazes and asymmetries in the atmospheres of the HR 8799 exoplanets with accurate polarimetry

2. Abstract / Total Time Requested

Total Amount of Time: 0.8 nights VM, 0 hours SM

Characterization of the atmospheres of exoplanets through direct imaging currently leverages on the analysis of only the intensity of their light as a function of wavelength and time. We aim to characterize the planets around HR 8799 by measuring their degree and angle of polarization at near-infrared wavelengths (H and K_s). These young gas giants emit infrared radiation that becomes linearly polarized up to a few % by a combination of scattering in haze layers and global asymmetries, e.g. rotational flattening and band structure. To obtain a polarimetric sensitivity $< 0.1\%$, we combine high-contrast imaging with dual-beam polarimetry, while an absolute polarimetric accuracy of $\sim 0.1\%$ will be obtained by applying our validated instrumental polarization model. We will interpret measurements of a non-zero degree of linear polarization with our planetary atmosphere and radiative transfer model. The corresponding angle of linear polarization constrains spin-orbit coupling.

3.

Run	Period	Instrument	Time	Month	Moon	Seeing	Sky	Mode	Type
A	98	SPHERE	0.8n=2x0.8H1	oct	g	0.8	CLR	v	

4. Number of nights/hours Telescope(s) Amount of time

a) already awarded to this project:

b) still required to complete this project:

5. Special remarks:

Our team consists of experts at observing with SPHERE/IRDIS, reduction of IRDIS data, polarimetric calibration and the interpretation of planet observations with radiative transfer models. Experienced users of SPHERE/IRDIS currently living in Chile, will be easily available to help during the observations.

6. Principal Investigator: Julien H. V. Girard, jgirard@eso.org, ESO, ESO Office Santiago

6a. Co-investigators:

J.-L.	Beuzit	CNRS,F
J.	de Boer	Sterrewacht,University of Leiden,NL
R.G.	van Holstein	Sterrewacht,University of Leiden,NL
M.	Kasper	ESO Headquarters Garching,ESO

Following CoIs moved to the end of the document ...

7. Description of the proposed programme

A – Scientific Rationale: The direct detection of planetary radiation allows the characterization of the composition and structure of atmospheres of self-luminous, hot, massive planets. The young planetary system of HR 8799 is known to host four such planets that have already been imaged directly (Marois et al., 2008; Marois et al., 2010; Zurlo et al., 2016), as they are in wide orbits that allow them to be observed spatially separated from their star. Recent spectral measurements of these planets have revealed the presence of gases such as CO, CH_4 and H_2O (Konopacky et al., 2013) and sub-micron dust particles (Bonnefoy et al., 2016) in their atmospheres. Temporal variations in near-infrared gaseous absorption features, such as those of CH_4, strongly suggest the presence of patchy clouds (Oppenheimer et al., 2013).

Traditionally, planetary atmospheres are investigated with photometry and spectroscopy. The degree and direction of linear polarization of the planetary radiation contain additional information on composition and structure of planetary atmospheres (e.g. Hansen & Travis, 1974; Hansen and Hovenier, 1974). Not only the starlight that an exoplanet reflects is expected to be polarized (Seager et al., 2000; Stam et al., 2004), but also the thermal emmission of a planet, as this radiation from inside the atmosphere will be scattered by cloud and haze particles on its way up. If the exoplanet (2D-projected) disk is azimuthally symmetric, polarization signals from different parts of the disk will cancel each other and the disk-integrated degree of polarization will be zero. However, with patchy or banded clouds, and/or a flattened planet due to rapid rotation, the net degree of polarization can be up to several percent at near-infrared wavelengths (Sengupta & Marley, 2010; de Kok et al., 2011). By determining the angle of polarization, the planet's projected spin axis can be constrained, and the time variability of the polarization signal reveals the patchiness of clouds. Combining polarimetic measurements with existing flux measurements can unambiguously reveal particle properties, such as albedo and size.

Near-infrared polarimetry has already been successfully performed for dozens of field brown dwarfs, yielding degrees of linear polarization between 0.1 to 2.5 % in the I-band (Sengupta & Marley, 2010) and up to 0.8 % in the Z- and J-bands (Miles-Páez et al., 2013). There are several reasons why exoplanets are expected to have stronger polarization signals than brown dwarfs: exoplanets have a lower surface gravity, hence a stronger flattening for a given rotation rate, and a lower effective atmospheric temperature can yield stronger polarization signals for a given temperature gradient (de Kok et al., 2011). The first polarimetric detection of exoplanets, however, has yet to be performed. The recently commissioned near-infrared high-contrast polarimeter VLT/SPHERE/IRDIS (Langlois et al., 2010) provides the opportunity to measure these polarization signals for the first time. The planets around HR 8799 are excellent candidates for a first detection of exoplanetary polarization signals: they can be spatially resolved from the star and are expected to have a patchy haze structure (Oppenheimer et al., 2013) that causes a net polarization signal. The planets have been detected with IRDIS with huge signal-to-noise ratio in intensity (> 200; Zurlo et al, 2016), which opens up the possibility for polarimetric characterization.

B – Immediate Objective: We aim to characterize the planets HR 8799 by measuring for the first time the degree and angle of polarization of planets c, d, e, and b (in order of likelihood). These ambitious measurements will reveal unambiguously 1) the presence of atmospheric clouds and hazes, and their patchiness, 2) spatial structure, e.g. flattening and bands, 3) the orientation of the spin axes, and 4) the particle size and cloud top pressure as constrained by the variation of the degree of polarization between the H- and K_s-bands (de Kok et al., 2011). We will achieve a **polarimetric sensitivity**, i.e. the noise level in degree of linear polarization, $< 0.1\%$ by combining Angular Differential Imaging (ADI) with dual-beam polarimetry to suppress the speckle noise at the location of the planet (while averaging out photon and read-out noise). We will attain an **absolute polarimetric accuracy** of $\sim 0.1\%$ by correcting the instrumental (and telescope) polarization (IP) with an IP-model that has been validated at the required level with internal sources and standard stars.

Our measurements with IRDIS will take advantage of its dual-beam polarimetric mode to eliminate differential effects that severly limit polarimetric sensitivity (flat-fielding errors, differential aberrations and seeing). To attain the high contrast required for polarimetry of exoplanets, we will use the pupil-tracking mode and combine ADI with Principal Component Analysis (KLIP; Soummer et al., 2012) to significantly reduce speckle noise, the principle noise component. Combining ADI with polarimetry further suppresses speckle noise (especially at small angular separations), because speckles are unpolarized. Polarimetry of the planets of HR 8799 has already been attempted with VLT/NACO, but the attained contrast appeared to be insufficient for a detection (de Juan Ovelar et al., submitted). From simulations using real IRDIS data, we expect to reach the required contrast observing with IRDIS, as SPHERE's adaptive optics system is more advanced than NACO's, resulting in a more than 1 order of magnitude higher contrast already at the position of planet c. In comparison to the recent attempt to measure infrared exoplanetary polarization with GPI (Jensen-Clem et al., 2016), we will significantly improve on their upper limit of 2.4% by increasing the exposure time by a factor 7 and the amount of sky rotation by a factor 16, and applying more advanced ADI and polarimetric demodulation techniques.

To extrapolate the (null) results from our NACO observations to IRDIS, we scale the attained polarimetric sensitivities with the intensity SNR's, and present our estimated polarimetric sensitivity in the following Table.

Planet	b	c	d	e
Sensitivity scaled from NACO to IRDIS (%)	**0.79**	**0.09**	-	-
Sensitivity scaled from IRDIS "single-" to dual-beam (%)	**1.53**	**0.14**	**0.012**	**0.010**

7. Description of the proposed programme and attachments

Description of the proposed programme (continued)

We obtained an independent estimate of the sensitivity of our observing technique by simulating *single-beam* polarimetric measurements with (non-polarimetric) IRDIS dual-band data of HR 8799 taken with the K2 filter (Zurlo et al., 2016). We separately reduced the even and odd frames with KLIP, and computed the sum and difference of the two results to simulate images of the total intensity (I) and one of the Stokes parameters (e.g. Q), respectively (see Fig. 1). The results from the Table are determined by estimating the expected polarimetric sensitivity at the location of the four planets and by factoring in the significant improvement of a dual-beam polarimeter over a single-beam polarimeter. For the inner planets d and e that are speckle noise limited, the simultaneous recording of opposite polarization directions in the dual-beam systems offers an order of magnitude improvement in polarimetric sensitivity (Keller et al., 2010; Hinkley et al., 2009). Planet b is not speckle noise limited, and has little benefit from single-beam to dual-beam. For planet c we adopted an intermediate improvement factor. Therefore, we are confident that 4 hours of observations (see Section 8) combining ADI with polarimetry will provide the sub-percent sensitivity required to measure polarization signals with high confidence level for planets c, d and e, and for b only when its degree of polarzation is very high ($\sim 5\%$).

To accurately derive a planet's polarization state from a measurement, it is paramount to know the polarimetric response of the whole optical system (telescope and instrument), which for IRDIS is complex and has many rotating components. To this end, we have developed a Mueller matrix model for the optical system that we have validated with internal calibration measurements and observations of standard stars, attaining an absolute polarimetric accuracy of $\sim 0.1\%$ (see Fig. 2). The polarimetric accuracy is particularly affected by the IP, which can make unpolarized sources appear a few percent polarized if not accounted for. IP created downstream from the half-wave plate (HWP) is effectively removed by calculating a double difference from two exposures taken at HWP angles 45° apart (Bagnulo et al., 2009). The combined IP of the telescope and SPHERE's first mirror (M4), cannot be removed however, and varies with telescope altitude angle (see Fig. 2). Fortunately, this IP is small: maximum 1.5% in the H-band and 1.3% in K_s, and we can correct for it with our sub-percent accurate Mueller matrix model.

Performing eight measurements (observing the four known planets around HR 8799 in two filters each) with the predicted polarimetric sensitivity and accuracy shows great promise for a first characterization of exoplanetary atmospheres through polarimetric direct imaging. We will interpret the measurements of non-zero polarization for any of the planets in either filter, with the advanced planetary atmosphere and radiative transfer model of de Kok et al., 2011. If the measurements are indicative of rotational flattening and/or band structure, we can interpret the measured polarization angle in terms of the planetary rotation axis, and investigate whether the planets' spins are aligned with their orbit or that they are affected by planetary encounters. The next step will be to monitor the temporal behavior of the polarization: temporal variation (as already measured for field brown dwarfs (Miles-Páez et al., 2015)) would arise from patchy clouds, with a periodic signal indicating persistent storms, such as Jupiter's Great Red Spot, and revealing atmospheric rotation rates.

Attachments (Figures)

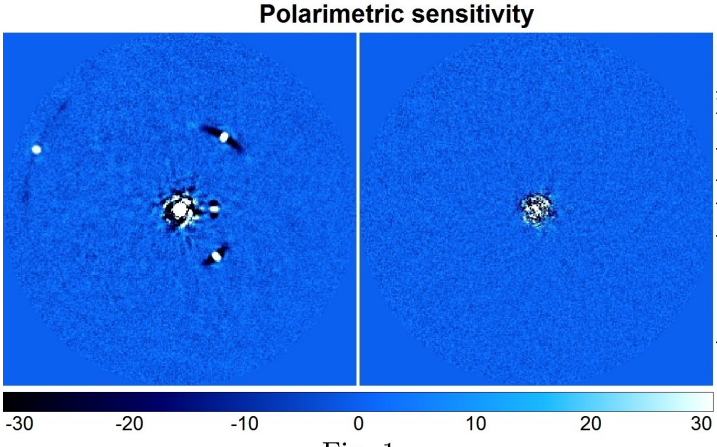

Fig. 1

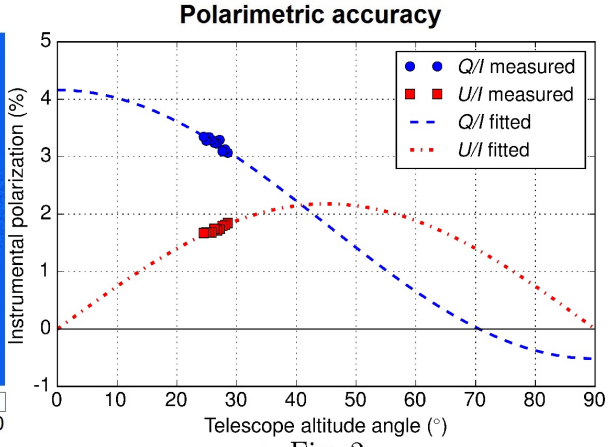

Fig. 2

Fig. 1: IRDIS K2-band images of HR 8799's planets. Left: total intensity image (I). Right: simulated single-beam polarimetric image of one of the Stokes parameters (e.g. Q), assuming zero planet polarization. Fig. 2: Measured (dots) and fitted (lines) instrumental polarization Stokes parameters of the telescope and SPHERE's first mirror (M4) as a function of telescope altitude angle in the Y-band (which has strongest IP).

8. Justification of requested observing time and observing conditions

Lunar Phase Justification: We request dark or gray time. The attainable sensitivity of the observations is dominated by the speckle noise from the central star, but scattered moonlight produces a time-varying polarized background. This background will limit the absolute polarimetric accuracy, even though we will subtract sky dark frames and the brightness of the moon is lower at near-infrared than at optical wavelengths. Because of the large field of view of the active optics of the VLT, it is recommended that the angular distance to the moon is larger than 30° (SPHERE User Manual P97.1). Therefore, October 12, 13, and 14 are unsuitable for our observations.

Time Justification: (including seeing overhead)

To obtain sufficient parallactic rotation to effectively suppress speckle noise with ADI, **at least 3.5 h of observing time is required** when observing this low-altitude target in October. The observation time required to attain the predicted sub-percent sensitivity (see Table in Section 7B) can be estimated by comparing the instrument configuration and measurement approach of our proposed observations with that of the IRDIS dual-band observations of HR 8799, that spanned 112 minutes of observation time. In our observations, frames in opposite polarization directions will be taken simultaneously, rather than sequentially, reducing the observing time by half. Unfortunately, IRDIS' polarizers transmit only half of the incident flux. Since the K_s-filter has ~ 3 times the bandwidth of the K2-filter (SPHERE User Manual P97.1), and therefore transmits ~ 3 times the flux, the observation time can be reduced by a factor ~ 3. In our observations, we repeat the measurements after reversing the polarization direction by rotating the half-wave plate (HWP) 45°, increasing the observation time by a factor 2, and compute a double difference to remove instrumental effects (e.g. instrumental polarization). Finally, the measurements are repeated with the HWP at 22.5° and 67.5° to obtain the image of Stokes U. **Thus, to attain sub-percent sensitivity, the required observation time is $112/2 \cdot 2/3 \cdot 2 \cdot 2 = 149$ min ≈ 2.5 h per filter, well within the 3.5 h required for the parallactic rotation.**

As we have a validated Mueller matrix model, no observations of unpolarized and/or polarized standard stars are required to calibrate the instrument. Before, during and after the observations, sky dark frames need to be taken to allow for the subtraction of the time-varying polarized background. **Therefore, including acquisition overhead and the time required to take sky dark frames, we need two times ~ 4 hours to perform polarimetry on HR 8799's planets in the H- and K_s-band.**

8a. Telescope Justification:

An 8-meter class telescope and a high-contrast instrument with advanced adaptive optics is required to directly image the planets around HR 8799 with a sufficiently high signal-to-noise ratio. The extreme adaptive optics system of SPHERE makes SPHERE/IRDIS currently the only ESO instrument capable of reaching the sensitivity and polarimetric accuracy that is required to perform polarimetry on HR 8799's planets in the H- and K_s-bands.

8b. Observing Mode Justification (visitor or service):

We request visitor mode observations, because our observations are novel and challenging, and may need real-time modifications to the observations blocks (OBs). In addition, we know that for a certain range of derotator angles the derotator causes significant cross-talk in the H- and K_s-band. Although we can account for this effect with our validated Mueller matrix model, the cross-talk severely decreases the polarimetric efficiency of the instrument and therefore limits the attainable polarimetric sensitivity. This efficiency loss can be avoided by applying an offset to the derotator angle to minimize the cross-talk, but this can only be done manually.

8c. Calibration Request:

Standard Calibration

9. Report on the use of ESO facilities during the last 2 years

The IRDIS dual-beam observations of HR 8799 (Zurlo et al., 2016) have been taken in July, August and December, 2014 during the commissioning of SPHERE. In addition, we have taken internal calibration measurements and observed standard stars to validate the Mueller matrix model we developed and that describes the complete optical system, i.e. the telescope and instrument.

9a. ESO Archive - Are the data requested by this proposal in the ESO Archive (http://archive.eso.org)? If so, explain the need for new data.

The only polarimetric data of HR 8799's planets (b and c) in the ESO Archive is that of program 089.C-0688 (PI: R. de Kok) taken with NACO in July, 2012. However, as described in Section 7B, the attained contrast appeared to be insufficient for a detection of polarization signals.

9b. GTO/Public Survey Duplications:

HR 8799 is on the SPHERE GTO list for IRDIFS observations. Our observations combine classical imaging with polarimetry (without IFS), which has a fundamentally different application. SHINE (previously NIRSUR) is not trying to find the polarization signal of the planets. We are not aiming towards first detections of new planets (the aim of SHINE), but aim to measure the polarized light of already detected planets.

10. Applicant's publications related to the subject of this application during the last 2 years

(Selected list) Zurlo, A., **Vigan, A.** et al. (incl. **Kasper, M.**, **Beuzit, J.-L.**, **Girard, J.H.**, **Langlois, M.**, **Mouillet, D.**), 2016, A&A, 587, A57: First light of the VLT planet finder SPHERE. III. New spectrophotometry and astrometry of the HR 8799 exoplanetary system

Bonnefoy, M., **Zurlo, A.** et al. (incl. **Vigan, A.**, **Kasper, M.**, **Beuzit, J.-L.**, **Girard, J.H.**, **Langlois, M.**, **Mouillet, D.**), 2016, A&A, 587, A58: First light of the VLT planet finder SPHERE. IV. Physical and chemical properties of the planets around HR8799

Vigan, A. et al. (incl. **Zurlo, A.**, **Beuzit, J.-L.**, **Girard, J.H.**, **Kasper, M.**, **Langlois, M.**, **Mouillet, D.**), 2016, A&A, 587, A55: First light of the VLT planet finder SPHERE. I. Detection and characterization of the substellar companion GJ 758 B

Vigan, A. et al., 2015, MNRAS, 454, 129: High-contrast imaging of Sirius A with VLT/SPHERE: looking for giant planets down to one astronomical unit

Pinilla, P., **de Boer, J.** et al. (incl. **Girard, J.H.**), 2015, A&A, 584, L4: Variability and dust filtration in the transition disk J160421.7-213028 observed in optical scattered light

Canovas, H., Meńard, F., **de Boer, J.** et al., 2015, A&A, 582, L7: Nonazimuthal linear polarization in protoplanetary disks

Zurlo, A., **Vigan, A.** et al. (incl. **Langlois, M.**, **Beuzit, J.-L.**, **Kasper, M.**, **Mouillet, D.**), 2014, A&A 572, A85: Performance of the VLT Planet Finder SPHERE I. Photometry and astrometry precision with IRDIS and IFS in laboratory

Snik, F. et al. (incl. **Stam, D.M.**, **de Boer, J.**, **Keller, C.U.**), 2014, GRL, 41, 7351: Mapping atmospheric aerosols with a citizen science network of smartphone spectropolarimeters

de Boer, J., **Girard, J.H.** et al. (incl. **Snik, F.**, **Keller, C.U.**), 2014, Proc. SPIE, 9147, 15: Characterizing Instrumental Effects on Polarization at a Nasmyth focus using NaCo

11. List of targets proposed in this programme

Run	Target/Field	α(J2000)	δ(J2000)	ToT	Mag.	Diam.	Additional info	Reference star
A	HR 8799	23 07 28.7	+21 08 03.3	8.0	5.96			

Target Notes: From the absolute magnitudes presented by Zurlo et al., 2016, and the distance to HR 8799 (39.4 pc) given by van Leeuwen, 2007, the apparent magnitudes of the planets are 18.1 (planet b), 17.1 (c), 17.0 (d) and 16.9 (e) in the H2-band and 17.0 (planet b), 15.9 (c), 15.8 (d) and 15.8 (e) in the K2-band. These values provide good estimates of the apparent magnitudes of the planets in the H- and K_s-bands. The time on target (ToT) is specified as the total observing time of the two half nights (observing one half night in H-band and one half night in K_s-band) and includes overhead and the time required to take sky dark frames.

12. Scheduling requirements

1. Run Splitting

Run	splitting
A	0.8H1,1s,0.8H1

12. Scheduling requirements contd...

4. Specific date(s) for time critical observations:

Run	from	to	reason
A	01-oct-16	25-oct-16	After October 25, the telescope altitude angle is too low (below 30°; airmass larger than 2.0) during part of our 4-hour observations.

13. Instrument configuration

Period	Instrument	Run ID	Parameter	Value or list
98	SPHERE	A	IRDIS-DPI	N-ALC-YJH-S/BB-H
98	SPHERE	A	IRDIS-DPI	N-ALC-YJH-S/BB-Ks
98	SPHERE	A	IRDIS-DPI	N-ALC-Ks-S/BB-Ks

6b. Co-investigators:

...continued from Box 6a.

C.U.	Keller	Sterrewacht,University of Leiden,NL
R.J.	de Kok	Sterrewacht,University of Leiden,NL
M.	Langlois	Centre de Recherche Astrophysique de Lyon,F
D.	Mouillet	CNRS,F
F.	Snik	Sterrewacht,University of Leiden,NL
D.M.	Stam	Delft University of Technology,NL
A.	Vigan	CNRS,F
A.	Zurlo	Universidad Diego Portales,CL